DOE/ER/53222--104

DE91 004118

Transport of Carbon Ion Test Particles and Hydrogen Recycling in the Plasma of the Columbia Tokamak "HBT"

by

Jian-Hua Wang

Submitted in partial fulfillment of the
requirements for the degree of
Doctor of Philosophy
in the Graduate School of Arts and Science

COLUMBIA UNIVERSITY

1990

MASTER

ABSTRACT

Transport of Carbon Ion Test Particles and Hydrogen Recycling in the Plasma of the Columbia Tokamak "HBT"

Jian-Hua Wang

Carbon impurity ion transport is studied in the Columbia High Beta Tokamak (HBT), using a carbon tipped probe which is inserted into the plasma ($n_e \simeq 1-5\times10^{14}$ (cm^{-3}), $T_e \simeq 4-10$ (eV), $B_t \simeq 0.2-0.4$ (T)). Carbon impurity light, mainly the strong lines of C_{II} (4,267A, emitted by the C^+ ions) and C_{III} (4,647A, emitted by the C^{++} ions), is formed by the ablation or sputtering of plasma ions and by the discharge of the carbon probe itself. The diffusion transport of the carbon ions is modeled by measuring the space-and-time dependent spectral light emission of the carbon ions with a collimated optical beam and photomultiplier. The point of emission can be observed in such a way as to sample regions along and transverse to the toroidal magnetic field. The carbon ion diffusion coefficients are obtained by fitting the data to a diffusion transport model. It is found that the diffusion of the carbon ions is "classical" and is controlled by the high collisionality of the HBT plasma; the diffusion is a two-dimensional problem and the expected dependence on the charge of the impurity ion is observed.

The measurement of the spatial distribution of the H_α emissivity was obtained by inverting the light signals from a 4-channel polychromator; the data were used to calculate the minor-radial influx , the density, and the recycling time of neutral hydrogen atoms or molecules. The calculation shows that the particle recycling time τ_p is comparable with the plasma energy confinement time τ_E; therefore, the recycling of the hot plasma ions with the cold neutrals from the walls is one of the main mechanisms for loss of plasma energy.

Table of Contents

Chapter 1: Introduction 1

1.1 The History of the Columbia HBT 1

1.2 The Objective of The Carbon Probe Experiment 4

1.3 The Method of The Carbon Probe Experiment 5

1.4 The Outline of This Report 6

Chapter 2: Carbon Probe Technique and Experimental Setup 9

2.1 Carbon Probe Construction 9

2.2 Carbon Probe Operation 12

2.3 Carbon Probe Perturbation 15

2.3.1 Density Perturbation 15

2.3.2 Magnetic Field Perturbation 15

2.4 The Ratio of C_{II} and C_{III} Light Emission 17

2.5 Single Channel Optical System 17

2.6 Other HBT Diagnostics and Operations 19

Chapter 3: Diffusion Model of Carbon Ions 26

3.1 Collision Time of Carbon Ions with Plasma Ions and Electrons 26

3.2 Basic Assumptions 38

3.3 Ionization and Recombination Time of Carbon Ions 40

3.4 Impurity Transport Modeling 41

3.5 Three Models of the Discharge Source 48

3.5.1 Delta Function Source Model 51

3.5.2 Square-wave Function Source Model 53

3.5.3 Sine-wave Function Source Model 57

3.5.4 Comparison of the Three Models 58

Chapter 4: The Observation and Data Fitting.....62

4.1 Introduction.....62

4.2 The Diffusion Coefficient Measurements 63

4.3 Convection Effect.....75

4.4 Error Analysis.....84

Chapter 5: Carbon Ion Diffusion in HBT.....89

5.1 Introduction.....89

5.2 Classical Impurity Diffusion 90

5.3 Neoclassical Impurity Diffusion.....103

5.4 Bohm Diffusion 107

5.5 Discussion of Carbon Ion Diffusion in HBT 108

Chapter 6: H_α Light Measurement 117

6.1 Introduction.....117

6.2 H_α Light Production.....117

6.3 Four Channel Optical System 118

6.4 Inversion 120

6.4.1 Abel Inversion 120

6.4.2 Improved Abel Inversion 123

6.4.3 Numerical Simulation of the Inversion.....128

6.5 Influxes and Recycling Time of Neutral Hydrogen 134

6.6 H_α Light Emission in HBT 138

6.6.1 Parallel Bias Case 138

6.6.2 Reverse Bias Case 143

6.6.3 The Pressure Effect 147

Chapter 7: Conclusion 150

7.1 The Carbon Ion Diffusion Measurement 150

7.2 The H_α Light Measurement 151

References 152

Appendix: The Observation of An Instability Using the Carbon Probe Technique 158

List of Figures

Figure 1.1 The general layout of the HBT machine 3

Figure 1.2 The summary of the impurity transport study in different devices 7

Figure 2.1 The lower end structure of the carbon probe.....10

Figure 2.2 The upper end structure of the carbon probe.....11

Figure 2.3 The power supply system of the carbon probe 23

Figure 2.4 The discharge current of the carbon probe (a), and the measured C_{II} (b) and C_{III} (c) light emission at the same location and operating condition 14

Figure 2,5 The magnetic field perturbation by the carbon probe 16

Figure 2.6 The single channel optical system 18

Figure 2.7 The arrangement of the HBT diagnostics and the toroidal field (TF) coil system (vertical view) 21

Figure 2.8 The cross-section of the HBT machine showing the vacuum chamber, the coil system and the poloidal flux contours (dotted line) for typical free-boundary equilibria 22

Figure 2.9 The loop voltage (for the parallel bias case) obtained in the old (a) and the new (b) vacuum chambers.....24

Figure 2.10 The timing sequence of the major plasma parameters (both parallel and reverse bias cases) and the discharge current of the carbon probe.....25

Figure 3.1 Diffusion of test particles in velocity space.....27

Figure 3.2 The different relaxation time of the C^{+}(Z=1) ion with protons and electrons as a function of temperature.....36

Figure 3.3 The different relaxation time of the C^{++}(Z=2) ion with protons and electrons as a function of temperature.....37

Figure 3.4 The coordinate system used in the diffusion model 39

Figure 3.5 The reciprocal of the ionization rate of carbon ions at different ionization states 42

Figure 3.6 The time ratio for two successive stages of ionization of charge Z and $Z+1$.....43

Figure 3.7 The reciprocal of the radiative recombination rate of carbon ions

at different ionization states 44

Figure 3.8 The experimental data for the rate coefficient of carbon ions at different ionization states.....45

Figure 3.9 The relationship of ionization and recombination between the ith and the other two adjacent ionization states.....46

Figure 3.10 (a) The estimate of the ionization and recombination times for different ionization states of carbon ions at $n_e = 3 \times 10^{14}$ $(cm^{-3})$and $T_e = 4 \sim 10\,(eV)$; (b) The reduced model for the calculation of C^{+} and C^{++} ion densities in the time scale interest.....47

Figure 3.11 The carbon probe discharge current and the three mathematical models for the source of carbon ions.....50

Figure 3.12 The illustration of the initial condition and the source term for (a)the square-wave function model, and (b)the sine-wave function model 55

Figure 3.13 The comparison of the predicted curves of C_{II} ion density from the three mathematical models 59

Figure 4.1 The C_{II} light measurement and the fitted solution of equation (3.5.11) (solid line) at low toroidal magnetic field (B_t =1.95 (kG)) in (a)the minor-radial and (b)the toroidal directions 64

Figure 4.2 The C_{II} light measurement and the fitted solution of equation (3.5.11) (solid line) at high toroidal magnetic field (B_t =3.5 (kG)) in (a)the minor-radial and (b)the toroidal directions 65

Figure 4.3 The C_{III} light measurement and the fitted solution of equation (3.5.11) (solid line) at low toroidal magnetic field (B_t =1.95 (kG)) in (a)the minor-radial and (b)the toroidal directions 66

Figure 4.4 The C_{III} light measurement and the fitted solution of equation (3.5.11) (solid line) at high toroidal magnetic field (B_t =3.5 (kG)) in (a) the minor-radial and (b) the toroidal directions.....67

Figure 4.5 The parallel diffusion coefficients for C_{II} and C_{III} at different radial and toroidal locations from the source point. Low B_t is for B_t =1.95 (kG) and high B_t is for B_t =3.5 (kG).....72

Figure 4.6 The perpendicular diffusion coefficients for C_{II} and C_{III} at different radial and toroidal locations from the source point. Low B_t is for B_t =1.95 (kG) and high B_t is for B_t =3.5 (kG) 73

Figure 4.7 The perpendicular diffusion coefficients for (a) C_{II} and (b) C_{III} at different toroidal magnetic field 74

Figure 4.8 The solutions of equation (4.3.8) at $x = 1.5$ (cm) and $y = z = 0.0$ from five different toroidal convection velocities. The radial convection velocity is (a)zero and (b)500.0 (m/sec), respectively 81

Figure 4.9 The solutions of equation (4.3.8) at $x = 2.5$ (cm) and $y = z = 0.0$ from five different toroidal convection velocities. The radial convection velocity is (a) zero and (b)500.0(m/sec), respectively 82

Figure 4.10 The solutions of equation (4.3.8) at x=4.7 (cm) and y=z= 0.0 from five different toroidal convection velocities. The radial convection velocity is (a) zero and (b)500.0(m/sec), respectively 83

Figure 5.1 The fit of the measured perpendicular diffusion coefficients using the curves predicted by the 2-D classical transport theory for the C^+ ions at $n_e = 3 \times 10^{14}\,(cm^{-3})$ and $T_e = 4 \sim 8\,(eV)$ 112

Figure 5.2 The fit of the measured perpendicular diffusion coefficients using the curves predicted by the 2-D classical transport theory for the C^{++} ions at $n_e = 3 \times 10^{14}\,(cm^{-3})$ and $T_e = 4 \sim 8\,(eV)$ 113

Figure 5.3 The fit of the measured perpendicular diffusion coefficients using the curves predicted by the 1-D classical transport theory for both the $C^+$and C^{++} ions at $n_e = 3 \times 10^{14}$ (cm^{-3}) and T_e = 4~8 (eV) 114

Figure 5.4 The fit of the measured perpendicular diffusion coefficients using the curves predicted by the 1-D neoclassical transport theory for both the $C^+$and C^{++} ions at $n_e = 3 \times 10^{14}\,(cm^{-3})$ and $T_e = 4 \sim 8\,(eV)$ 115

Figure 5.5 The fit of the measured perpendicular diffusion coefficients using the curves predicted by the Bohm diffusion formula for both the $C^+$and C^{++} ions at $n_e = 3 \times 10^{14}\,(cm^{-3})$ and $T_e = 4 \sim 8\,(eV)$ 116

Figure 6.1 The layout of the four channel optical system..... 119

Figure 6.2 The diagram for Abel inversion 121

Figure 6.3 The inversion map with scale 1:2..... 122

Figure 6.4 The geometry for the improved Abel inversion..... 124

Figure 6.5 (a)The input photon flux is converted into output voltage by PMT and amplifier; (b)The photocathode spectral response

characteristics 132

Figure 6.6 The geometry used to calculate the inward minor - radial H_2 flux 136

Figure 6.7 (a)The four chordal measurements of H_α light emission; (b)The inverted H_α emissivity in four zones. This is the parallel bias case 139

Figure 6.8 (a) The inward minor-radial flux of H_2 molecules; (b)H_α emissivity profile evolution, two different views (parallel bias case) 140

Figure 6.9 (a) The line integrated electron density from the CO_2 interferometer; (b)The total plasma current from the Rogowski coil. Both for parallel bias case at pressure 10 *mTorr* 141

Figure 6.10 (a)The four chordal measurements of H_α light emission; (b)The inverted H_α emissivity in four zones. This is the reverse bias case 144

Figure 6.11 (a) The inward minor-radial flux of H_2 molecules; (b) H_α emissivity profile evolution, two different views (reverse bias case) 145

Figure 6.12 (a) The line integrated electron density from CO_2 interferometer; (b) The total plasma current from Rogowski coil. Both for reverse bias case at pressure 10 *mTorr* 146

Figure A.1 An instability measurement from C_{II} light emission. 160

Figure A.2 An example of an unstable shot. 161

List of Tables

Table 1 Parameters for the Columbia HBT 2

Table 2 The collision time of carbon ions with plasma protons and electrons 35

Table 3 The Coulomb logarithm $ln\Lambda_{cp}$ of the carbon ions at the different plasma densities and temperatures 98

Table 4 The $(\Omega_c \tau_{cp})^2$ factor of the carbon ions for different plasma densities and temperatures at $B_t = 2.0\,(kG)$ 101

Table 5 The $(\Omega_c \tau_{cp})^2$ factor of the carbon ions for different plasma densities and temperatures $B_t = 3.5\,(kG)$ 101

Table 6 The particles recycling time and energy confinement time at different fill pressure (parallel bias case) 149

Table 7 The particles recycling time and energy confinement time at different fill pressure (reverse bias case) 149

ACKNOWLEDGMENTS

I would like to express my sincere thanks to my advisor, Professor T. C. Marshall, for his continued guidance, interest, support and encouragement throughout the course of this research.

I would like to thank Professor M. E. Mauel, especially for the useful introduction and help in the H_α light measurement, and Professor G. A. Navratil for many suggestions and discussions.

I would also like to say thanks to many people at the lab who supported my research effort, and I hope that I don't miss too many of them. I am very appreciative of the help from Tom Ivers who showed me the HBT operating procedure and the computer system, from Dr. Vijiya Sanka who operated the CO_2 interferometer system during my data acquisition, and from David Gates who provided me with the results of Thomson scattering measurement.

I am grateful to the technical support staff of the Columbia University Plasma Physics Laboratory for their assistance and to the following people in particular: Nick Rivera for the day to day running of the HBT machine, Steve Lopez for his tremendous help and excellent suggestion on the design of the carbon probe, Moe Cea for his years of technical experience to solve practical problems, Harold Wadlegger for his consummate skills in building many of the experimental components, Hank Alvestad for his smart idea on the electrical connection of the carbon probe, and Tony Novinsky for servicing and repairing some of the electronic equipment. I have learned much practical knowledge from them.

I will never forget my friends in the Plasma Laboratory. Those who gave their friendship are too numerous to list, and I thank them all.

Research was found by the Department of Energy under the contract DE-FG02-86ER53222.

This thesis is dedicated to my wife, my love, Tong-Bi Pei, who showed unfailing patience, confidence, understanding and help throughout the course of this long research, especially in the preparation of this manuscript. I also thank my parents by their sacrificing and supporting me through undergraduate school.

None of the ways observed or described by us, in which things happen or events occur, is the Master Way by which nature works. No word or name can disclose nature's deepest secret. Creation began in an event which is not identified and therefore has no name. All creatures, nevertheless, can be traced to a common mother or matrix, something to which such words as "mother" or "matrix" can be applied.

LAO TZU (604? - 531? B.C.)

Chinese philosopher

What I value in life is quality rather than quantity, just as in Nature the overall principles represent a higher reality than does the single object.

ALBERT EINSTEIN

CHAPTER ONE
INTRODUCTION

1.1 The History of The Columbia HBT

The Columbia High Beta Tokamak (HBT)[1] is a small-size toroidal plasma device which produces plasmas that fall within the scope of MHD studies. Plasma MHD has had considerable success in describing the phenomena observed as plasmas are generated and heated in toroidal geometry; both MHD equilibrium and stability are commonly used in the design of new and larger devices. The HBT project was begun in 1976 in order to study the physics of tokamak plasmas having high beta: in particular, could such plasmas be generated, and what equilibria could be achieved? It should be noted that in 1976 the toroidal beta of tokamak plasmas was a small fraction of a percent, at least an order of magnitude or more smaller than required for fusion plasma applications. It was proposed to generate plasmas having beta of several percent, and in 1978 the Torus II device (the predecessor of HBT) was operated. After a few years, devoted to diagnostic development, it was found that tokamak-type plasmas of elongated cross section could be generated having average toroidal beta ~ 10%[2]. It is worthy of note that recently the DIII-D conventional tokamak has found that toroidal beta ~ 10% can be produced.

The plasmas produced in Torus II were of limited lifetime, and so in 1982 it was decided to redesign the tokamak and upgrade the pulse-power systems so as to extend the lifetime of the plasma beyond 100 (μsec): this permitted good documentation of the plasma equilibrium conditions[3]. More recently, the magnetic probe diagnostic has been able to detect certain MHD instabilities[4] and study the equilibrium of plasmas formed near or in the *second stability* zone of plasma betas[5].

Although there has been considerable success in understanding the HBT plasma in terms of MHD[6], there have been from time to time a number of reservations or criticisms. The HBT plasma is formed rapidly at relatively high density (compared with other tokamaks), above the Murikami limit[7], and it is also a rather small device contained within a quartz chamber and lacking a limiter. These raise issues such as the contamination of the plasma by impurities, the rapid outflux of energy by neutral collision charge exchange, low magnetic Reynolds number, etc.. As a result, the fusion community has been slow to accept the relevance of HBT research to larger, hotter plasmas. Is HBT a "real" tokamak? One of the objectives of the present study is to examine what happens in the HBT on a microscopic level of collisions and transport.

The typical HBT parameters and the main diagnostics used in the carbon probe experiment are listed in Table 1, and a picture which shows the general layout of the HBT machine (not including the power supply system), is shown in Fig.1.1. The coil system and the diagnostic arrangement will be shown in Fig.2.7 and Fig.2.8 in Chapter Two.

Table 1: Parameters for the Columbia HBT

Major radius, R_0, cm	24	Peak toroidal field, B_t, kG	6
Minor radius, a, cm	≤ 5	Typical q^*	2.0
Toroidal magnetic field, B_T, kG	2 - 5	Toroidal beta, $<\beta>$, %	≤ 3
Elongation, κ	≈ 1	$\varepsilon\beta_p$	≤ 1.0
Ion species	H, D, He	Typical discharge times, μsec	100
Density, $<n_e>$, $\times 10^{14} cm^{-3}$	1 - 5	Energy confinement, τ_E, μsec	$\approx 20 - 100$
Temperature, $<T_e>$, eV	4 - 10	Diagnostics: CO_2 interferometer,Thomson	
Peak plasma current, I_p, kA	20	scattering, magnetic probe, carbon probe.	

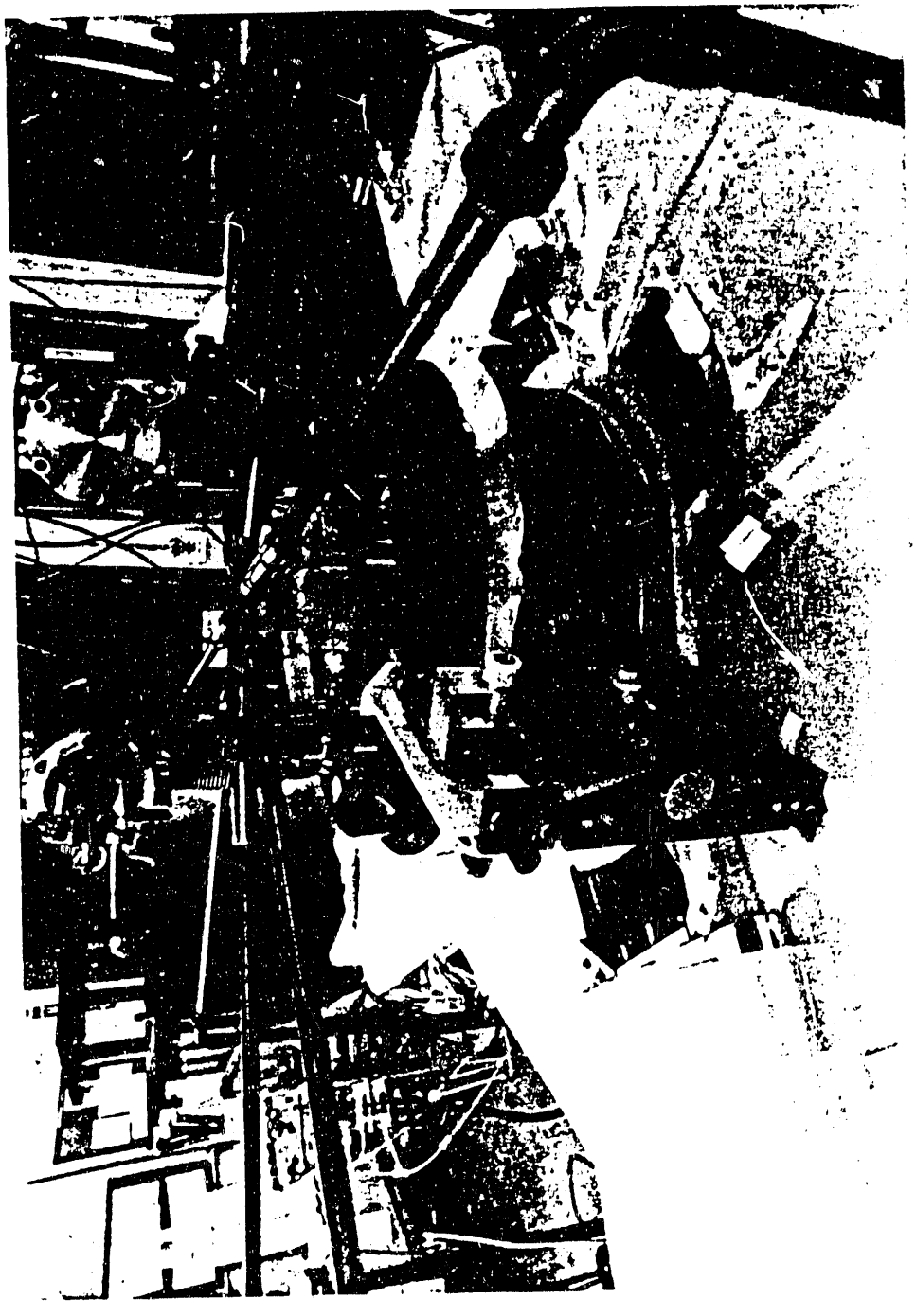

Figure 1.1 The general layout of the HBT machine.

1.2 The Objective of The Carbon Probe Experiment

In the present study, a group of "test particles" (actually carbon ions) is injected into the plasma, and we analyze the carbon ion emitted light in order to determine how these ions diffuse along and across the magnetic field lines which contain the plasma. The plasma is itself collision-dominated, that is, the collision mean free path is much smaller than the toroidal circumference, and therefore the carbon ions random-walk their way across the field lines by scattering off the dominant ion species, protons. We ask the question: is this process in HBT described by the classical mechanism mentioned above, or are there other effects, e.g. plasma flows or field errors which cause the plasma to move differently? It is worth noting that in another toroidal device (Spheromak)[8], a similar experiment done in a plasma having similar conditions to HBT found that the ion impurity diffusion was ~ five times the Bohm ("anomalous") diffusion. However, Spheromak is not generically a tokamak; it is a form of reverse-field pinch[9].

Another reason to do the carbon ion diffusion experiment is to develop a different technique to sense plasma macroscopic motion. An MHD instability, for example, will cause the plasma to shake in a characteristic way, and this motion can be detected by examining the emitted impurity light, which is generated in the locality of the carbon ion source. Presently, instabilities are detected using a magnetic probe; therefore one is actually sensing the fluctuation of the magnetic field which is "tied" into the plasma to some degree, rather than the actual plasma motion. It would be useful to validate the magnetic probe measurement with another diagnostic. In fact, we show an instability measurement using carbon probe in this manuscript, however the abrupt termination of the HBT experiment did not permit full exploitation of this technique.

Finally, the optical sensing system was also capable of additional studies, in particular the examination of light emitted by neutral hydrogen. The neutral gas arises

from a flux of gas from the chamber wall, which then flows into the hot plasma and ionizes. Some neutrals, however, merely charge-exchange resonantly on the plasma ions (protons), and this results in a recycling of particles between the plasma and the walls. This represents an important energy loss to the plasma, and our observations permit us to compute a characteristic time for this energy loss process. We find that it occurs on a timescale comparable with the plasma life time. Therefore, the recycling of the hot plasma ions with the cold neutrals could be an important mechanism for the loss of the plasma energy, together with electron heat conduction and impurity radiation.

1.3 The Method of The Carbon Probe Experiment

The carbon ions are released from the discharge of a carbon tipped probe which consists of a hollow graphite cathode coaxial with a stainless steel anode pin. The probe is vertically inserted into the vacuum chamber, and is located at the magnetic axis of the plasma during the time scale of interest. A bench test showed that both C^+ and C^{++} can be produced during the source discharge; later on, due to the reionization by plasma electrons, part of the C^+ ions will be ionized to C^{++} state. The recombination of either C^+ or C^{++} can be neglected because of the short time duration of the plasma. The spectral light emission from C^+ ($C_{II} = 4267\ A$) and C^{++} ($C_{III} = 4647\ A$) is collected by a single channel optical system, which includes the focusing lens, the optical fiber, the monochromator and the photomultiplier (PMT). The diffusion coefficients of carbon ions are obtained by numerically fitting of the temporal evolution of the spectral light signal measured at different distances from the probe, along a direction either parallel or transverse to the magnetic field.

A number of other spectroscopic techniques have been devised to monitor either the spatial or the temporal evolution of test particles to study the particle confinement in devices, such as Alcator C [10], TEXT [11], TFTR [12], Proto S-1/C Spheromak [13]. The impurities used in these experiments includes a wide range, such as ions of Sc, Au,

Si, Ti, Ge, C etc.; they all are uniquely identifiable via their characteristic line radiations. The Laser ablation and gas puff techniques were used in most large tokamaks. A carbon probe technique similar to ours was used in the Proto S-1/C Spheromak. Fig.1.2 shows a summary of several of these experiments performed at different tokamaks, including the Columbia HBT. The diffusion coefficients, $D_{\perp}$, found in most of the experiments, are on the order of $1.0 - 10.0$ (m^2/sec). The convection velocity, c_v, used in the fitting of the measured spectral light emission by the impurity ions, differs for different machines; however, it varies between zero and 10.0 (m/sec).

1.4 The Outline of This Report

In this report, we first (in Chapter Two) give a brief description of the general layout of the carbon probe experiment, including the probe structure and power supply, the probe perturbation, the optical system and other diagnostics used in this experiment.

In Chapter Three, a diffusion model of the carbon ions is introduced, including the calculation of the different relaxation times for the carbon ions, three mathematical models for the source discharge of the probe, and the analytical solutions of the continuity equation for each model.

The observation and the fitting of the spectral light signal of the carbon ions at different ionization states is presented in Chapter Four. Convection effects and error analysis are also discussed in this chapter.

Chapter Five presents the interpretation of the carbon ion diffusion data in the HBT plasma. Both of the classical and the neoclassical impurity transport theories are presented there. Bohm diffusion is also briefly discussed.

The H_α light measurements are presented in Chapter Six, including a description of the multichannel optical system, the inversion and reconstruction of the H_α light emissivity. Based on that, the calculations of the minor-radial influx and the recycling

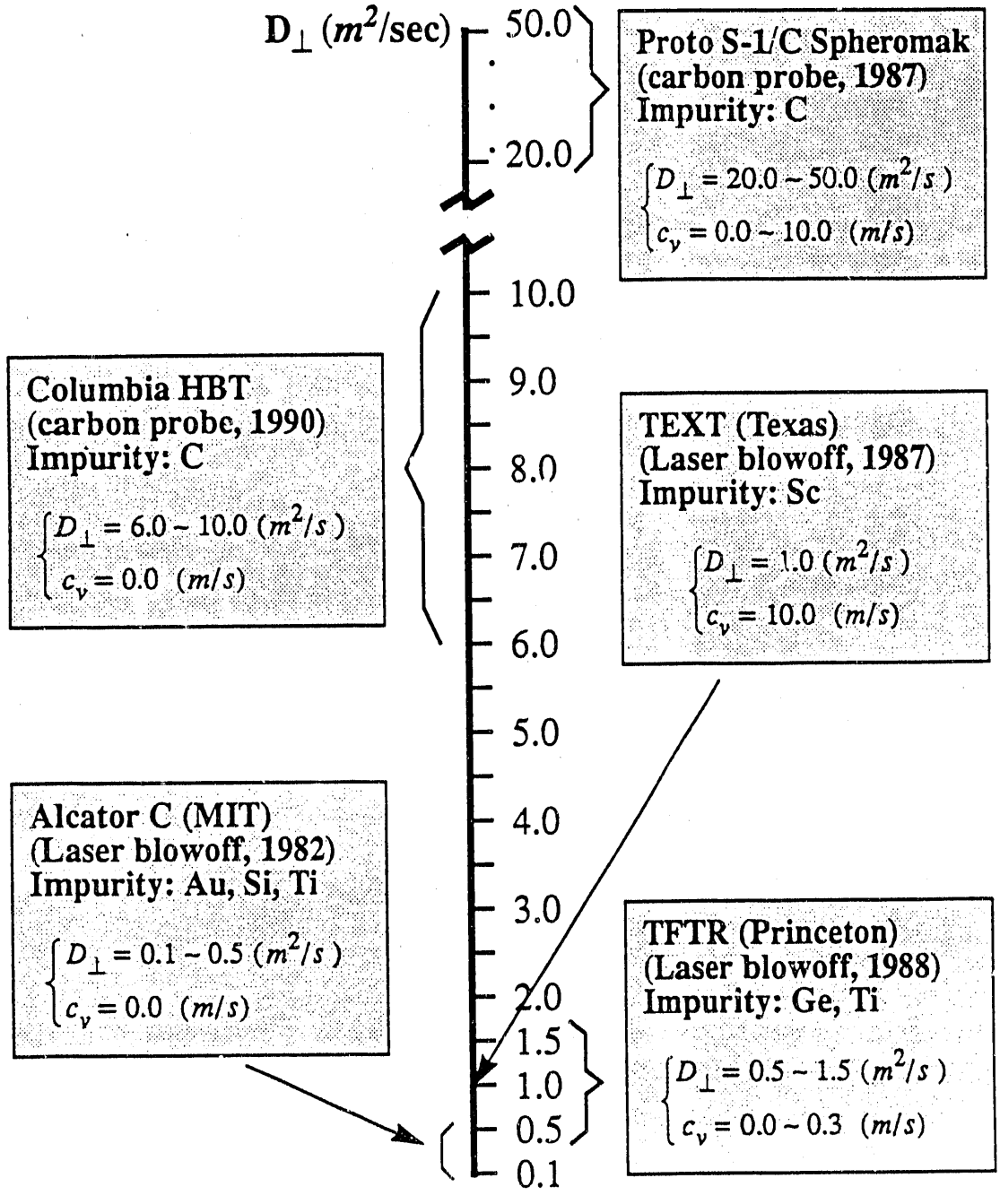

Figure 1.2 The summary of the impurity transport study in different devices .

time of the neutral hydrogen gas is also discussed for both parallel and reverse bias cases of HBT.

Chapter Seven summaries the major results for both of the carbon ion and the H_α light measurements.

In the appendix, we discussed the observation of a macroscopic instability of the HBT plasma using the carbon probe technique. An instability-like shot, obtained in the old vacuum chamber and detected only by the C_{II} light measurement, is presented.

CHAPTER TWO
CARBON PROBE TECHNIQUE AND EXPERIMENTAL SETUP

The basic technique used to measure the carbon impurity diffusion coefficient is to inject a group of carbon ions as test particles into the HBT plasma via the carbon probe discharge, and monitor the spectral light emission from carbon ions (either C^+ or C^{++}) at different directions and locations.

2.1 Carbon Probe Construction

The carbon probe consists of a hollow graphite cathode (9.5 (mm) diameter and 9.5 (mm) length) coaxial with a stainless steel (s.s.) anode pin (1.0 (mm) diameter and 10.0 (mm) length), see Fig.2.1. The graphite cathode is screwed on a tapped s.s. holder which is used to make good electrical contact between the stripped wires of $RG-174$ coaxial cable and the graphite tip. A smaller diameter but longer quartz tubing is nested into a larger diameter but shorter one which is used to keep the s.s. holder on the center line. There is a tiny hole on one end of the holder into which a short piece of wire is inserted and soldered. The center conductor of the coaxial cable is soldered to the s.s. anode pin in the same way. All of these wires are covered by shrinkable tubing to obtain better electrical insulation. The remaining volume inside the quartz tubing is filled with vacuum epoxy.

The probe is vertically inserted into the vacuum chamber. The upper end construction is shown in Fig.2.2. The center conductor and stripped wires of the coaxial cable are soldered to two pieces of wire (#20AWG) individually. A thicker insulation tubing is placed over the center wire which is longer than the grounded one to keep the high voltage perfectly isolated. Vacuum epoxy is also used for sealing. A delicate electrical connector plug (which is not shown on the figure) is especially made for the upper end to link the firing system to the probe.

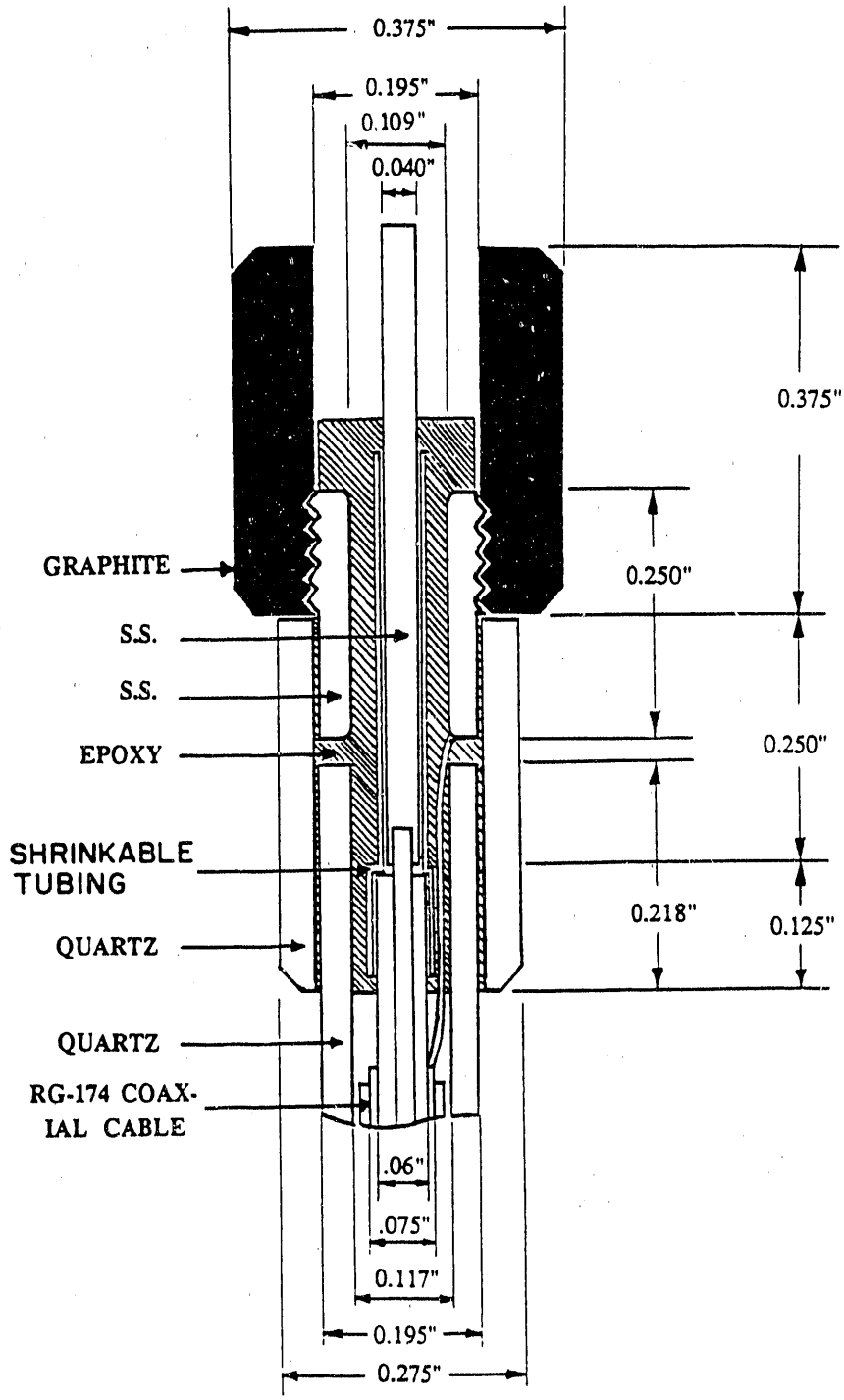

Figure 2.1 The lower end structure of the carbon probe.

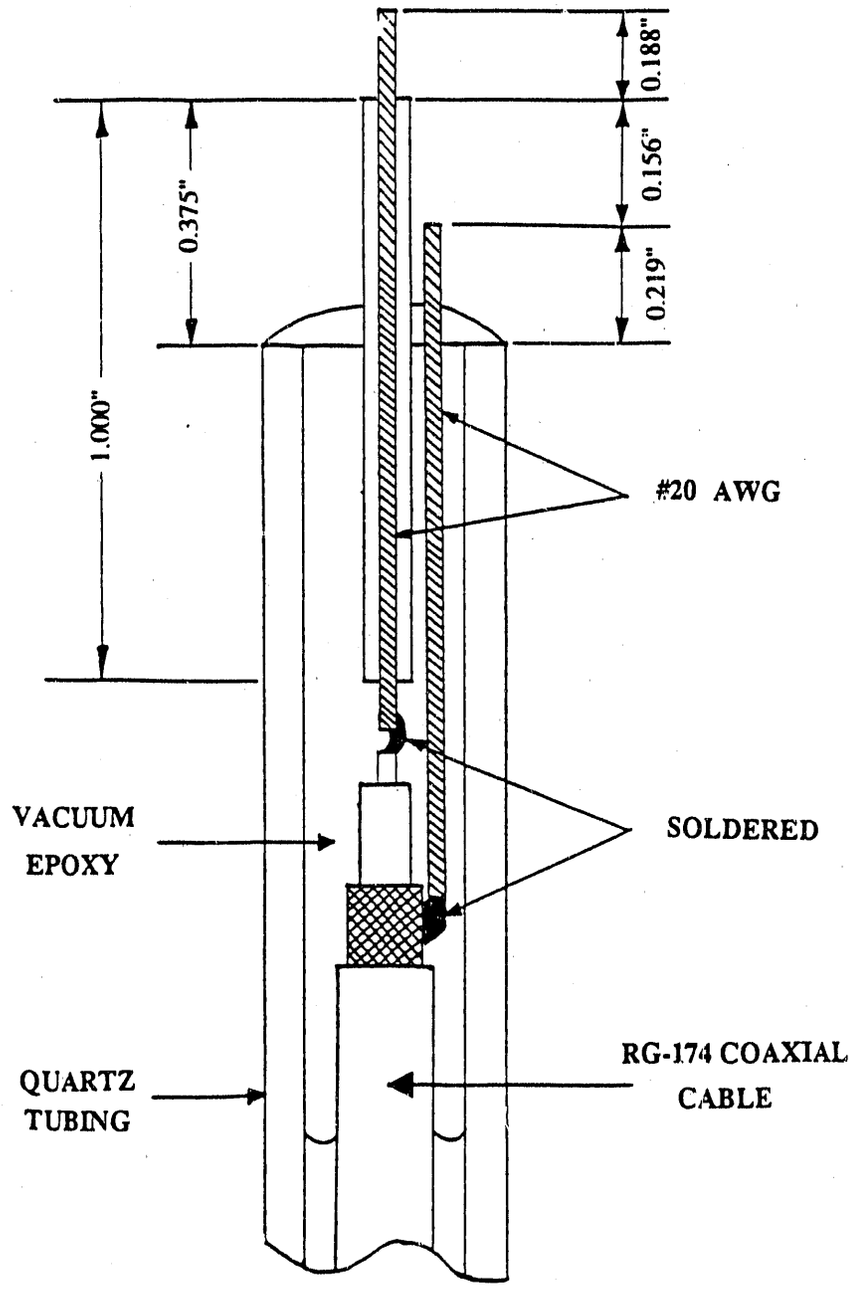

Figure 2.2 The upper end structure of the carbon probe.

2.2 Carbon Probe Operation

The carbon probe is fired by a 20 (kV), 1.0 (μF) capacitor, shown in Fig.2.3. Typically the capacitor was charged up to 10 ~ 15 (kV) and discharged by firing an ignitron. A 1:1 transformer is used to isolate the triggering mechanism from the plasma potential, and the coaxial output feed is wound about 50 turns around an iron core, which provides additional inductive isolation for the circuit from any high voltage potential in or around the vessel during the HBT discharge. In order to get the desired discharge pulse shape we first tested the carbon probe in a small vacuum chamber and found a ring of the discharge since the whole circuit is under–damped. From the width of the discharge current pulse the inductance of the whole system can be obtained, roughly 6.0 (μH), which is partially in the firing circuit and partially in the cable and probe. The critical damping resistance is about 5.8 (Ω), but it reduces the peak current by a factor of 4. So finally a 2.0 (Ω) resistor is used in the main circuit as a compromise between oscillation damping and peak discharge current. The pulse shape is shown in Fig.2.4(a). The C_{II} light signal from a discharge of the carbon probe is shown in Fig.2.4(b), and Fig.2.4(c) is for the signal of C_{III} light emission.

There are two different operating modes for the carbon probe: the static ablation mode by the plasma ions while the carbon tip is at the same floating potential as the plasma, and the firing mode when the carbon tip is at negative potential with respect to the anode pin. In the first mode the ablation results from the sputtering of plasma ions with their thermal energy. In the second mode an arc is formed between the circumference of carbon tip and the center pin. Plasma protons in the arc region are accelerated to much higher energy than their thermal energy, hitting the carbon tip surface and release more (about 5 ~ 10 times) carbon ions than the ablation mode[14].

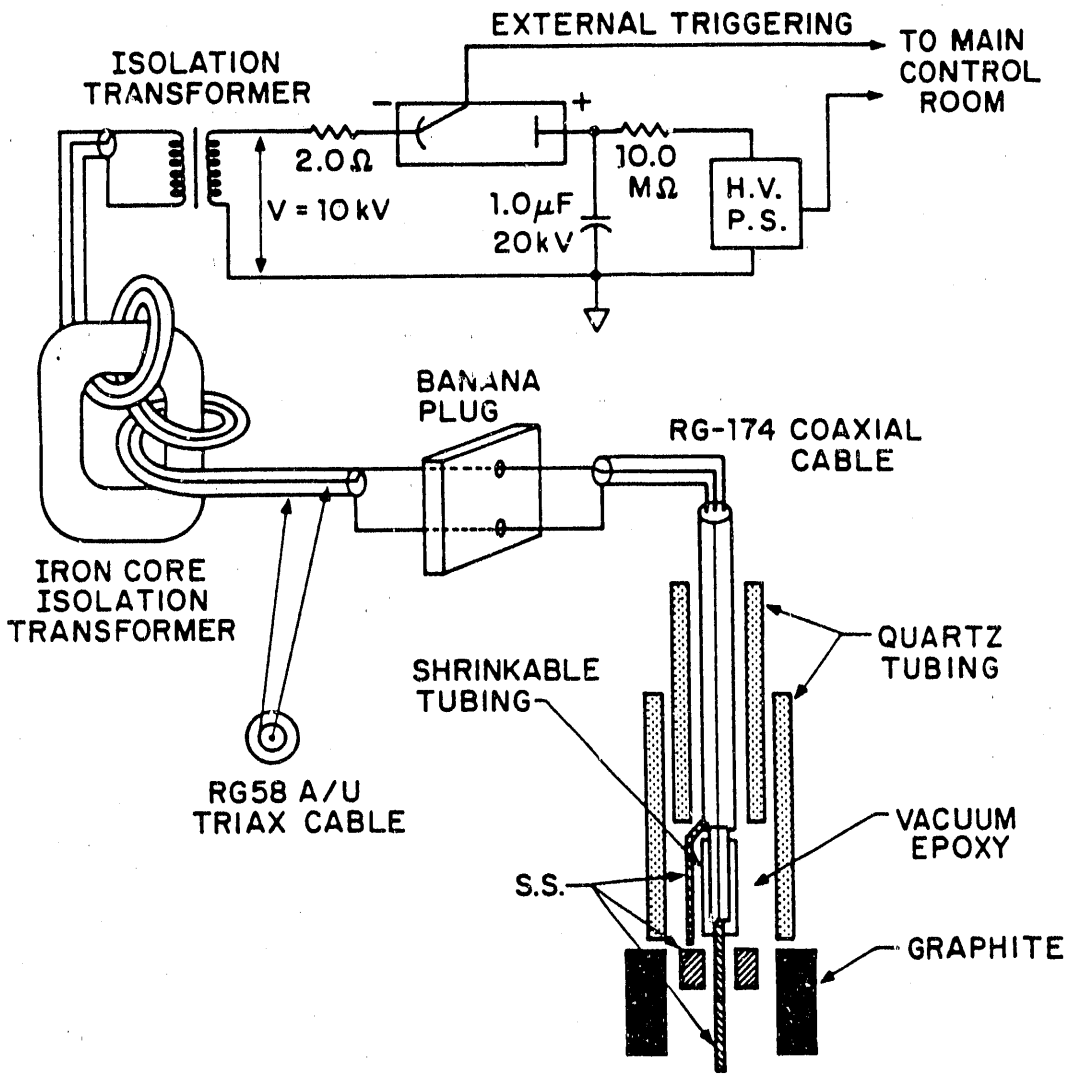

Figure 2.3 The power supply system of the carbon probe .

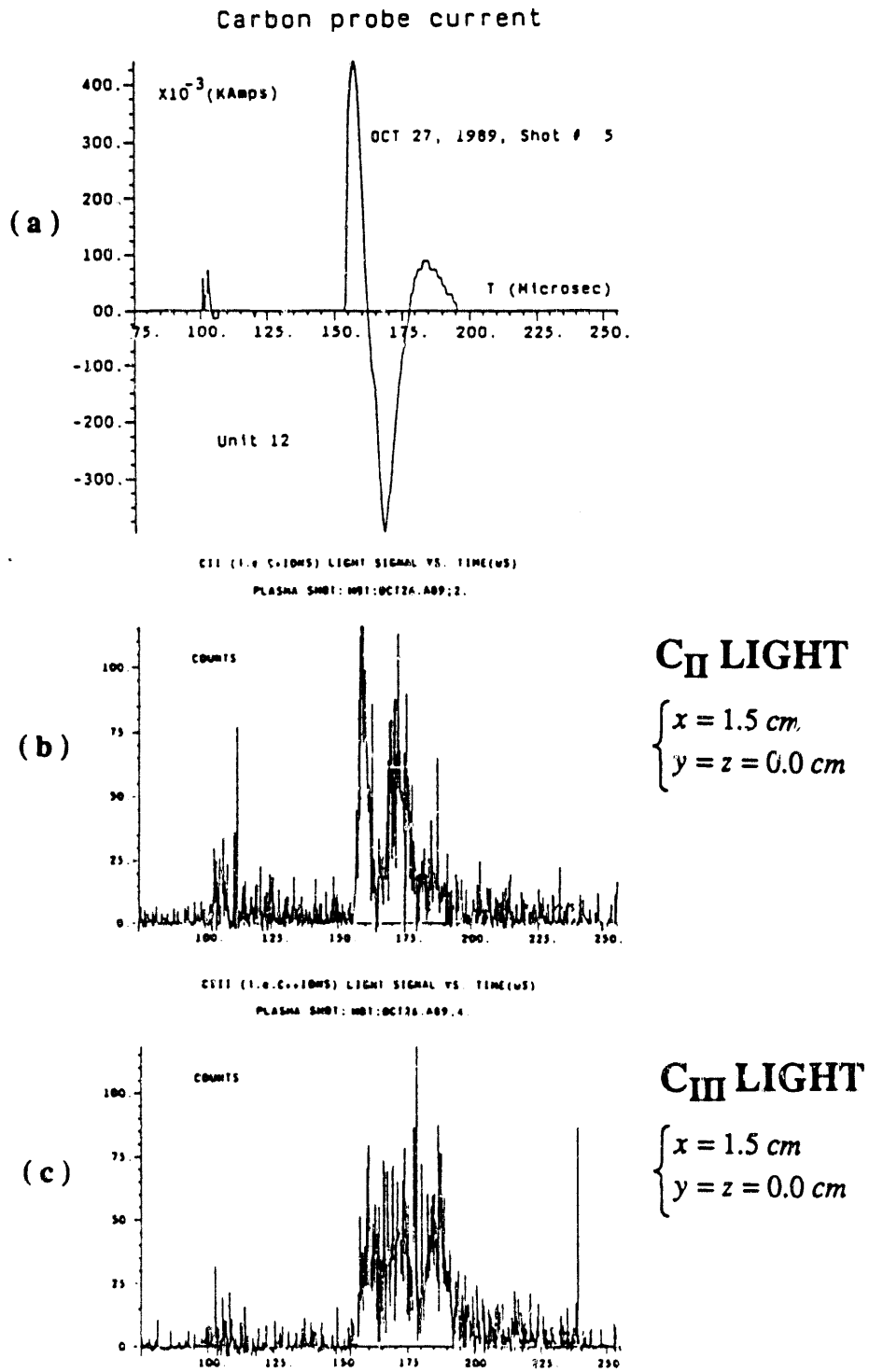

Figure 2.4 The discharge current of the carbon probe (a), and the measured C_{II} (b) and C_{III} (c) light emission at the same location and operating condition .

2.3 Carbon Probe Perturbation

One of the advantages of HBT plasma is that we can insert a probe into the plasma because of its relatively low temperature and short discharge time. But this will also cause some perturbation of the plasma.

2.3.1 Density Perturbation

The density perturbation depends on how many carbon ions are released from the carbon tip during its operation. From line strength comparison of spectral light emission between carbon ions and excited neutral hydrogen (H_α light), the density of carbon ions is in the range of $10^{10} \sim 10^{11}$ (cm^{-3}), which is $10^2 \sim 10^3$ times lower than the plasma density. The Z-effective of the mixture of plasma ions and carbon ions is still close to that of the plasma without injected carbon, so the density perturbation does not effectively change the global parameters of HBT plasma.

2.3.2 Magnetic Field Perturbation

When the carbon probe is working in the discharge mode, its arc current can also produce a perturbation of the magnetic field. As shown in Fig.2.5, the discharge current mainly produces an azimuthal B-field around the central anode pin (similar to the geometry of toroidal field coil system), which can be estimated using the formula

$$\Delta B = \frac{\mu_0 I}{2\pi r} \tag{2.3.1}$$

With the discharge current $I \sim 400\,(A)$, and the average radius $r \approx 2.5\,(mm)$ (inside the carbon tip), then $\Delta B \approx 320.0\,(Gauss)$. But when $r > a = 5.0\,(mm)$ (outside the carbon tip), $\Delta B = 0$ according to Ampere's law because the total current passing through the loop (shown as the dotted line in Fig.2.5 is zero. Even considering that some arc may exist outside the carbon tip a little bit, the perturbation B-field will drops as r^{-3} using a magnetic dipole model. More detailed calculation. for this case, indicates

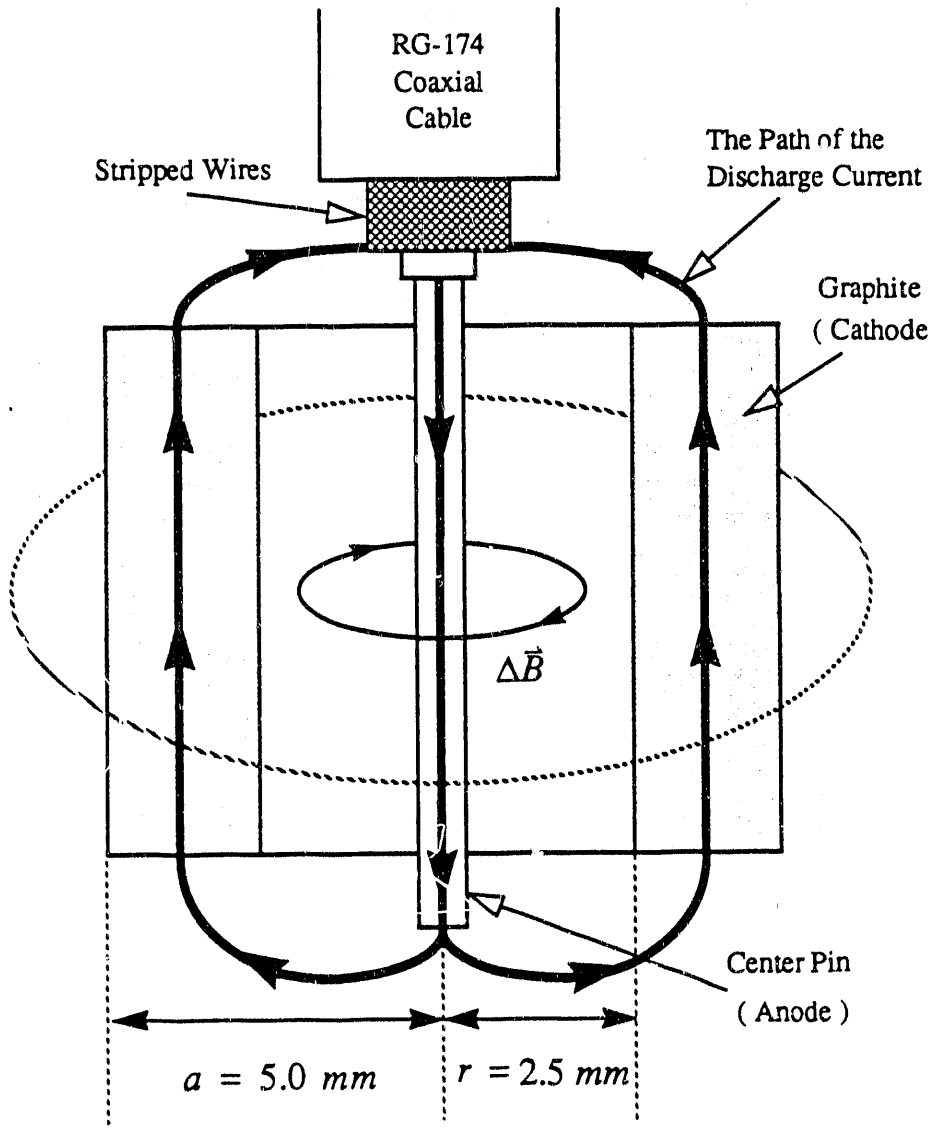

Figure 2.5 The magnetic field perturbation by the carbon probe .

that for $r \geq 1.5$ (cm) the perturbation will be greatly reduced and $\frac{\Delta B_t}{B_t} \leq 1$ %, where $B_t = 2.0$ (kG) is the unperturbed toroidal magnetic field. So the perturbation field due to the discharge current of carbon probe is localized and can be neglected.

2.4 The Ratio of C_{II} and C_{III} Light Emission

The carbon probe was first tested in a small vacuum chamber filled with neon gas at different pressures. The branch ratio of C_{II} (4,267 A, emitted by C^+ ions) and C_{III} (4,647 A, emitted by C^{++} ions) is about 50% under the average of several shots. Because of the ringing of the probe discharge current the light signals also show multiple peaks, and the relative level of each peak is roughly (with 30% to 40% fluctuation) proportional to the corresponding peak of discharge current. This provides a very useful knowledge in the numerical fitting of diffusion model which will be discussed in chapter 3.

2.5 Single Channel Optical System

The basic layout of the carbon probe experiment is shown in Fig.2.6. The probe is vertically inserted into the HBT plasma through a flange which is electrically isolated from the toroidal field coil system and the probe itself. The probe axis is 2.54 (cm) away from the axis of the top and bottom ports, allowing us to rotate the probe around the port axis to get an arbitrary radial position (from $R_0 + 2.54$ (cm) to $R_0 - 2.54$ (cm), where $R_0 \simeq 24.0$ (cm)) to match the magnetic axis.

The spectral light emission from carbon ion is collected by a wide angle Nikkon ($f/2.0$, 28 (mm)) camera lens and focused on a 1-D optical fiber array. The lens is located about 20.0 (cm) below the vacuum chamber. The camera lens and the optical fiber array holder are mounted together , both located on the port axis. This allows us to rotate the whole lens set around the axis to observe diffusion of carbon ions either the radial or toroidal direction. A sliding rectangular aperture, which allows the light

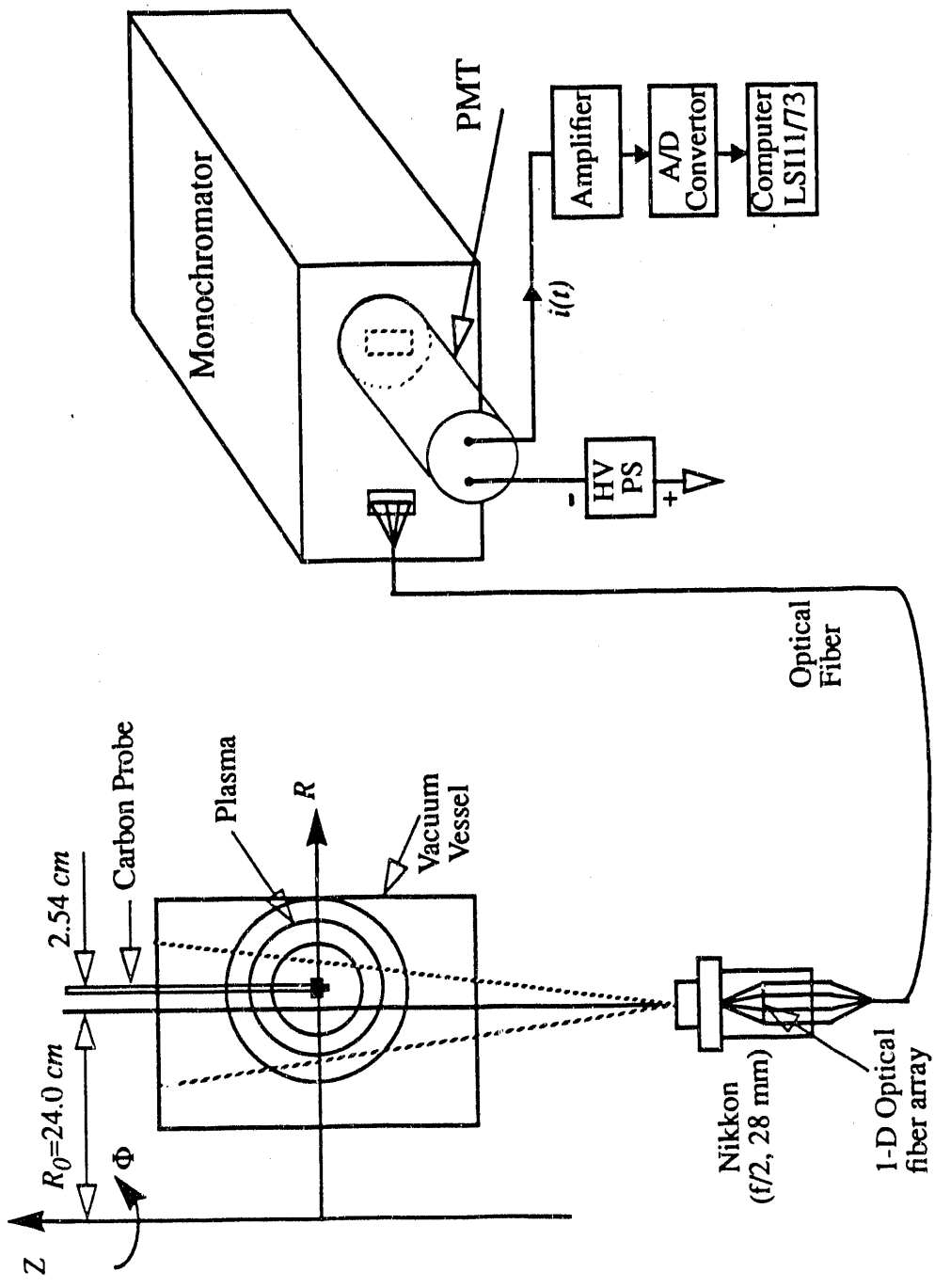

Figure 2.6 The single channel optical system .

focused only on the end of one optical fiber (0.6 (*mm*) diameter), is used to confine the field of view into a small region of plasma (about 6.6 (*mm*) since the demagnification of the camera lens is 11:1). The light is coupled to the monochromator (f/8.5, 50 (*cm*)) through a long (about 10 meters) optical fiber and then amplified by a photomultiplier tube (PMT). Because of the mismatching of the f-number between the optical fiber and the monochromator, a big loss of light ($\approx$ 91 %) exists. This will be discussed in more detail later in chapter 7. From this single channel configuration we can get only one point of view in each shot. To obtain the light emission profile several shots must be taken under the same conditions. This is somewhat undesirable because of the fluctuations from shot to shot, and several shots are needed to take the average. A multichannel system has been developed, but is good for only the H_α light measurement, since the H_α intensity is much higher than that of the carbon lines. In the single channel case, for the reason mentioned above, the measurements of the temporal evolution, rather than the spatial profile, of carbon light were used to obtain the diffusion coefficients because the later one has too much errors.

2.6 Other HBT Diagnostics and Operations

Many diagnostics have been developed and installed on HBT. Here only those which relate to the carbon probe experiment are listed and briefly discussed.

a. Rogowski Coils: These measure the total plasma current and the currents in all the coil systems. These currents are extremely important to monitor the discharge of each capacitor bank, the triggering and timing of the whole plasma programming procedure, and to judge the quality and reproducibility of the plasma.

b. Internal Magnetic Probe: This measures the internal plasma magnetic field structure. The probes are inserted both vertically and horizontally into the plasma with 3-D coil arrays to measure the three different components of internal magnetic field. These measurements can be used not only to plot the time evolution of each B-field com-

ponent, but also to determine the poloidal flux contours, plasma current density contours, toroidal field contour and the q-profile[15].

c. Thomson Scattering Diagnostic: This is used to measure both plasma temperature and the density profile at ten radially separated locations on the midplane of the machine at one time during the discharge[16]. This is a very important diagnostic since it provides the plasma pressure profile. The time evolution of the temperature and density profiles can be obtained by making many reproducible shots and taking one profile at one specific time on each shot. Data from this diagnostic was provided to us by David Gates.

d. CO_2 Laser Interferometer: This is used to measure the line integrated plasma density evolution at two radially separated vertical chords[17]. Data was provided by Dr. Vijaya Sankar.

The general layout of these diagnostics on HBT is shown in Fig.2.7, and the cross section of HBT structure and the location of the vacuum chamber is shown in Fig.2.8. All of the signals produced by the various transducers are collected by the A/D convertors and recorded by the computers in a main data file. There are various programs for the data acquisition, reduction, and plotting which greatly facilitate and accelerate the progress of research.

The original chamber, which is curved at the outside wall, was broken in April of 1989 in the course of these studies apparently from the fatigue accumulation due to the routine venting and pumping. A substitute vacuum chamber with a rectangular cross section was installed in order to complete this research. The main difference between the two vessels is the shape of the vessel cross section. The rectangular one is taller but narrower and allows more neutral gas on the top and bottom regions; it was observed that the plasmas were more stable in the rectangular vessel, for reasons not understood here.

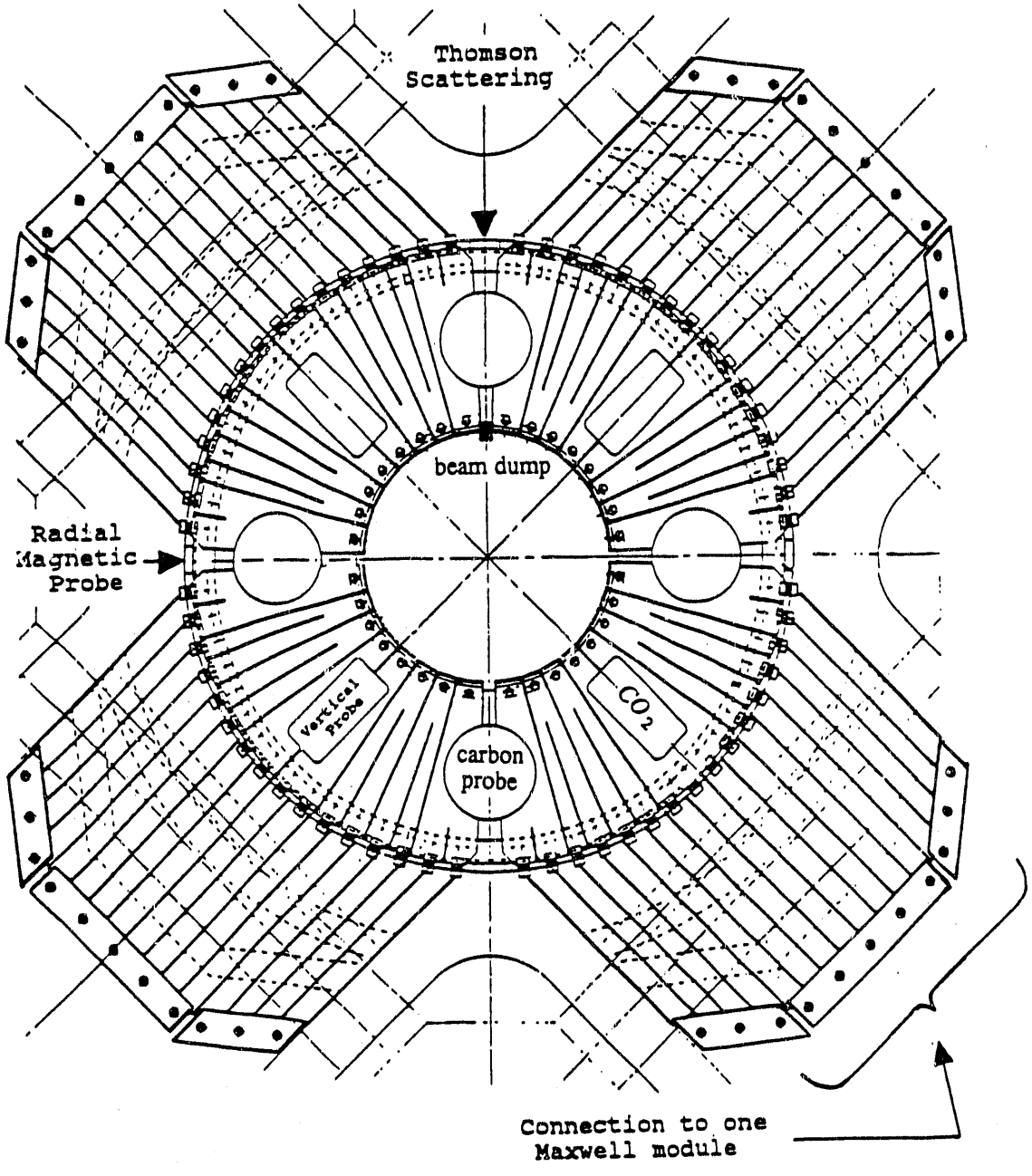

Figure 2.7 The arrangement of the HBT diagnostics and the toroidal field (TF) coil system (vertical view).

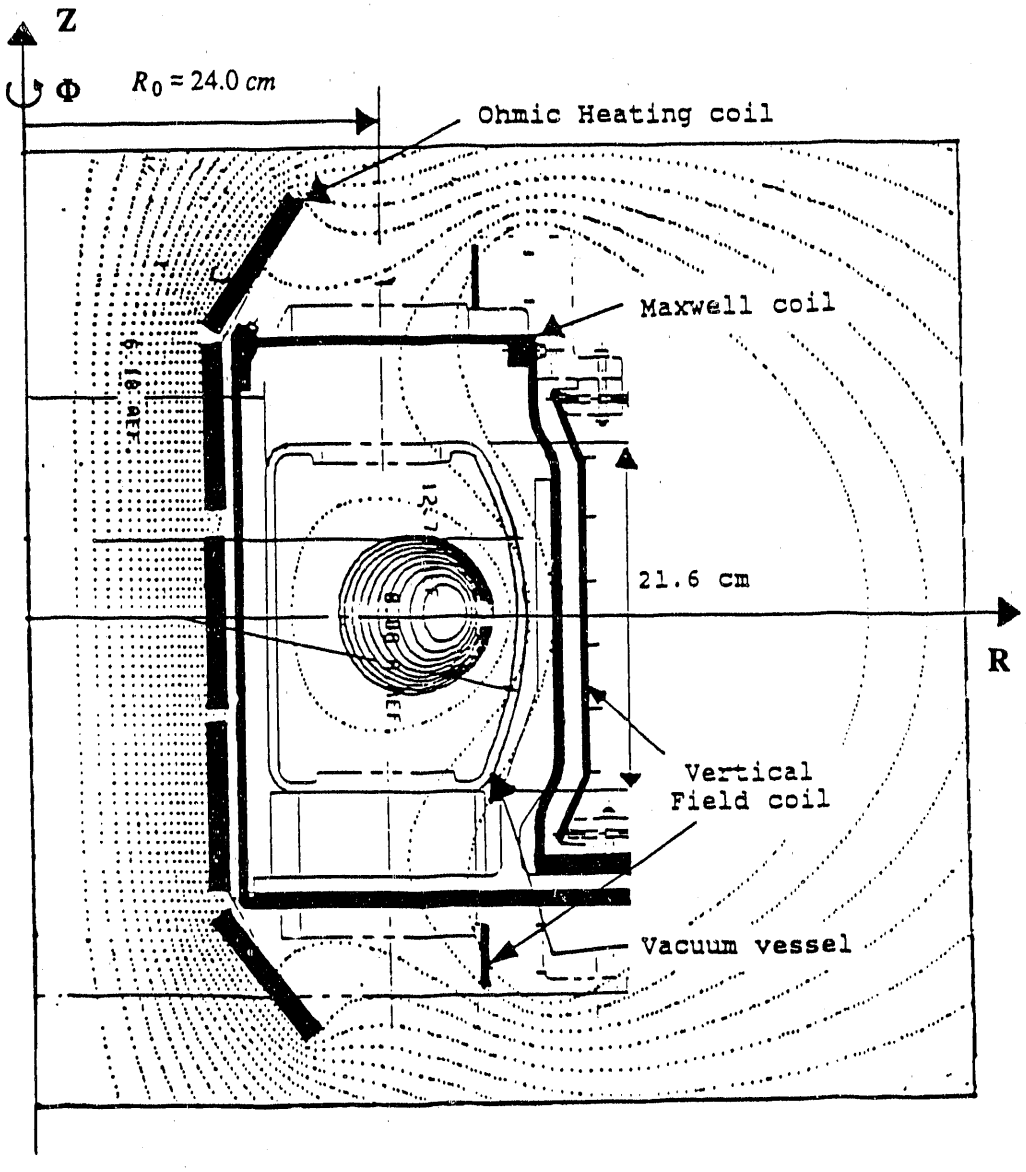

Figure 2.8 The cross-section of the HBT machine showing the vacuum chamber, the coil system and the poloidal flux contours (dotted line) for typical free-boundary equilibria .

The carbon probe experiment was partially performed on the original chamber but the main data base of carbon ion diffusion as well as the multichannel H_α light measurement was set up on the new vessel. The Thomson scattering diagnostic system could not be attached to the new chamber because there is no side port opening on the inner wall to put the beam dump. Comparing the loop voltage obtained in both the old and the vacuum vessels, as shown in Fig.2.9, the electron temperature would appear to be the same for the plasmas produced in the two chambers.

There are two main operation modes for HBT[18]: the parallel toroidal bias field and reverse bias, as shown in Fig.2.10. The most important feature distinguishing the two cases is the time dependance of B_t, the toroidal magnetic field. Parallel bias means that B_t produced by the TFR (toroidal-field-reverse) bank has the same direction as that produced by the Maxwell bank. Reverse bias is the opposite case in which the toroidal field B_t is quickly (in about $1 \sim 2$ ($\mu\, sec$)) reversed by the Maxwell bank resulting in hotter plasma because of a transient turbulent heating process which requires (at least initially) a larger vertical field (VF) to prevent the plasma from striking the outside wall. As the plasma cools, the VF must decay at the same time or else the plasma strikes the inside vessel wall. The parallel bias plasma is sustained ohmically and the VF must be adjusted to increase (with use of its power crowbar) to maintain the plasma centered within the vacuum chamber.

The carbon probe technique was tested in both cases, but finally only the parallel bias operation mode was chosen since the reverse bias plasma is hotter and produces an ablation light signal which is higher than the pulsed signal from the discharge of the carbon probe. In the H_α light measurement both parallel and reverse bias modes are studied, and the neutral particle recycling time is measured for several different fill pressures.

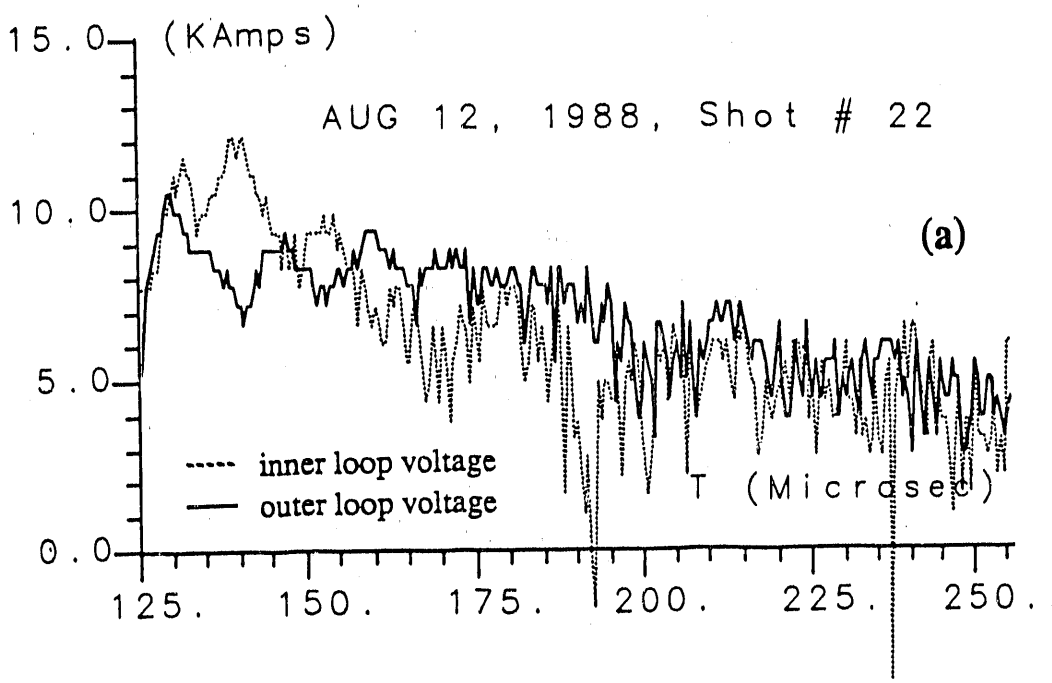

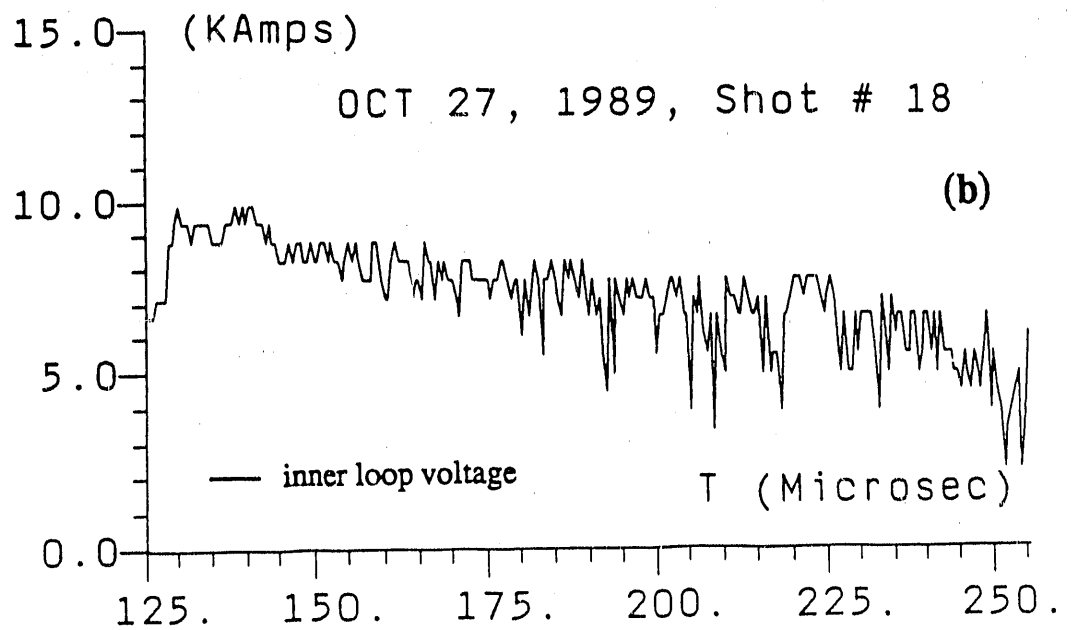

Figure 2.9 The loop voltage (for the parallel bias case) obtained in the old (a) and the new (b) vacuum chambers.

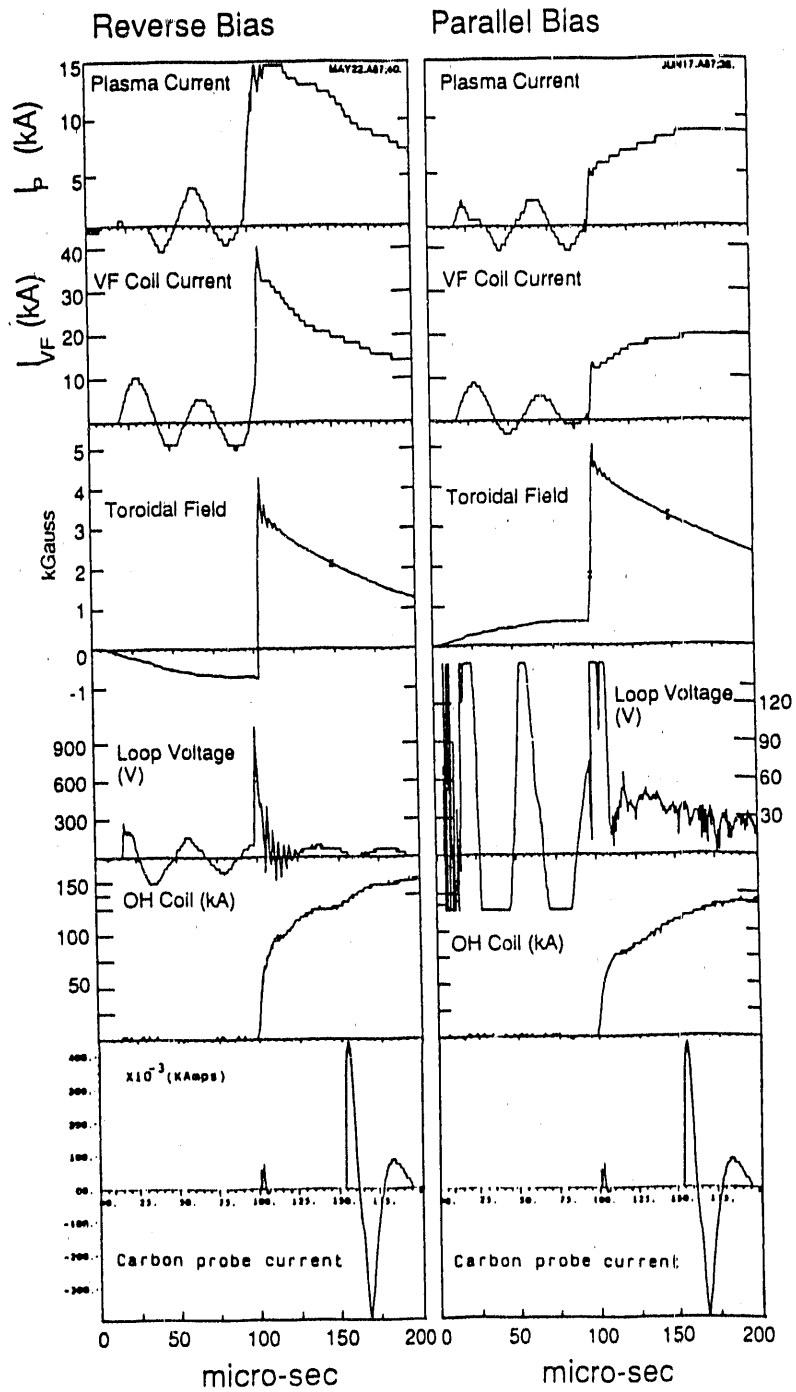

Figure 2.10 The timing sequence of the major plasma parameters (both parallel and reverse bias cases) and the discharge current of the carbon probe.

CHAPTER THREE
DIFFUSION MODEL OF CARBON IONS

The transport of carbon ions in the HBT plasma is explained by a impurity diffusion model. This model, together with some assumptions, allows us to get the analytical solutions of the continuity equation for carbon ions to fit the measured light emission signals.

3.1 Collision Time of Carbon Ions with Plasma Ions and Electrons

The interactions (or collisions) among charged particles are characterized by several kinds of relaxation time which are used to denote the time in which collisions produce a large alteration in some original velocity distribution.

Assume a group of charged test particles, all having velocity in the $\hat{z}$–direction, pass through a plasma which contains the field particles, which may have any velocity distribution. Subscripts t and f will denote "test" and "field" particles unless exceptionally specified. Then these test particles will experience a series of small angle Coulomb collisions with the field particles. In the velocity space the original velocity of the test particle will be progressively altered, analogous to the "diffusion" phenomenon in 3-D configuration space, as shown in Fig.3.1. How fast the diffusion occurs will depend on how many encounters happen per unit time. The total number of test particles is assumed to be much smaller than field particles so that the self collisions among test particles can be neglected.

When the field particles have Maxwellian velocity distribution, Chandrasekhar gave the detailed computation of the diffusion coefficients, for test particles having velocity w_t, in the velocity space as follows[19]:

$$\begin{cases} <\Delta w_{t\,||}> = -A_D\, l_f^2 \left[1 + \dfrac{m_t}{m_f} \right] G\,(\,l_f\, w_t\,) \\[2ex] <(\Delta w_{t\,||})^2> = \dfrac{A_D}{w_t}\, G\,(\,l_f\, w_t) \\[2ex] <(\Delta w_{t\,\perp})^2> = \dfrac{A_D}{w_t}\, [\,\Phi\,(\,l_f\, w_t) - G\,(\,l_f\, w_t\,)\,]\,, \end{cases} \tag{3.1.1}$$

where < > indicates the increase of velocity dispersion of test particles per second. Here || and $\perp$ refer to the direction parallel or perpendicular to the original velocity of the test particle. $<\Delta w_{t\,||}>$ is the so called the "coefficient of dynamical friction" and is usually negative, representing the rate at which the moving test particles are slowed down by interacting with the field particles. This does not increase the dispersion

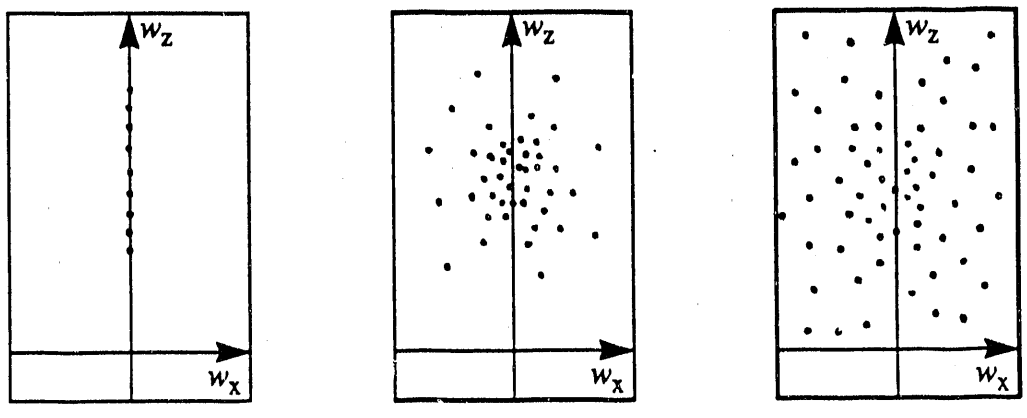

a. Initially

b. After N encounters

c. After 10 N encounters

Figure 3.1 Diffusion of test particles in velocity space.

of test particles in velocity space, but does reduce the speed in the original velocity direction of the test particles. The term $<(\Delta w_{t\,\|})^2>$ is the rate of dispersion in the direction parallel to the original motion of the test particles, i.e. the range of speed reductions in this direction. The third term $<(\Delta w_{t\,\perp})^2>$, which equals twice $<(\Delta w_{t\,x})^2>$ or $<(\Delta w_{t\,y})^2>$ for the case of axisymmetry about $\hat{z}$–direction, is the rate of increase of $(\Delta w_t)^2$ in the perpendicular direction, i.e. the transverse dispersion of test particles in the velocity space.

A_D is given as

$$A_D = \frac{8\,\pi\, e^4\, Z_t^2\, Z_f^2\, n_f \ln \Lambda}{m_t^2}\,, \tag{3.1.2}$$

and $\Phi\,(x)$, the error function, and $G\,(x)$ are defined as:

$$\begin{cases} \Phi\,(x) = \dfrac{2}{\sqrt{\pi}} \displaystyle\int_0^x e^{-t^2}\,dt \\[2ex] \Phi'\,(x) = \dfrac{d}{dx}\,[\,\Phi\,(x)\,] = \dfrac{2}{\sqrt{\pi}} e^{-x^2} \\[2ex] G\,(x) = \dfrac{\Phi\,(x) - x\,\Phi'\,(x)}{2\,x^2}\,. \end{cases} \tag{3.1.3}$$

l_f is defined as follows:

$$l_f = \frac{1}{w_f} = \left[\,\frac{m_f}{2\,k\,T_f}\,\right]^{1/2}, \tag{3.1.4}$$

so the quantity $l_f\, w_t$, which is usually denoted by x, is the velocity ratio of the test particle to the field particle:

$$x = l_f\, w_t = \frac{w_t}{w_f} = \left[\,\frac{3}{2}\,\right]^{1/2} \left[\,\frac{m_f}{m_t}\,\right]^{1/2} \left[\,\frac{T_t}{T_f}\,\right]^{1/2}. \tag{3.1.5}$$

The units used here are the *CGS–Gaussian* system, i.e. e is in *statcoulomb*, n_f in cm^{-3}, m_t in *gram*, and T in *Kelvin degrees*.

From equation (3.1.3) we can get the limits of the functions used in (3.1.1) as x is very small or large

$$\begin{cases} \dfrac{G(x)}{x} \to \dfrac{2}{3\sqrt{\pi}}, \ \dfrac{1}{x}[\Phi(x) - G(x)] \to \dfrac{4}{3\sqrt{\pi}}, \ as\ x \to 0, \\ \dfrac{G(x)}{x} \to \dfrac{1}{2x^3}, \ \dfrac{1}{x}[\Phi(x) - G(x)] \to \dfrac{1}{x}, \quad as\ x \to \infty. \end{cases} \tag{3.1.6}$$

Then the three diffusion coefficients in velocity space will have two important limiting forms:

When $x \to 0$:

$$\begin{cases} <\Delta w_{t\,||}> = 0 \\ <(\Delta w_{t\,||})^2> = \dfrac{2 A_D l_f}{3\sqrt{\pi}} \\ <(\Delta w_{t\,\perp})^2> = \dfrac{4 A_D l_f}{3\sqrt{\pi}}. \end{cases} \tag{3.1.7}$$

When $x \to \infty$:

$$\begin{cases} <\Delta w_{t\,||}> = -\dfrac{A_D}{2 w_t^2}\left[1 + \dfrac{m_t}{m_f}\right] \\ <(\Delta w_{t\,||})^2> = \dfrac{A_D}{2 l_f^2 w_t^3} \\ <(\Delta w_{t\,\perp})^2> = \dfrac{A_D}{w_t}. \end{cases} \tag{3.1.8}$$

Equation (3.1.7) shows that stationary test particles don't experience any friction and their diffusion is isotropic since $<(\Delta w_{t\,||})^2> = \frac{1}{2}<(\Delta w_{t\,\perp})^2>$ and depending on field particles only. This would be the case for the impurity studies in tokamak plasma if we assume that the impurity mass is much large than the proton, or the electron, mass but they all have similar temperature so $x \sim \left[\frac{m_f}{m_t}\right]^{1/2}$ is quite small.

Equation (3.1.8) indicates that fast test particles mainly diffuse transversely since $<(\Delta w_{t\,||})^2>$ is much smaller than $<(\Delta w_{t\,\perp})^2>$. When heavy test particles are scattered by light field particles (i.e. $m_t \gg m_f$) the diffusion tend to be dominated by friction rather than by diffusion since $\left[1 + \frac{m_t}{m_f}\right]$ is a very large factor.

Five kinds of relaxation time are especially interesting in plasma physics and simply discussed here.

a). Deflection Time t_D: This is the time in which collisions gradually deflect the test particle by 90° with respect to their original velocity direction.

Since $<(\Delta w_{t\,\perp})^2>\, t_D = w_t^2 \sin(\chi = 90°) = w_t^2$, where χ is the deflection angle, we have

$$t_D = \frac{w_t^2}{<(\Delta w_{t\,\perp})^2>} = \frac{m_t^2\, w_t^3}{8\pi Z_t^2 Z_f^2 e^4 n_f \ln\Lambda\,[\Phi(x) - G(x)]} \tag{3.1.9}$$

b). Energy Exchange Time t_E: This is the characteristic time in which test particles change their kinetic energy.

Since the energy change for each test particle after a collision is

$$\Delta E = \frac{m_t}{2}\,[(w_t + \Delta w_{t\,||})^2 + \Delta w_{t\,\perp}]^2 - \frac{m_t}{2} w_t^2$$
$$= \frac{m_t}{2}\,[2\, w_t\, \Delta w_{t\,||} + (\Delta w_{t\,||})^2 + (\Delta w_{t\,\perp})^2],$$

the first term in the equation is dominant and the remaining two terms are non-dominant because $|w_t| \gg |\Delta w_{t\,||}|$ or $|\Delta w_{t\,\perp}|$ in each unit time; the square of the energy change per unit time is

$$<(\Delta E)^2> \approx m_t^2\, w_t^2\, <(\Delta w_{t\,||})^2>$$

As the square of total kinetic energy of the test particle is $E^2 = \frac{m_t^2\, w_t^4}{4}$, so finally we can get the energy exchange time as

$$t_E = \frac{E^2}{<(\Delta E)^2>} = \frac{w_t^2}{4\,<(\Delta w_{||})^2>}$$

$$= \frac{w_t^3\, m_t^2}{32\,\pi\, Z_t^2\, Z_f^2\, e^4\, n_f \ln\Lambda\, G\,(\,l_f\, w_t\,)} \tag{3.1.10}$$

Comparing with the definition of deflection time t_D, we can get the following relation

$$\frac{t_D}{t_E} = \frac{4\,G\,(\,l_f\, w_t\,)}{\Phi\,(\,l_f\, w_t\,) - G\,(\,l_f\, w_t\,)} \tag{3.1.11}$$

c). Self Collision Time t_c: This is the same as the deflection time except that now the test and field particles are identical. Since $\chi = l_f\, w_t = \sqrt{3/2} = 1.225$ and $\Phi(1.225) - G(1.225) = 0.714$, we have

$$t_c = \frac{m_t^2\, w_t^3}{0.714 \times 8\,\pi\, Z_t^2\, Z_f^2\, e^4\, n_f \ln\Lambda} \tag{3.1.12}$$

d). Slowing Down Time t_s: This gives the rate $(\frac{1}{t_s})$ at which the mean velocity of the test particles is reduced by collisions.

Since $<\Delta w_{t\,||}>t_s = w_t \cos(\,\chi = \pi\,) = -w_t$, then we obtain

$$t_s = -\frac{w_t}{<\Delta w_{t\|}>} = \frac{w_t}{A_D\, l_f^2 \left[1 + \frac{m_t}{m_f} \right] G\,(l_f\, w_t)} \tag{3.1.13}$$

e). Equipartition Time t_{eq}: is the rate $\left[\frac{1}{t_{eq}} \right]$ at which the energy equipartition is established between test and field particles. That is

$$\frac{d\,T_t}{d\,t} = \frac{T_f - T_t}{t_{eq}},$$

where T is the particle temperature. Spitzer[20] gives the equipartition time as follows

$$t_{eq} = \frac{3\, m_t\, m_f\, k^{3/2}}{8\sqrt{2\pi}\, Z_t^2\, Z_f^2\, e^4\, n_f \ln\Lambda} \left[\frac{T_t}{m_t} + \frac{T_f}{m_f} \right]^{3/2}. \tag{3.1.14}$$

Finally we can put the numerical values into each velocity diffusion coefficient and summarize the results for all of the five kinds of relaxation time in three cases, according to the velocity ratio of test particles to field particles, i.e. $0 \ll x \ll \infty$, $x \to 0$, and $x \to \infty$, where the x is defined in equation (3.1.5). The units in the following formulae are conventional, i.e. the mass m is equal to Am_u where m_u is the atomic mass unit and A is the atomic weight, n is the number density of particles per cubic centimeter (cm^{-3}), the kinetic temperature of particles, T, is in electron volt (eV), and the time t is in (*second*). The self collision time is only discussed in case 1 since it is meaningless for the other two cases.

- Case 1: when $0 \ll x \ll \infty$:

$$t_D = 1.015 \times 10^7 \frac{\sqrt{A_t}\, T_t^{3/2}}{Z_t^2\, Z_f^2\, n_f \ln\Lambda\, [\,\Phi(x) - G(x)\,]} \tag{3.1.15}$$

$$t_E = 2.538 \times 10^6 \frac{\sqrt{A_t}\, T_t^{3/2}}{Z_t^2\, Z_f^2\, n_f \ln\Lambda\, G(x)} \tag{3.1.16}$$

$$t_c = 1.421 \times 10^7 \frac{\sqrt{A_t}\, T_t^{3/2}}{Z^4\, n \ln \Lambda} \tag{3.1.17}$$

$$t_s = 6.765 \times 10^6 \frac{A_t^{3/2} \sqrt{T_t}\, T_f}{Z_t^2\, Z_f^2\, [\, A_t + A_f \,]\, n_f \ln \Lambda\, G\,(x)} \tag{3.1.18}$$

$$t_{eq} = 7.334 \times 10^6 \frac{A_t\, A_f}{Z_t^2\, Z_f^2\, n_f \ln \Lambda} \left[\frac{T_t}{m_t} + \frac{T_f}{m_f} \right]^{3/2} \tag{3.1.19}$$

Three kinds of self collision time, t_{p-p} (protons–protons), t_{e-e} (electrons–electrons), and t_{C-C} (carbon ions–carbon ions), are given according to equation (3.1.17) as

$$t_{p-p} = 1.421 \times 10^7 \frac{T_p^{3/2}}{n_p \ln \Lambda} \tag{3.1.20}$$

$$t_{e-e} = 3.305 \times 10^5 \frac{T_e^{3/2}}{n_e \ln \Lambda} \tag{3.1.21}$$

$$t_{C-C} = 4.922 \times 10^7 \frac{T_C^{3/2}}{Z_C^4\, n_C \ln \Lambda} \tag{3.1.22}$$

- Case 2: when $x \rightarrow 0$:

$$t_D = 1.014 \times 10^7 \frac{A_t\, T_t \sqrt{T_f}}{Z_t^2\, Z_f^2 \sqrt{A_f}\, n_f \ln \Lambda} \tag{3.1.23}$$

$$t_E = 5.071 \times 10^6 \frac{A_t\, T_t \sqrt{T_f}}{Z_t^2\, Z_f^2 \sqrt{A_f}\, n_f \ln \Lambda} \tag{3.1.24}$$

$$t_s = 1.469 \times 10^7 \frac{A_t\, T_f^{3/2}}{Z_t^2\, Z_f^2 \sqrt{A_f} \left[1 + \frac{A_f}{A_t} \right] n_f \ln \Lambda} \tag{3.1.25}$$

t_{eq}: *the same as that in case* 1 .

Now the relation between t_D and t_E in this special case is $t_E = \frac{1}{2} t_D$ since

$$\frac{t_D}{t_E} = \frac{4\,G(x)}{\Phi(x) - G(x)} = \frac{4\,\dfrac{G(x)}{x}}{\dfrac{1}{x}\left[\Phi(x) - G(x)\right]}$$

$$\rightarrow \frac{4\,\dfrac{2}{3\sqrt{\pi}}}{\dfrac{4}{3\sqrt{\pi}}} = \frac{4 \times 2}{4} = 2 \quad as\ x \rightarrow 0\,. \tag{3.1.26}$$

- Case 3: when $x \rightarrow \infty$:

$$t_D = 1.015 \times 10^7\ \frac{\sqrt{A_t}\ T_t^{3/2}}{Z_t^2\ Z_f^2\ n_f \ln \Lambda} \tag{3.1.27}$$

$$t_E = 7.610 \times 10^6\ \frac{T_t^{5/2}\ A_f}{Z_t^2\ Z_f^2\ T_f \sqrt{A_t}\ n_f \ln \Lambda} \tag{3.1.28}$$

$$t_s = 2.029 \times 10^7\ \frac{T_t^{3/2}\ \sqrt{A_t}}{Z_t^2\ Z_f^2 \left[1 + \dfrac{A_t}{A_f}\right] n_f \ln \Lambda} \tag{3.1.29}$$

t_{eq}: *the same as that in case* 1 .

The relation between t_D and t_E in this special case is

$$\frac{t_D}{t_E} = \frac{4\,G(x)}{\Phi(x) - G(x)} = \frac{4\,\dfrac{G(x)}{x}}{\dfrac{1}{x}\left[\Phi(x) - G(x)\right]}$$

$$\rightarrow \frac{4\,\dfrac{1}{2x^2}}{\dfrac{1}{x}} = \frac{4}{2x^3}\,x = \frac{2}{x^2} \quad as\ x \rightarrow \infty\,. \tag{3.1.30}$$

Table 2. The Collision Times of Carbon Ions with Plasma Protons and Electrons *

Type of Interaction times μsec	Test Particles = Carbon Ions (A_t=12) Field Particles = Electrons (A_f=5.4859×10^{-4}, Z_f=−1)				Test Particles = Carbon Ions (A_t=12) Field Particles = Protons (A_f=1, Z_f=+1)	
	Method A †		Method B ‡		Method A	
	C^+ (Z=+1)	C^{++} (Z=+2)	C^+ (Z=+1)	C^{++} (Z=+2)	C^+ (Z=+1)	C^{++} (Z=+2)
Deflection Time $t_D=\frac{W^2}{<(\Delta W_\perp)^2>}$	28.77 μsec	7.19 μsec	26.49 μsec	6.62 μsec	0.69 μsec	0.17 μsec
Energy Exchange Time $t_E=\frac{E^2}{<(\Delta E)^2>}$	14.11 μsec	3.53 μsec	13.25 μsec	3.31 μsec	0.36 μsec	0.09 μsec
Slowing-Down Time $t_s=-\frac{W}{<\Delta W_\parallel>}$	37.60 μsec	9.40 μsec	38.38 μsec	9.60 μsec	0.89 μsec	0.22 μsec
Equipartition Time $t_{eq}=\frac{T_f-T_t}{\frac{dT_t}{dt}}$	19.10 μsec	4.77 μsec	19.10 μsec	4.77 μsec	0.50 μsec	0.13 μsec

For the scattering time of carbon ions by plasma electrons we should use the formulae in case 2 to reduce the calculation error since x is very small, $x = \left[\frac{3}{2}\right]^{1/2} \left[\frac{m_e}{m_C}\right]^{1/2} \left[\frac{T_C}{T_e}\right]^{1/2} = 0.0083$ assuming $T_e = T_p \simeq T_{C^+} \simeq T_{C^{++}}$. When we calculate the relaxation time of carbon ions by plasma protons, $x = \left[\frac{3}{2}\right]^{1/2} \left[\frac{m_p}{m_C}\right]^{1/2} \left[\frac{T_C}{T_e}\right]^{1/2} = 0.354$ with the similar assumptions, we can use the formulae of either case 1 or case 2 since x is not very small. The numerical results for these calculations are plotted in Fig.3.2 and Fig.3.3. A special example is given in table 3.1 for the typical HBT

* This table is under the asumptions of $T_{c^+}=T_{c^{++}}=T_e=T_i=5eV$, $n_e=n_i=3\times10^{14}(cm^{-3})$.

† Method A is to directly calculate $\Phi(x)-G(x)$ and $G(x)$, for any x; even x is small.

‡ Method B is to take the limit of $\frac{1}{x}[\Phi(x)-G(x)]\rightarrow\frac{4}{3\sqrt{\pi}}$, $\frac{1}{x}G(x)\rightarrow\frac{2}{3\sqrt{\pi}}$, for small x.

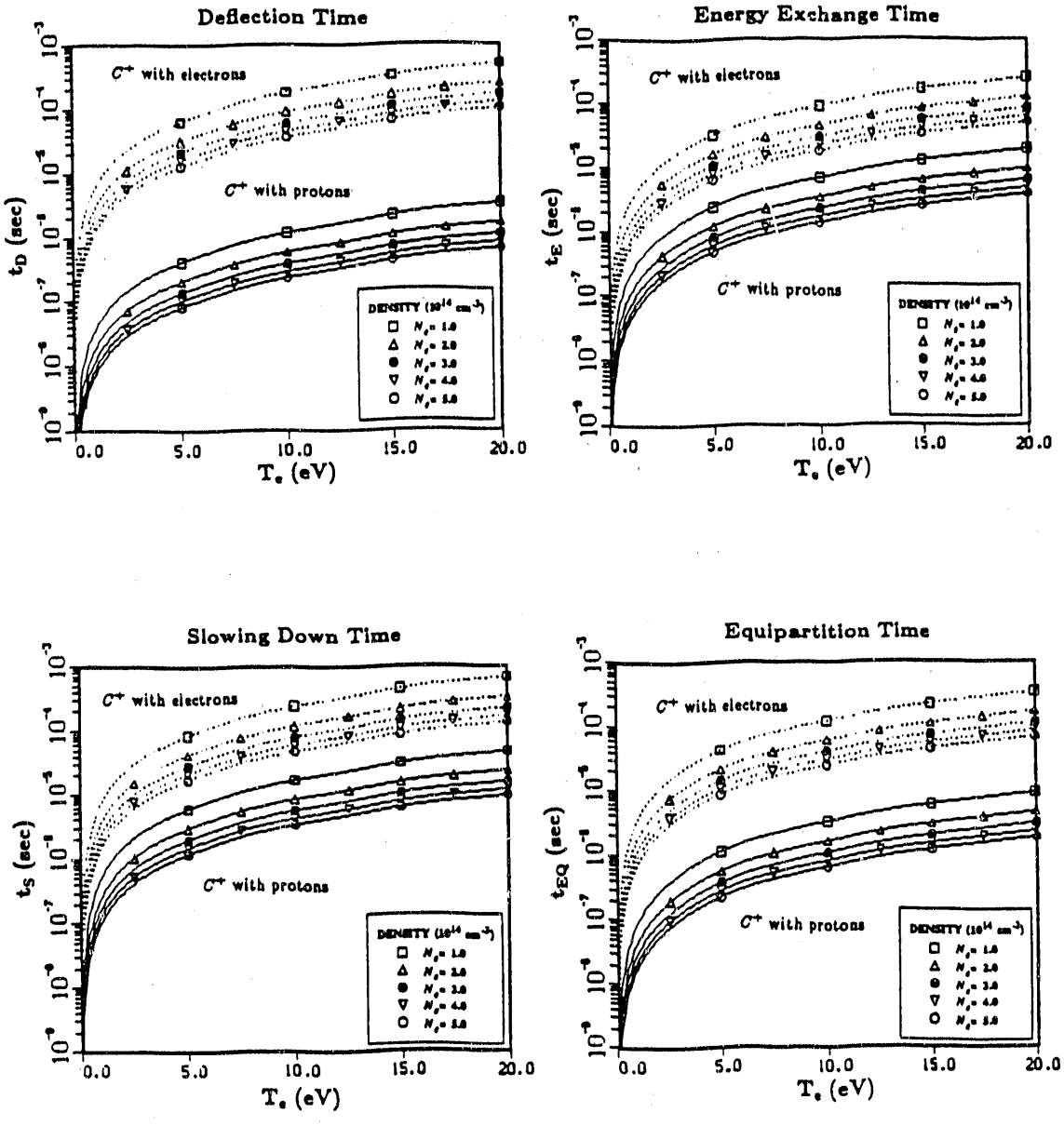

Figure 3.2 The different relaxation time of the $C^+(Z=1)$ ion with protons and electrons as a function of temperature.

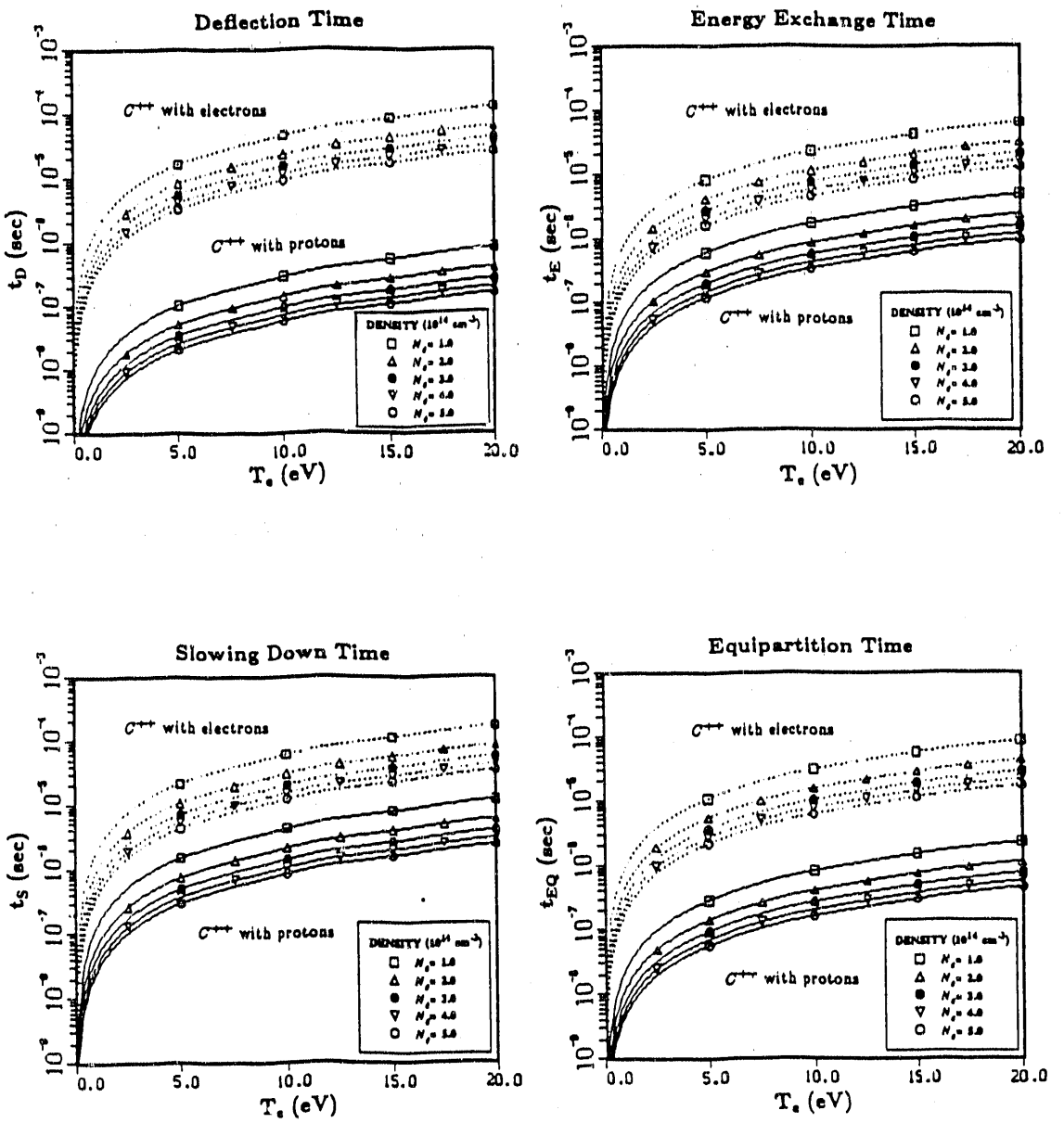

Figure 3.3 The different relaxation time of the C^{++}(Z=2) ion with protons and electrons as a function of temperature.

parameters at $n_e = 3.0 \times 10^{14}$ (cm^{-3}), $T_e \approx T_p \approx T_{C^+} \approx T_{C^{++}} \approx 5$ (eV). From these results we can see that relaxation time of carbon ions by electrons is about two orders longer than that by protons, due to the small electron mass, and these interactions provide less force for both the dragging and scattering on carbon ions. Therefore, the dominant collision process is the interaction between carbon ions and protons, not electrons.

Another point to be noted is that according to equation (3.1.22) the self collision time of carbon ions is much longer than that of electrons or protons since the carbon ion densities are about $10^2 - 10^3$ times lower than plasma density (see chapter 2). But this is not quite true for the higher ionization state because t_{C-C} drops as $\frac{1}{Z_C^4}$. In our experiment $Z = 1$ or 2 and $\ln \Lambda$ does not change much for carbon ions, so the diffusion of carbon ions is mainly driven by the carbon ion density gradient via the collisions with protons rather than by the self collisions of carbon ions themselves.

3.2 Basic Assumptions

Several assumptions have been made to interpret the time evolution of the spectral light emission from carbon ions.

It is assumed that the local magnetic flux tube can be approximated as a cylinder with the $\hat{z}$–axis along the magnetic field line which is in the toroidal direction since the carbon tip is located on the magnetic axis of plasma. This also means that the magnetic flux surfaces are just the cylindrical surfaces uniformly nested within each other and the magnetic field lines are straight and in the $\hat{z}$–direction. The cylindrical geometry is described by local Cartisian coordinates $\hat{x} - \hat{y} - \hat{z}$ since the diffusion could be anisotropic in our problem. These coordinates and the toroidal coordinates $\hat{R} - \hat{Z} - \hat{\Phi}$ are shown in Fig.3.4.

Three diffusion coefficients, D_x, D_y, and D_z, will be used to describe the diffusion process. In our analytical solutions of the continuity equations, the three coefficients

can be different from each other. However, in our problem, the diffusion is assumed to be axisymmetric about the local cylindrical $\hat{z}$–axis, i.e. $D_x = D_y = D_\perp$ and $D_z = D_{||}$, since the HBT plasma has a nearly circular cross section.

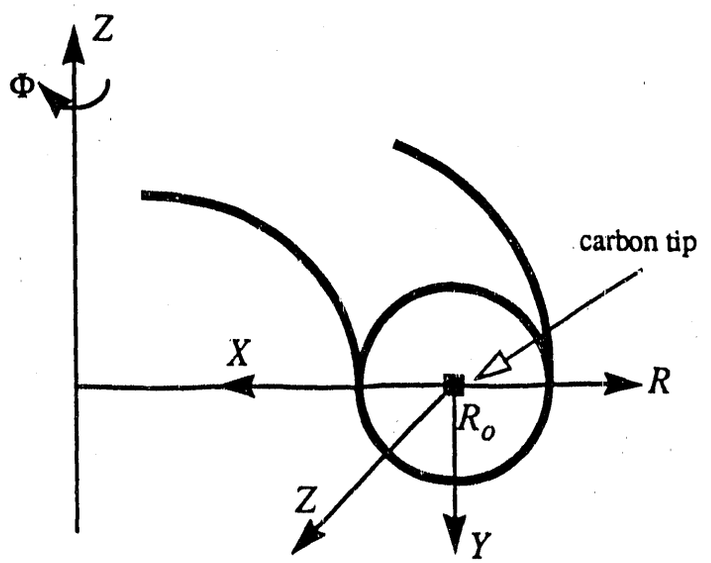

Figure 3.4 The coordinate system used in the diffusion model .

From the calculation of collision time, we know that the injected carbon ions can quickly (in about 1.0 (μsec)) set up a thermal equilibration with the background plasma ions and electrons. The thermal velocity of carbon ion is $V_{th,c} = \left[\frac{3T_c}{m_c} \right]^{1/2} \approx 1.1 \sim 1.5$ ($cm/\mu sec$) at $T_c \approx 4 \sim 10\,(eV)$, so the mean free path of carbon ions due to collisions with plasma protons is $\lambda_c = V_{th,c} \cdot t_D \leq 1.0\,(cm)$ for C^+ ions or $\leq 0.2\,(cm)$ for C^{++} ions. It is evident that it would take a longer time than the HBT operation time for carbon ions to fill the entire flux surface. Experimentally, it is observed that the carbon ions remain only in the vicinity of carbon tip so the diffusion is determined by the local magnetic field and the local plasma density and temperature. On this view point, it is reasonable to assume that all of the diffusion coefficients, the ionization rates and the recombination rates are constants in both the space and time domains.

3.3 Ionization and Recombination Time of Carbon Ions

Two methods have been used to estimate the rates of electron impact ionization and recombination processes: the time-dependent corona model and some experimental data.

The time-dependent corona model assumes[21] that (a)the characteristic time for the change of the plasma parameters is slow compared with both the atomic lifetime and the electron thermalization time (this is satisfied for the HBT plasma); (b)the ionization process is step by step, i.e. $Z \rightarrow Z+1 \rightarrow Z+2$,etc., and is caused by a collision of a free electron with an atom or ion in its ground level and the recombination is radiative; (c)a spectral line radiation is produced by an inelastic electron collision exciting an ion from its ground state and the subsequent decay of the excited level to the ground state. These assumptions are valid for once-ionized states when the electron density $n_e < 5 \times 10^{14}$ (cm^{-3}) at $T_e \sim 50$ (eV), and the validity varies as

$$n_e \leq k\,(Z+1)^6\, T_e^{1/2} \exp\left[\frac{(Z+1)^2}{T_e}\right], \tag{3.3.1}$$

where k is a constant and Z is the ion charge number. The HBT plasma barely satisfies this condition. The ionization rate can be expressed as:

$$S\,(T_e, \chi_Z, Z) \equiv (n_e\, \tau_{ion,Z})^{-1}$$

$$= \frac{1.1 \times 10^{-5}}{\chi_Z^{3/2}} \frac{\zeta_Z \left[\dfrac{k\,T_e}{\chi_Z}\right]^{1/2}}{6 + \left[\dfrac{k\,T_e}{\chi_Z}\right]} \exp\left[-\frac{\chi_Z}{k\,T_e}\right], \tag{3.3.2}$$

where χ_Z is the ionization potential at charge state Z in the unit of (eV), $k\,T_e$ is the electron temperature in (eV), and ζ_Z is the number of electrons in the outer shell of an ion at charge state Z.

The reciprocal of the ionization rate for carbon ions in the range of electron temperature 0.0 – 30.0 (eV) is plotted in Fig.3.5 for the ionization states $Z = 1, 2, 3, 4$ which correspond to the ionization potential $\chi_Z =$ 11.256, 24.376, 47.871, and 64.476 (eV), respectively. The time ratio for two successive stages of ionization of charge Z and $Z + 1$ is calculated as:

$$\frac{\tau_{ion,Z+1}}{\tau_{ion,Z}} = \frac{\chi_{Z+1}}{\chi_Z} \frac{\zeta_Z}{\zeta_{Z+1}} \frac{\left[6 + \frac{k\,T_e}{\chi_{Z+1}}\right]}{\left[6 + \frac{k\,T_e}{\chi_Z}\right]} \exp\left[-\frac{(\chi_Z - \chi_{Z+1})}{k\,T_e}\right], \qquad (3.3.3)$$

and plotted in Fig.3.6.

For the data on radiative recombination reviewed by Bates[22], the recombination coefficient depends mainly on the value of the ionic charge. The following formula for the recombination coefficient α may be relied up on to $\pm$ 100% (with the temperature range 1 (eV) < $\left[\frac{T_e}{Z^2}\right]$ < 13 (eV):

$$\alpha\,(T_e, Z+1, g) = 2.79 \times 10^{-11} \frac{Z^2}{\sqrt{T_e}} \quad (cm^3\,sec^{-1})\,. \qquad (3.3.4)$$

The reciprocal of the radiative recombination coefficient is plotted in Fig.3.7 for different ionization charge states in the range of electron temperature 0.0 – 30.0 (eV).

The experimental data of the rate of coefficient of the carbon ions is taken from Phaneu, etc.[23], and presented in Fig.3.8.

3.4 Impurity Transport Modeling

Consider the ith ionization state of impurity ions with number density $n_i(\vec{r}, t)$, shown in Fig.3.9. $n_i(\vec{r}, t)$ depends not only on the source of the ith state, but also on the ionization or recombination from the adjacent lower or higher ionization state[24]. So, in general, the continuity equation of the ith state impurity can be written as:

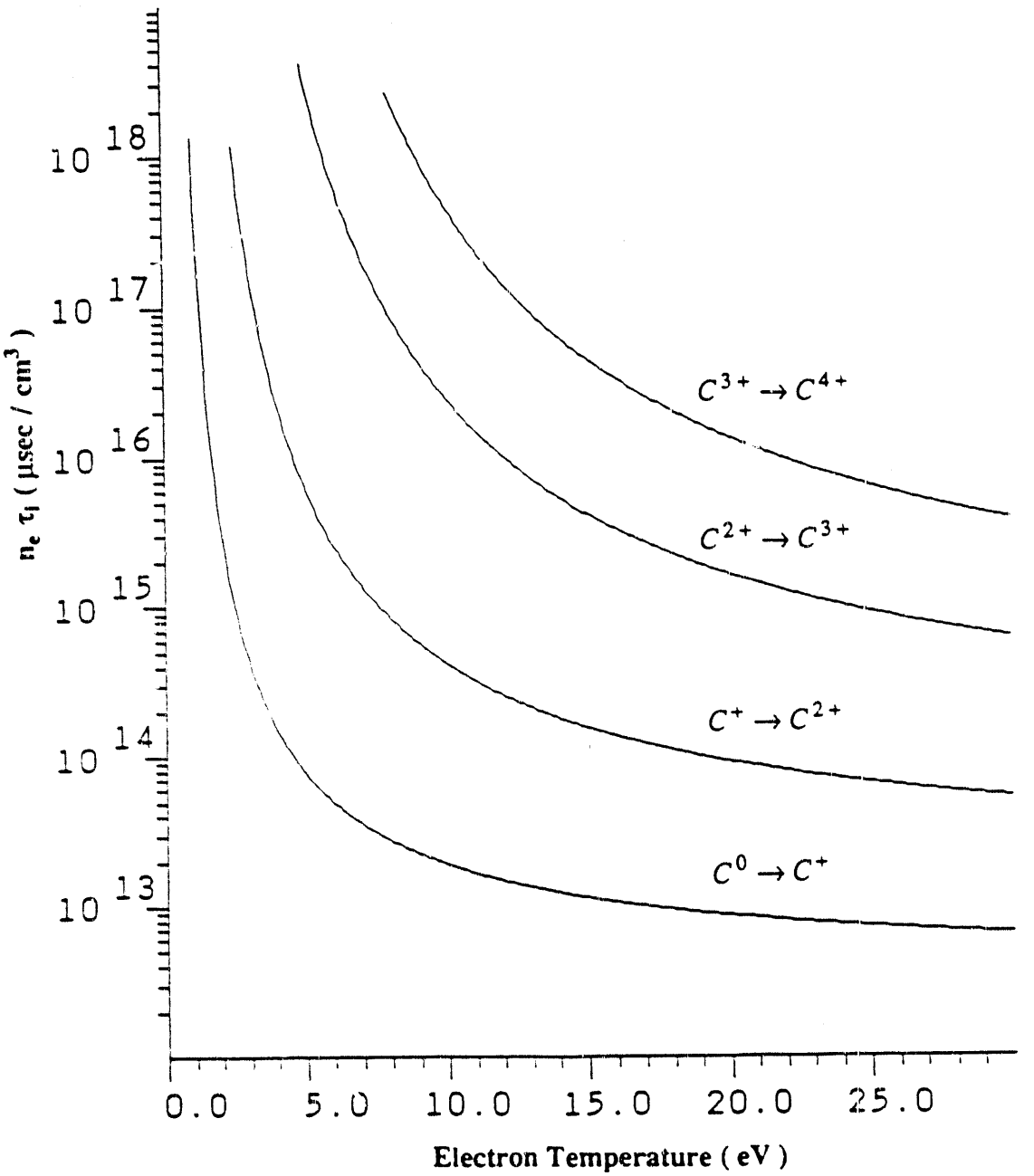

Figure 3.5 The reciprocal of the ionization rate of carbon ions at different ionization states .

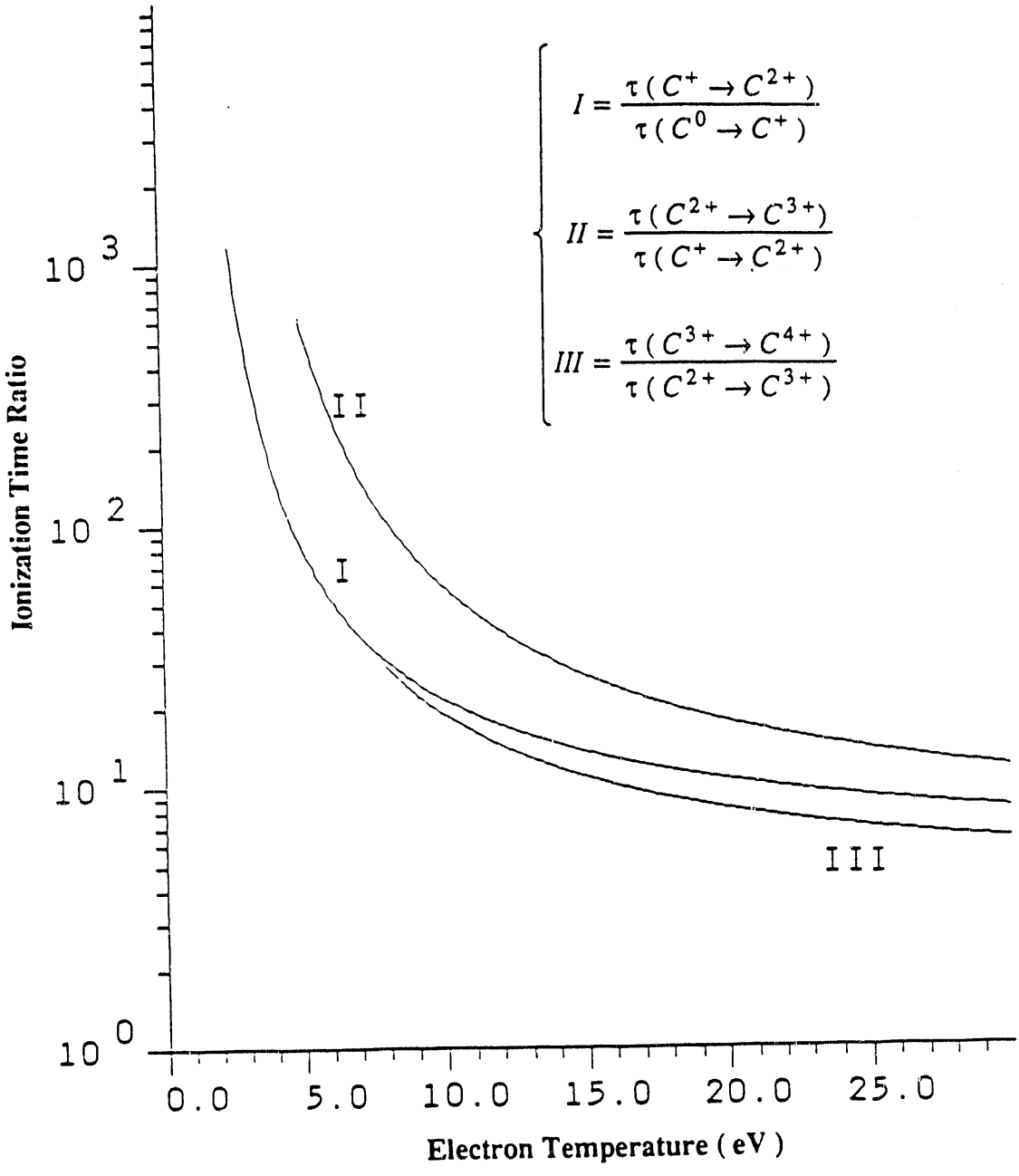

Figure 3.6 The time ratio for two successive stages of ionization of charge Z and $Z+1$.

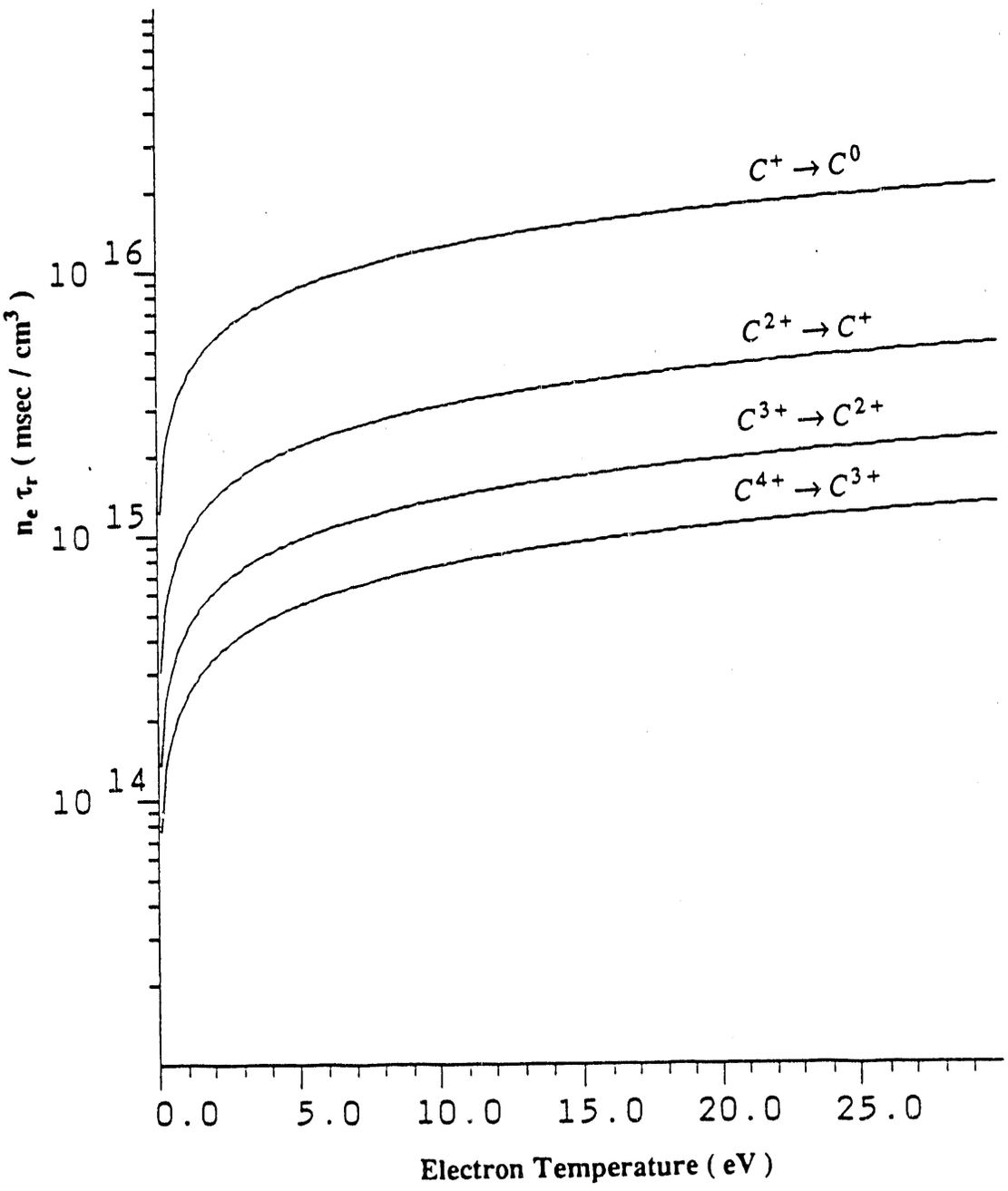

Figure 3.7 The reciprocal of the radiative recombination rate of carbon ions at different ionization states .

$$e^- + C^{q+} \rightarrow C^{(q+1)+} + 2e^-$$

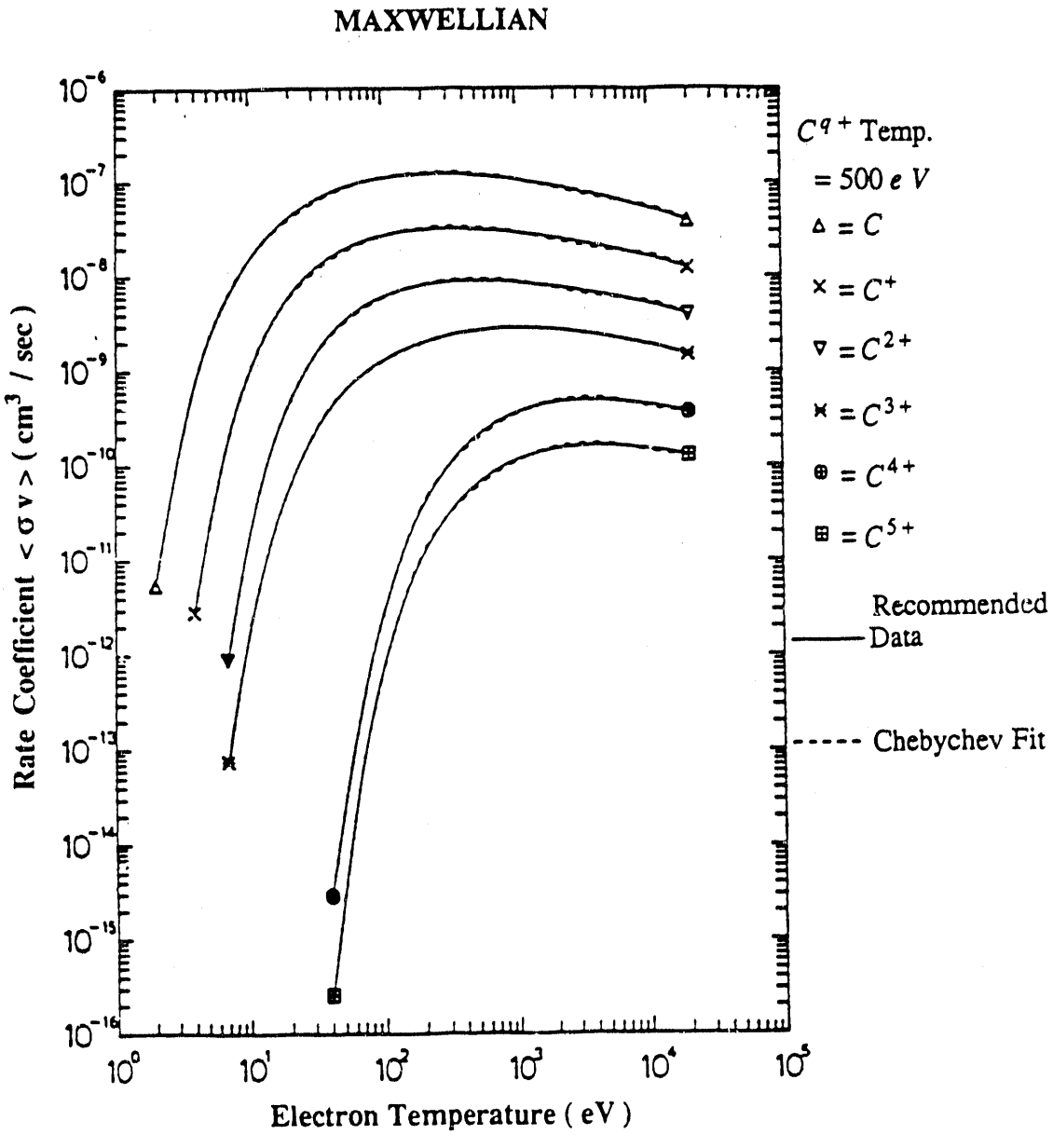

Figure 3.8 The experimental data for the rate coefficient of carbon ions at different ionization states.

$$\frac{\partial n_i}{\partial t} = \left[D_{ix}\frac{\partial^2}{\partial x^2} + D_{iy}\frac{\partial^2}{\partial y^2} + D_{iz}\frac{\partial^2}{\partial z^2} \right] n_i + (I_{i-1}n_{i-1} + R_{i+1}n_{i+1}) - (I_i n_i + R_i n_i) + S(\vec{r},t) \tag{3.4.1}$$

where $I_i\ (1/sec) = n_e < \sigma v >_{i \to i+1}$ is the ionization rate of impurity ions from the ith to the $(i+1)^{th}$ state, and $R_i\ (1/sec) = n_e < \sigma v >_{i+1 \to i}$ the recombination rate from the $(i+1)^{th}$ to the ith state.

Accordingly the characteristic time for ionization and recombination for the typical HBT parameters ($n_e \approx 1.0 - 3.0 \times 10^{14}\ (cm^{-3})$, $T_e \approx 4 - 10\ (eV)$) are shown in Fig.3.10(a). For the duration of the plasma (~ 150 (μ sec)) the effects of recombination can be neglected since it happens on a millisecond time scale. Also the ionization from C^0 to C^+ is almost instantaneous (~ 1 (μ sec)), but C^{++} could be thought as the highest ionization state because the ionization from C^{++} to C^{+++} or higher state takes much longer than the discharge time. Only the transition from C^+ to C^{++} needs to be considered since it just falls into the experimental time range. Thus the problem of carbon ion transport can be simplified, as shown in Fig.3.10(b), and the continuity equations for C^+ and C^{++} ions become

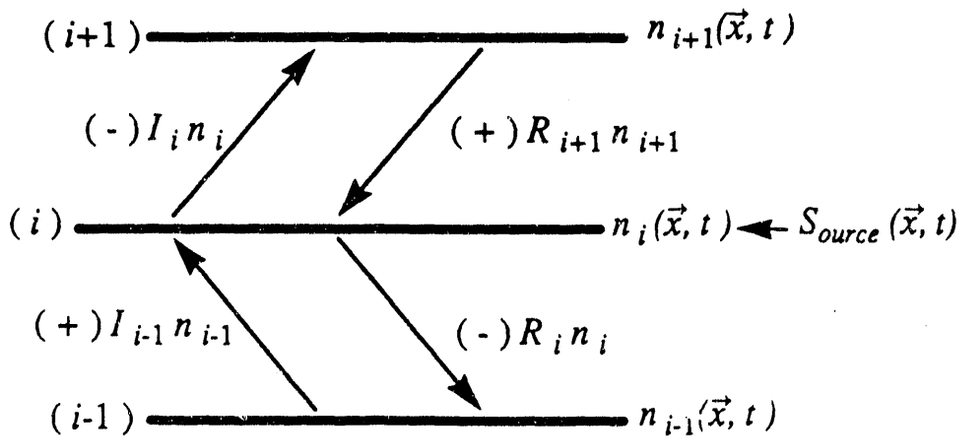

Figure 3.9 The relationship of ionization and recombination between the ith and the other two adjacent ionization states.

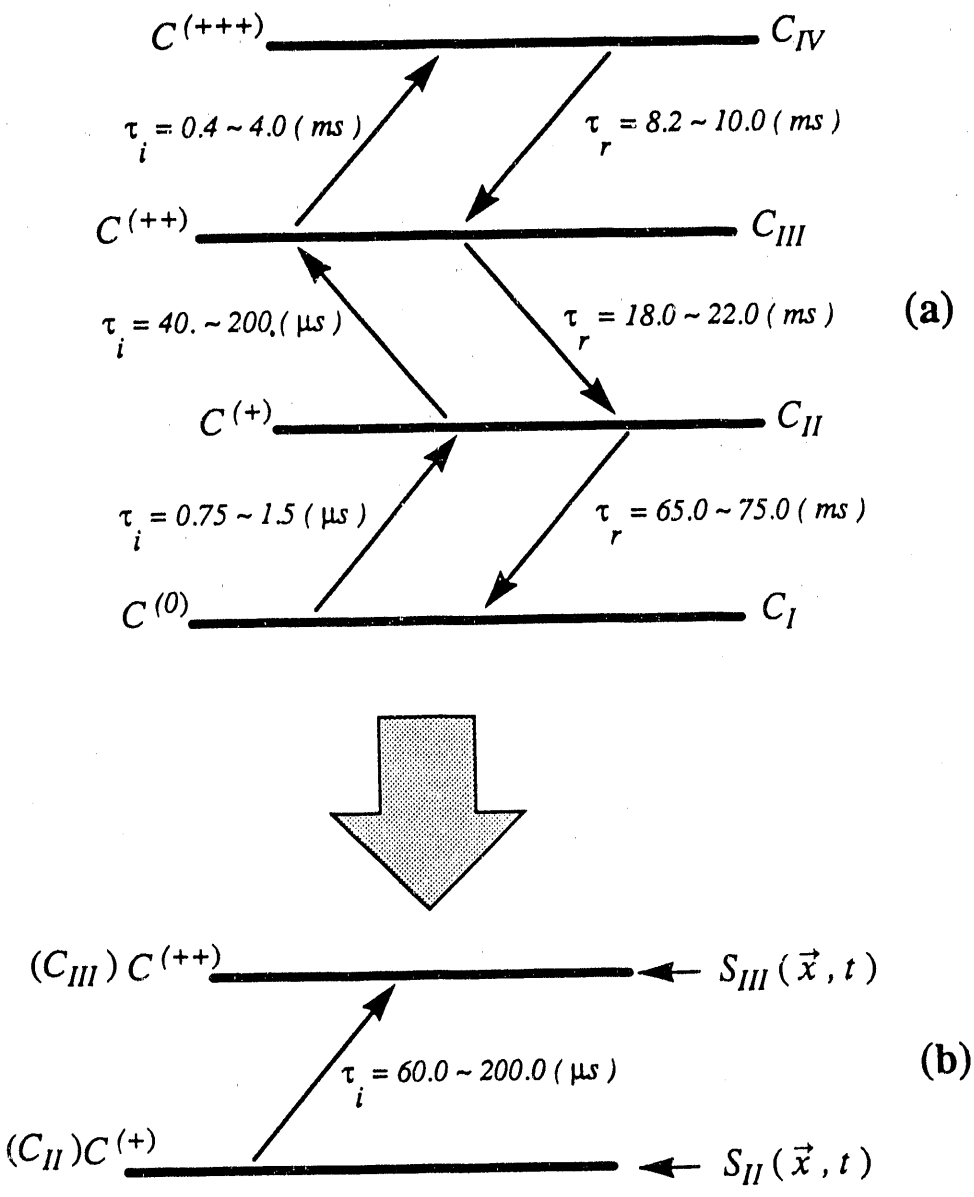

Figure 3.10 (a) The estimate of the ionization and recombination times for different ionization states of carbon ions at $n_e = 3 \times 10^{14}$ $(cm^{-3})$and $T_e = 4 \sim 10\ (eV)$; (b) The reduced model for the calculation of C^{+} and C^{++} ion densities in the time scale interest.

$$\frac{\partial n_{II}}{\partial t} = \left[D_{2x}\frac{\partial^2}{\partial x^2} + D_{2y}\frac{\partial^2}{\partial y^2} + D_{2z}\frac{\partial^2}{\partial z^2} \right] n_{II} - I\, n_{II} + S_{II} \tag{3.4.2}$$

$$\frac{\partial n_{III}}{\partial t} = \left[D_{3x}\frac{\partial^2}{\partial x^2} + D_{3y}\frac{\partial^2}{\partial y^2} + D_{3z}\frac{\partial^2}{\partial z^2} \right] n_{III} + I\, n_{II} + S_{III}\,, \tag{3.4.3}$$

where the subscripts II and 2 denote the C^+ ions (C_{II} emission), III and 3 for C^{++} ions (C_{III} emission), and I is the ionization rate ($1/sec$) from C^+ to C^{++}. S_{II} and S_{III} are the source terms for C^+ and C^{++} ions, respectively, which are formed during the discharge process of the carbon probe.

3.5 Three Models of the Discharge Source

Equations (3.4.2) and (3.4.3) can be reduced to the following general mathematical problem

$$\begin{cases} \dfrac{\partial n}{\partial t} = \left[D_x\dfrac{\partial^2}{\partial x^2} + D_y\dfrac{\partial^2}{\partial y^2} + D_z\dfrac{\partial^2}{\partial z^2} \right] n - A\, n + S(t\,;x,y,z) \\ n(t=0\,;x,y,z) = \phi\,(x,y,z) \\ (0 \le t < \infty\,; -\infty < x,y,z < +\infty) \end{cases} \tag{3.5.1}$$

where A is a constant. This is a 3-D diffusion problem in an infinite inhomogeneous medium, and the general solution is[25]:

$$n(t\,;x,y,z) = n_a(t\,;x,y,z) + n_b(t\,;x,y,z) \tag{3.5.2}$$

where

$$n_a(t\,;x,y,z) = \iiint_{-\infty}^{+\infty} \phi(\xi,\eta,\zeta) \times G(t\,;x-\xi,\, y-\eta,\, z-\zeta)\, d\xi\, d\eta\, d\zeta \tag{3.5.3}$$

and

$$n_b(t;x,y,z)=\int_0^t d\tau \iiint_{-\infty}^{+\infty} S(\tau;\xi,\eta,\zeta)\times$$

$$G(t-\tau;x-\xi,y-\eta,z-\zeta)\,d\xi\,d\eta\,d\zeta \qquad (3.5.4)$$

Here $G(t;x,y,z)$ is the "Green's function" of problem (3.4.1), i.e. the solution of the same diffusion problem but with unit strength point source $\delta(\vec{r})\,\delta(t)$

$$\begin{cases} \dfrac{\partial G}{\partial t}=\left[D_x\dfrac{\partial^2}{\partial x^2}+D_y\dfrac{\partial^2}{\partial y^2}+D_z\dfrac{\partial^2}{\partial z^2}\right] n\,G-AG \\ G(t=0;x,y,z)=\delta(x)\,\delta(y)\,\delta(z) \\ (0\le t<\infty;-\infty<x,y,z<+\infty) \end{cases} \qquad (3.5.5)$$

Using the Fourier transform, the Green's function can be obtained as follows

$$G(t;x,y,z)=\frac{1}{8\pi^{3/2}}\frac{e^{-At}}{\sqrt{D_xt}\sqrt{D_yt}\sqrt{D_zt}}\times$$

$$\exp\left[-\frac{x^2}{4D_xt}-\frac{y^2}{4D_yt}-\frac{z^2}{4D_zt}\right]. \qquad (3.5.6)$$

So the problem (3.4.1) is solved in principle and the remaining work is how to decide the initial condition $\phi(x,y,z)$ and the inhomogeneous parts, A and $S(t;x,y,z)$. Three models have been developed to describe the discharge process of carbon probe, as shown in Fig.3.11.

The ringing of the discharge current causes a puff of carbon ions (both C^+ and C^{++} ions as discussed in chapter 2) to be released at each pulse. The mathematical solution for this kind of source is obtained by linearly superimposing the three individual solutions (each one corresponding to one peak of the discharge current) according to the

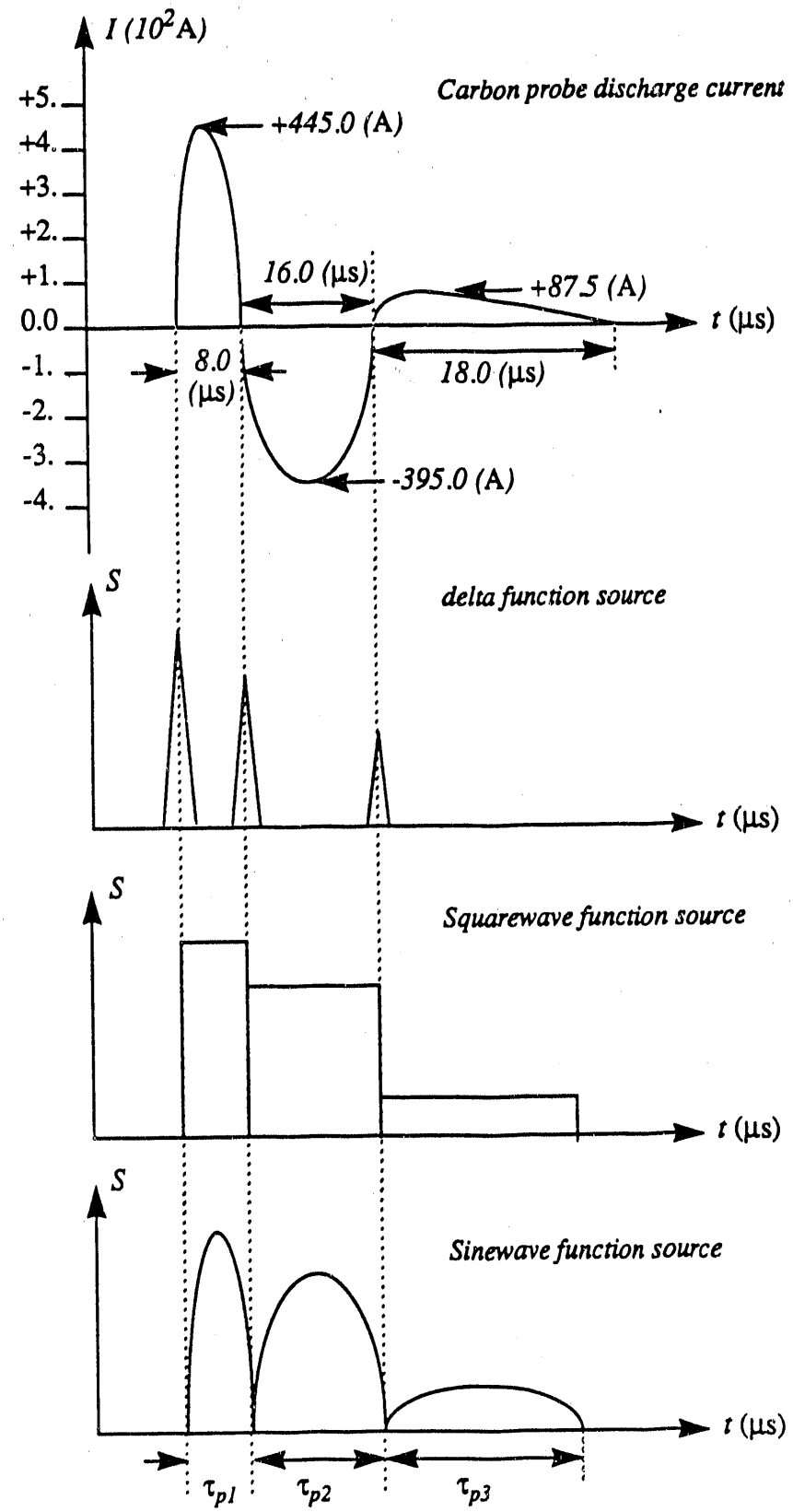

Figure 3.11 The carbon probe discharge current and the three mathematical models for the source of carbon ions.

time sequence, shown in Fig.3.11, because the problem is linear in all the unknown functions and their derivatives. Then the final solution can be generally expressed as the summation of three parts[26]:

$$n_{II}(t\,;x,y,z) = n_{II,1}(t\,;x,y,z) + n_{II,2}(t-\tau_{p1}\,;x,y,z)$$

$$+\, n_{II,3}(t-\tau_{p1}-\tau_{p2}\,;x,y,z) \tag{3.5.7}$$

Similarly,

$$n_{III}(t\,;x,y,z) = n_{III,1}(t\,;x,y,z) + n_{III,2}(t-\tau_{p1}\,;x,y,z)$$

$$+\, n_{III,3}(t-\tau_{p1}-\tau_{p2}\,;x,y,z) \tag{3.5.8}$$

where $n_{II,j}$ and $n_{III,j}(j=1,2,3)$ are zero when their time arguments are less than zero. $\tau_{pj}(j=1,2)$ is the pulse duration for each peak. It should be pointed out that the solution for each pulse has the same analytical form except for the difference in the relative level and the pulse length.

3.5.1 Delta Function Source Model

In this model the three pulses of the discharge current are simplified as three delta functions at the starting time of each pulse, see Fig 3.11. Then equation (3.4.2) becomes

$$\begin{cases} \dfrac{\partial n_{II}}{\partial t} = \left[D_{2x}\dfrac{\partial^2}{\partial x^2} + D_{2y}\dfrac{\partial^2}{\partial y^2} + D_{2z}\dfrac{\partial^2}{\partial z^2} \right] n_{II} - I n_{II} \\ n_{II}(t=0\,;x,y,z) = N_{II0}\,\delta(x)\,\delta(y)\,\delta(z) \\ (0 \le t < \infty\,; -\infty < x,y,z < +\infty) \end{cases} \tag{3.5.9}$$

Comparing with equation (3.5.1) we find that now $A = I$, $S = 0$ and $\phi = N_{II0}\,\delta(x)\,\delta(y)\,\delta(z)$. Since $\delta(x)$ has the dimension of $\frac{1}{x}$, N_{II0} is dimensionless and

denotes the total number of C^+ ions released in one pulse.

Similarly, for C^{++} ions, equation (3.4.3) can be written as

$$\begin{cases} \dfrac{\partial n_{III}}{\partial t} = \left[D_{3x}\dfrac{\partial^2}{\partial x^2} + D_{3y}\dfrac{\partial^2}{\partial y^2} + D_{3z}\dfrac{\partial^2}{\partial z^2} \right] n_{III} + I n_{II} \\ n_{III}(t=0\,;x,y,z) = N_{III0}\,\delta(x)\,\delta(y)\,\delta(z) \\ (0 \le t < \infty\,; -\infty < x,y,z < +\infty)\,. \end{cases} \tag{3.5.10}$$

N_{III0} is the total number of C^{++} ions coming from one pulse, and now $A = 0$, $S = I\,n_{II}$ and $\phi = N_{III0}\,\delta(x)\,\delta(y)\,\delta(z)$.

The solution of (3.5.9) is

$$n_{II}(t\,;x,y,z) = \frac{N_{II0}}{8\pi^{3/2}} \frac{e^{-At}}{\sqrt{D_{2x}t}\sqrt{D_{2y}t}\sqrt{D_{2z}t}} \times$$

$$\exp\left[-\frac{x^2}{4D_{2x}t} - \frac{y^2}{4D_{2y}t} - \frac{z^2}{4D_{2z}t} \right]. \tag{3.5.11}$$

But the solution of problem (3.5.10) includes two parts:

$$n_{III}(t\,;x,y,z) = n_{IIIa} + n_{IIIb} \tag{3.5.12}$$

where n_{IIIa} is the C^{++} ion density coming from the initial discharge of the carbon probe

$$n_{IIIa}(t\,;x,y,z) = \frac{N_{III0}}{8\,\pi^{3/2}} \frac{1}{\sqrt{D_{3x}t}\sqrt{D_{3y}t}\sqrt{D_{3z}t}} \times$$

$$\exp\left[-\frac{x^2}{4D_{3x}t} - \frac{y^2}{4D_{3y}t} - \frac{z^2}{4D_{3z}t} \right], \tag{3.5.13}$$

and n_{IIIb} is the C^{++} ion density resulting from the ionization of C^+ ions by the collisions with plasma electrons

$$n_{IIIb}(t\,;x,y,z) = \frac{N_{II0}}{8\,\pi^{3/2}} \int_0^t e^{-I\tau} f(\tau\,,\,t-\tau\,;x,y,z)\,d\tau \tag{3.5.14}$$

where the function $f(\tau\,;t-\tau\,;x,y,y)$ is defined as

$$f(\tau\,,\,t-\tau;x,y,z) = \frac{\exp\left\{-\dfrac{x^2}{4[D_{2x}\tau + D_{3x}(t-\tau)]}\right\}}{[D_{2x}\tau + D_{3x}(t-\tau)]^{1/2}} \times$$

$$\frac{\exp\left\{-\dfrac{y^2}{4[D_{2y}\tau + D_{3y}(t-\tau)]} - \dfrac{z^2}{4[D_{2z}\tau + D_{3z}(t-\tau)]}\right\}}{[D_{2y}\tau + D_{3y}(t-\tau)]^{1/2}[D_{2z}\tau + D_{3z}(t-\tau)]^{1/2}} \tag{3.5.15}$$

Note that x,y,z and t are four independent variables. When fitting the data at different radial positions we can adjust the coordinates to set $y = z = 0$ and the solutions will be greatly simplified.

Only in the delta function source model can an analytical solution of $n_{II}(t\,;x,y,z)$ be found and used to calculate $n_{III}(t\,;x,y,z)$, which partially comes from the initial condition and partially comes from the reionization of C^+ ions (i.e. n_{II} density). The following two models merely discuss the calculation of n_{II} because n_{III} is too complicated to be expressed analytically.

3.5.2 Square-wave Function Source Model

In this model, the effect of the finite dimension of the carbon tip is included and the pulse is considered as a square wave, as shown in Fig.3.12(a). The carbon tip is modeled as a rectangular parallelepiped with 3 dimensions $X_0 = Y_0 = 0.5\ cm$, and $Z_0 = 0.6\ cm$. The continuity equation of C^+ ions is

$$\begin{cases} \dfrac{\partial n_{II}}{\partial t} = \left[D_{2x}\dfrac{\partial^2}{\partial x^2} + D_{2y}\dfrac{\partial^2}{\partial y^2} + D_{2z}\dfrac{\partial^2}{\partial z^2} \right] n_{II} - I\, n_{II} + S(t\,;x,y,z) \\ n_{II}(t=0\,;x,y,z) = \begin{cases} N_{II0}\ (\,|x| \le X_0,\ |y| \le Y_0,\ |z| \le Z_0\,) \\ 0 \qquad (elsewhere) \end{cases} \\ S(t\,;x,y,z) = \begin{cases} \dfrac{N_{II0}}{\tau_p}\ (0 \le t \le \tau_p,\ |x| \le X_0,\ |y| \le Y_0,\ |z| \le Z_0\,) \\ 0 \qquad (t > \tau_p,\ -\infty < x,y,z < +\infty)\,. \end{cases} \end{cases} \tag{3.5.16}$$

Note here $A = -I$, $S \neq 0$. The solution of this problem also includes two parts:

$$n_{II} = n_{IIa}(t\,;x,y,z) + n_{IIb}(t\,;x,y,z) \tag{3.5.17}$$

where

$$n_{IIa}(t\,;x,y,z) = \frac{N_{II0}}{8} f(t\,;x,y,z) \tag{3.5.18}$$

$$(0 \le t < \infty\,; -\infty < x,y,z < +\infty)$$

and

$$n_{IIb}(t\,;x,y,z) = \frac{1}{8\,\pi^{3/2}} \left[\frac{N_{II0}}{\tau_p} \right] \begin{cases} \displaystyle\int_0^t f(t-\tau\,;x,y,z)\,d\tau \\ (0 \le t \le \tau_p\,; -\infty < x,y,z < +\infty) \\ \displaystyle\int_0^{\tau_p} f(t-\tau\,;x,y,z)\,d\tau \\ (\tau_p \le t \le \infty\,; -\infty < x,y,z < +\infty) \end{cases} \tag{3.5.19}$$

where the function $f\,(t-\tau\,;x,y,z)$ is defined as follows

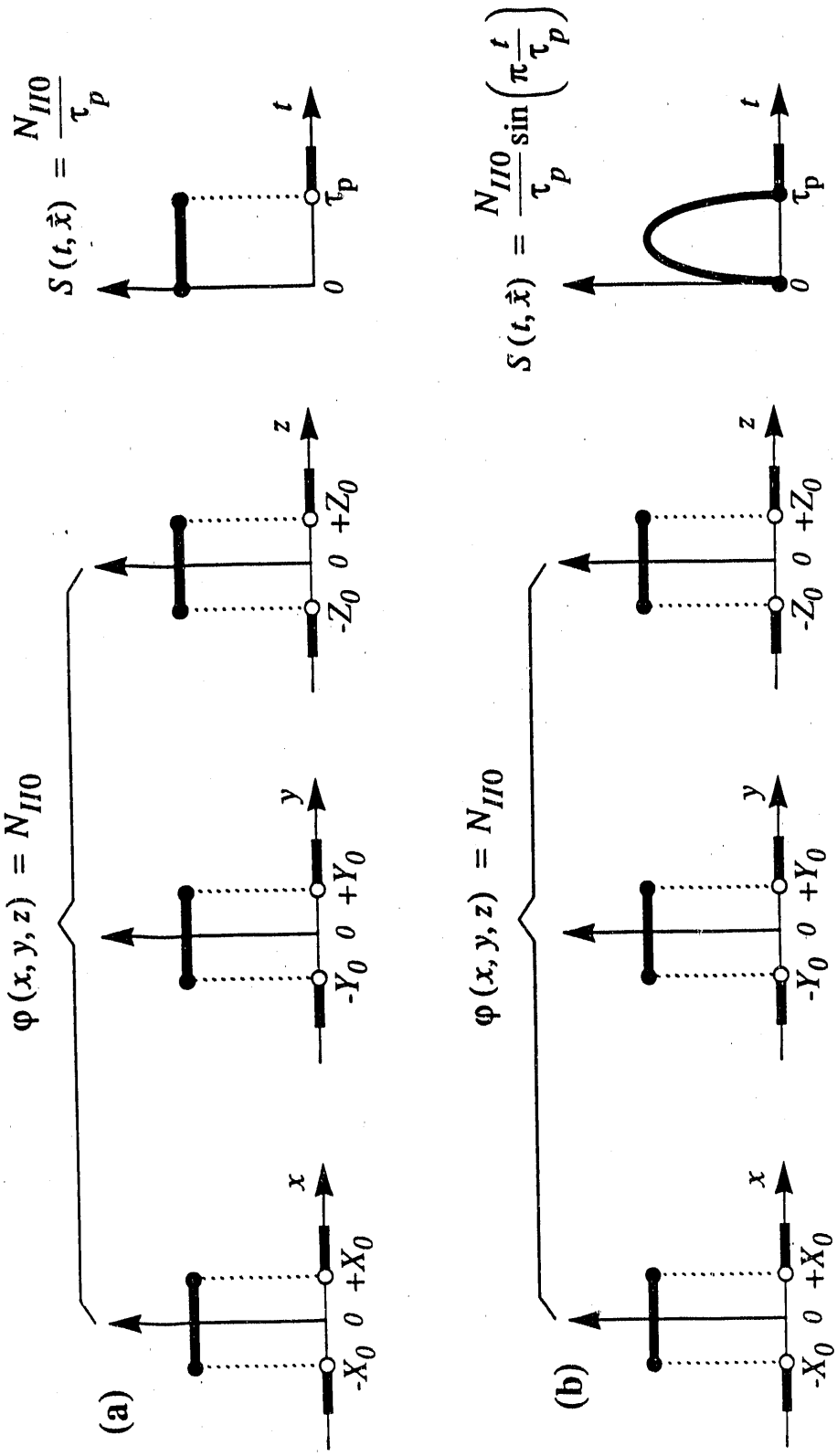

Figure 3.12 The illustration of the initial condition and the source term for (a)the square-wave function model, and (b)the sine-wave function model .

$$f(t-\tau;x,y,z)=e^{-I(t-\tau)}\times$$

$$\left[\Phi\left[\frac{x+X_0}{2\sqrt{D_{2x}(t-\tau)}}\right]-\Phi\left[\frac{x-X_0}{2\sqrt{D_{2x}(t-\tau)}}\right]\right]\times$$

$$\left[\Phi\left[\frac{y+Y_0}{2\sqrt{D_{2y}(t-\tau)}}\right]-\Phi\left[\frac{y-Y_0}{2\sqrt{D_{2y}(t-\tau)}}\right]\right]\times$$

$$\left[\Phi\left[\frac{z+Z_0}{2\sqrt{D_{2z}(t-\tau)}}\right]-\Phi\left[\frac{z-Z_0}{2\sqrt{D_{2z}(t-\tau)}}\right]\right], \qquad (3.5.20)$$

where Φ is the "error function" as mentioned before having the following simple feature

$$\begin{cases}\Phi(0)=0, & \Phi(\infty)=1\\ \Phi(-x)=-\Phi(x), & \Phi(-\infty)=-1\end{cases} \qquad (3.5.21)$$

If $|x|<X_0, |y|<Y_0, |z|<Z_0$, $f\rightarrow\ [1-(-1)]^3=8$, then $n_{IIa}\rightarrow\ \frac{N_{II0}}{8}\times 2\times 2\times 2=N_{II0}$ and $n_{IIb}\rightarrow 0$ when $t\rightarrow 0$. This is just the "source region" as defined in the initial condition. In the non-source region, i.e. $|x|>X_0$, $|y|>Y_0$, $|z|>Z_0$, $f\rightarrow(1-1)^3=0$, so $n_{IIa}\rightarrow\frac{N_{II0}}{8}$ and $n_{IIb}\rightarrow 0$ when $t\rightarrow 0$. This means that the initial ions are only localized at the source region. At the boundary of the carbon tip, i.e. $|x|=X_0$, $|y|=Y_0$, $|z|=Z_0$, $f\rightarrow(1-0)^3=1$, $n_{IIa}\rightarrow\frac{N_{II0}}{8}\times 1^3=\frac{N_{II0}}{8}$ and $n_{IIb}\rightarrow 0$ when $t\rightarrow 0$, which indicates that each quadrant only emits one eighth of N_{II0}; the total number of ions is released from eight quadrants in each pulse because the cube is symmetric about the origin of coordinates.

3.5.3 Sine-wave Function Source Model

In the square-wave function model, the source is assumed to emit carbon ions continuously during each pulse of the discharge. But, in fact, the discharge current is eventually starting from zero, reaching the peak value and then dropping to zero again, and so the sine-wave function model is used to describe this feature. This model has the same spatial description of the source as the square-wave one, but with the pulse shape modification, shown in Fig.3.12(b). Now the diffusion problem can be expressed as follows:

$$\begin{cases} \dfrac{\partial n_{II}}{\partial t} = \left[D_{2x}\dfrac{\partial^2}{\partial x^2} + D_{2y}\dfrac{\partial^2}{\partial y^2} + D_{2z}\dfrac{\partial^2}{\partial z^2} \right] n_{II} - I\, n_{II} + S(t\,;x,y,z) \\ n_{II}(t=0\,;x,y,z) = 0\ (-\infty < x,y,z < +\infty) \\ S(t\,;x,y,z) = \begin{cases} \dfrac{N_{II0}}{\tau_p}\sin\left[\pi\dfrac{t}{\tau_p}\right] & (0 \le t \le \tau_p,\ |x| \le X_0,\ |y| \le Y_0,\ |z| \le Z_0) \\ 0 & (elsewhere)\,. \end{cases} \end{cases} \tag{3.5.22}$$

Note now we have $A = -I$, $S \neq 0$, but $\phi = 0$, so $n_{IIa} = 0$, and $n_{II} = n_{IIb}$, i.e.

$$n_{II}(t\,;x,y,z) = \frac{1}{8\pi^{3/2}}\left[\frac{N_{II0}}{\tau_p}\right] \begin{cases} \displaystyle\int_0^t f(\tau, t-\tau\,;x,y,z)\,d\tau \\ (0 \le t \le \tau_p\,; -\infty < x,y,z < +\infty) \\ \displaystyle\int_0^{\tau_p} f(\tau, t-\tau\,;x,y,z)\,d\tau \\ (\tau_p \le t \le \infty\,; -\infty < x,y,z < +\infty) \end{cases} \tag{3.5.23}$$

where the function $f(\tau, t-\tau\,;x,y,z)$ is defined as

$$f(\tau, t-\tau; x,y,z) = \sin\left[\pi \frac{\tau}{\tau_p}\right] e^{-I(t-\tau)} \times$$

$$\left[\Phi\left[\frac{x+X_0}{2\sqrt{D_{2x}(t-\tau)}}\right] - \Phi\left[\frac{x-X_0}{2\sqrt{D_{2x}(t-\tau)}}\right]\right] \times$$

$$\left[\Phi\left[\frac{y+Y_0}{2\sqrt{D_{2y}(t-\tau)}}\right] - \Phi\left[\frac{y-Y_0}{2\sqrt{D_{2y}(t-\tau)}}\right]\right] \times$$

$$\left[\Phi\left[\frac{z+Z_0}{2\sqrt{D_{2z}(t-\tau)}}\right] - \Phi\left[\frac{z-Z_0}{2\sqrt{D_{2z}(t-\tau)}}\right]\right]. \qquad (3.5.24)$$

Obviously this solution also satisfies the initial condition of problem (3.5.21).

3.5.4 Comparison of the Three Models

Three models have been plotted in Fig.3.13 at three different radial positions, i.e. $y = z = 0.0\ (cm)$, $x = 1.5, 2.5, 4.7\ (cm)$, with the parameters $D_{2x} = D_{2y} = D_{2\perp} = 9.7\ (m^2/sec)$ and $D_{2z} = D_{2\|} = 14.1\ (m^2/sec)$. When the viewing point is closer to the source region the differences among these models can be seen clearly. The delta function source has the sharpest evolution profile since it releases the least amount of carbon ions. The sine-wave model has the slowest time response of the discharge since it assumes the source is zero at $t = 0$ but the other two models provide the source with finite values, $N_{\|0}$, at $t = 0$. As the view point moves farther away from the source point the details from the discharge, either the differences between the three models or the multipeaks of the source current profile, are smoothed out as long as the diffusion coefficients are not too large.

It should be pointed out that from any one of the three models, as long as $t \neq 0$, then $n_{\|}(t; x,y,z)$ is non zero for any observation point no matter how far away from the source region, i.e. the diffusion velocity is infinity. The reason for this puzzle is that when we derive the diffusion equation (or say the continuity equation) the factor of the

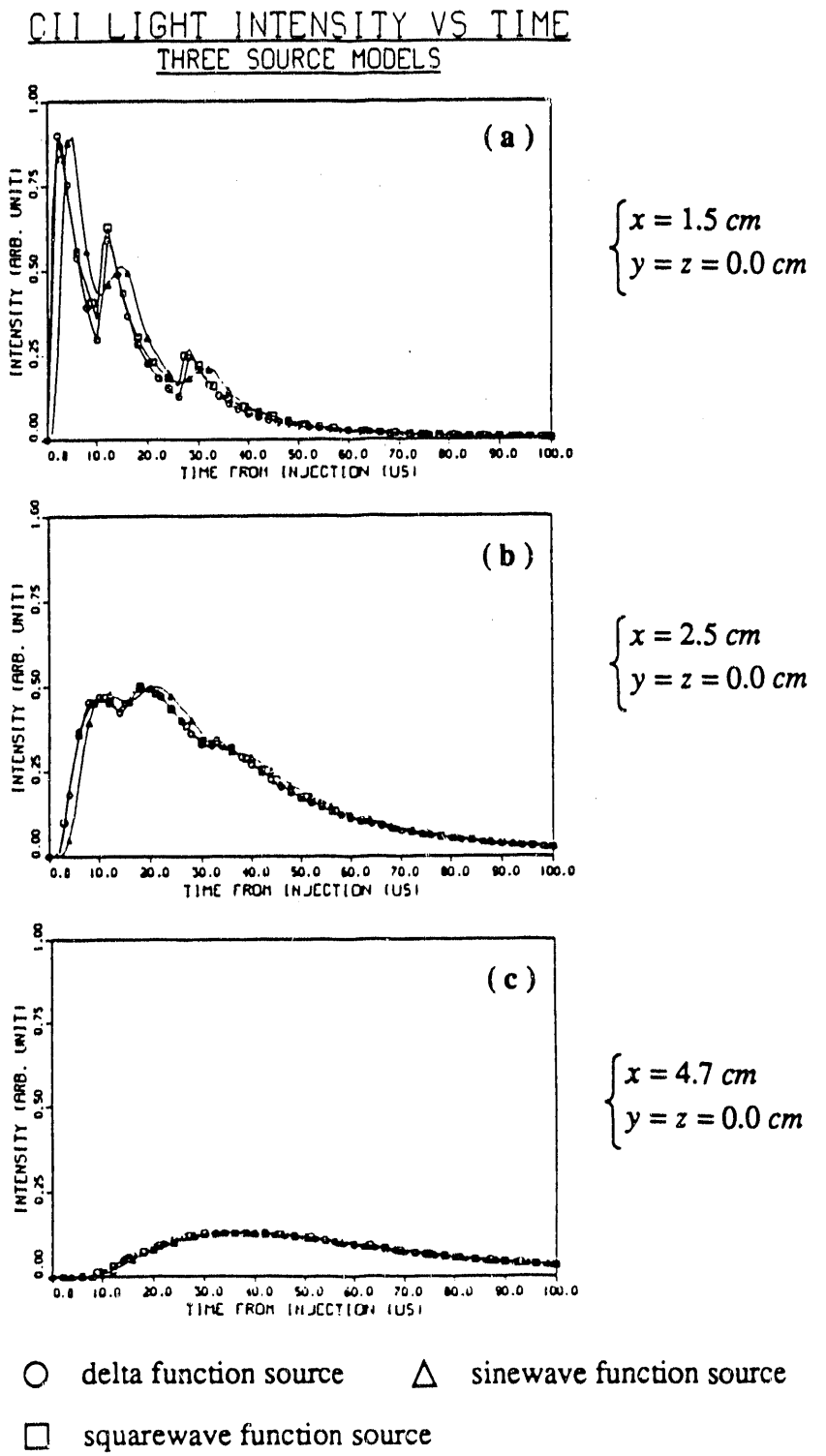

Figure 3.13 The comparison of the predicted curves of C_{II} ion density from the three mathematical models .

perturbation velocity is not included. This is equivalent to assuming that the perturbation signal can propagate infinitely fast.

Since the carbon diffusion is a 3-D problem, the Cartesian coordinates $\hat{x} - \hat{y} - \hat{z}$ are used which results in the error functions in the final solutions. If the problem is axisymmetric about, say, the $\hat{z}$–axis, a cylindrical coordinate $\hat{r} - \hat{\theta} - \hat{z}$ is usually adopted which will result in some other special functions, such as Bessel functions.

Finally it is necessary to discuss the numerical method to calculate the error functions since they are frequently used in our problem and determine the accuracy of the numerical fittings. The following formula[27], based on Chebyshev fitting, gives an approximate expression of the "complementary error" $erfc\ (x)$, which is defined as

$$erfc\ (x) = 1 - erf\ (x) = \frac{2}{\sqrt{\pi}} \int_x^{\infty} e^{-t^2}\, dt\ , \tag{3.5.25}$$

with fractional error everywhere less than 1.2×10^{-7}, i.e.

$$erfc\ (x) = u \exp\left[-z^2 + \sum_{i=0}^{i=9} a_i\, u^i \right] + \varepsilon\,(x) \tag{3.5.26}$$

$$|\varepsilon\,(x)| < 1.2 \times 10^{-7} \qquad (\text{ for } any\ x\ )$$

where the definition of u, z and the coefficients are

$$\begin{cases} z = |x| \\ u = \dfrac{1}{1 + 0.5\, z} \end{cases}$$

and

$$\begin{cases} a_0 = -1.26551223 \\ a_1 = +1.00002368 \\ a_2 = +0.37409196 \\ a_3 = +0.09678418 \\ a_4 = -0.18628806 \\ a_5 = +0.27886807 \\ a_6 = -1.13520398 \\ a_7 = +1.48851587 \\ a_8 = -0.82215223 \\ a_9 = +0.17087277 \,. \end{cases}$$

CHAPTER FOUR
THE OBSERVATION AND DATA FITTING

4.1 Introduction

Perpendicular (along the minor-radial direction in the plasma midplane) and parallel (along the toroidal direction also in the plasma midplane) diffusion was observed under several different conditions, such as low ($B_t \approx 1.95\,(kG)$) and high ($B_t \approx 3.5\,(kG)$) toroidal magnetic field at the fill pressure $10\,(mTorr)$. Diffusion coefficient was obtained by observation of the C_{II} and C_{III} lines, involving a spatial scan at three different locations from the carbon tip, i.e. 1.5, 2.5 and 4.7 (cm).

In order to get the carbon line emission from the discharge of the carbon probe, we subtract the background signal. The background arises from carbon probe ablation by plasma protons and electrons as well as the continuum spectrum of plasma bremsstrahlung radiation.

When we use the diffusion models discussed in the previous chapter, there are *three* adjustable parameters (the ionization time $\left[\frac{1}{I}\right]$ and the parallel and perpendicular diffusion coefficients $D_{2\|}$, $D_{2\perp}$ for C^+ ions) for the fitting of C_{II} light signals, and *two* more parameters (the parallel and perpendicular diffusion coefficients $D_{3\|}$, $D_{3\perp}$ for C^{++} ions) for the fitting of C_{III} light signals.

The fitting procedure for C_{II} signals is that first we choose the ionization time ($C^+ \rightarrow C^{++}$) according to the electron temperature and density (see section 3.3) and, keeping it fixed, adjusting the choices of $D_{2\|}$ and $D_{2\perp}$ to fit the data. Usually the fitting of the parallel diffusion measurement was done first since in this case more C^+ ions diffuse along the toroidal direction than diffuse along the minor-radial direction because of the toroidal magnetic field. Note that only $D_{2\|}$ appears in the exponential part (see

equation (3.5.11)) while $D_{2\perp}$ is included in the denominator when we set $x = y = 0$ and $z \neq 0$; therefore $D_{2\|}$ has more effect on the data than $D_{2\perp}$ in this geometry. Then the fitting of perpendicular measurement was done by using the values of $\left[\frac{1}{I}\right]$ and $D_{2\|}$ obtained from the parallel measurement. After the fitting of all of the measurement of C_{II} light, the values of $\left[\frac{1}{I}\right]$, $D_{2\|}$ and $D_{2\perp}$ were kept constant in the fitting of the diffusion coefficients of the C_{III} light. Similarly we did the calculation for the parallel measurement first, and then for the perpendicular one.

All of the three models, i.e. the delta function source model, the squarewave function source model and the sinewave function source model, were used in the numerical fitting in each case. Since they all have similar behavior especially when the observation point is far away from the source point (see Fig.3.14), only the fitting curve from delta function source model is plotted for clarity. In order to reduce the noise from the PMT all of the signals are processed by a noise-smoothing subroutine. This smoother averages every data point with six adjacent points which are evenly distributed on both sides of the given data point, and, therefore this functions like a low pass filter since it averages over 1.2 (μsec) of the 0.2 (μsec) digitizer sampling period; and the fastest characteristic time for the signal change is about 5 – 10 (μsec) depending on the location of the view point.

4.2 The Diffusion Coefficient Measurements

The C_{II} light measurements along the radial and toroidal directions at low toroidal magnetic field ($B_t = 1.95$ (kG)) and the theoretically predicted curves from the delta function source model are shown in Fig.4.1(a) and (b), respectively; and the case for higher toroidal magnetic field ($B_t = 3.5$ (kG)) is shown in Fig.4.2(a) and (b). Fig.4.3(a) and (b) show C_{III} light signals in the perpendicular and parallel directions at low

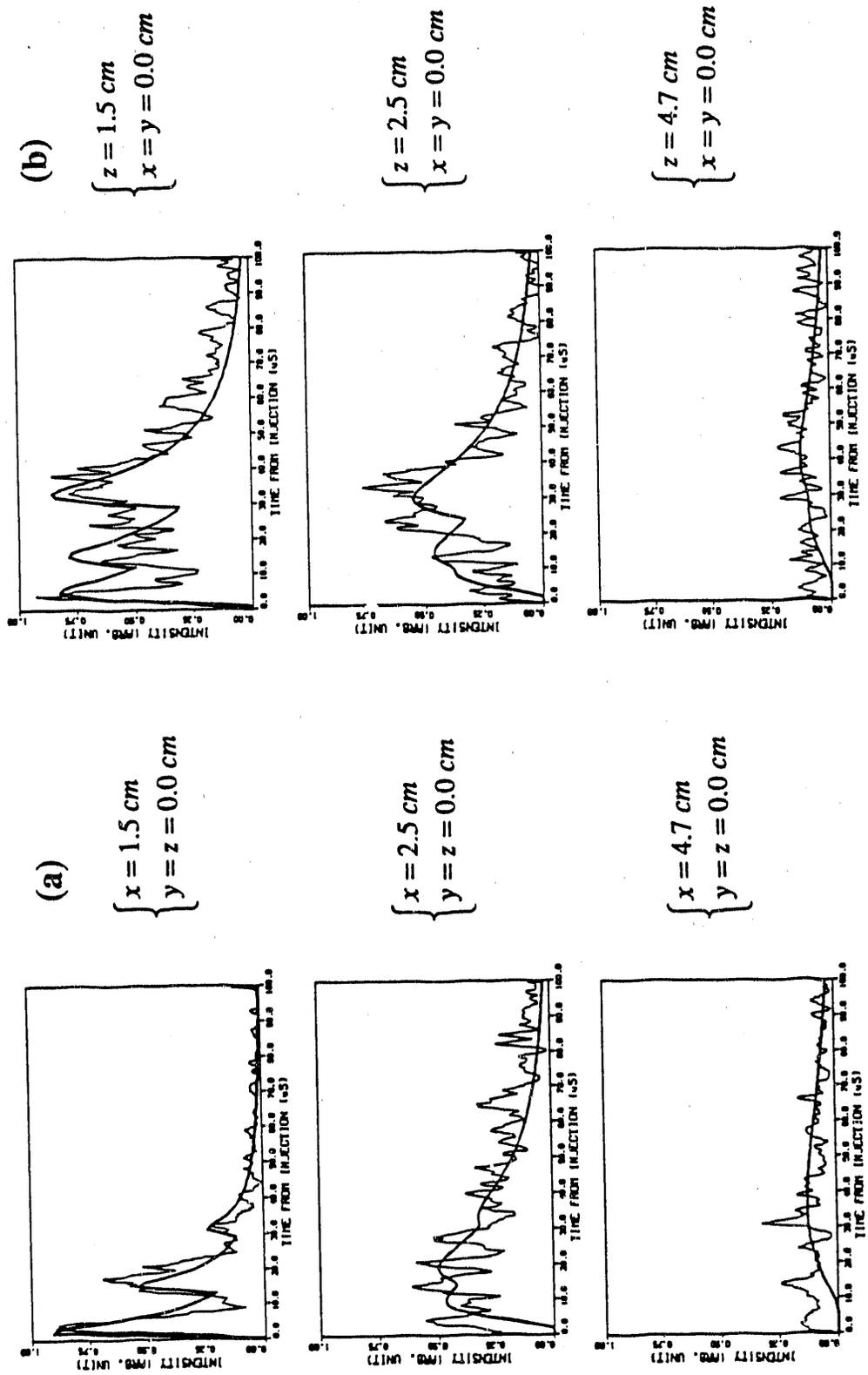

Figure 4.1 The C_{II} light measurement and the fitted solution of equation (3.5.11) (solid line) at low toroidal magnetic field (B_t =1.95 (kG)) in (a)the minor-radial and (b)the toroidal directions .

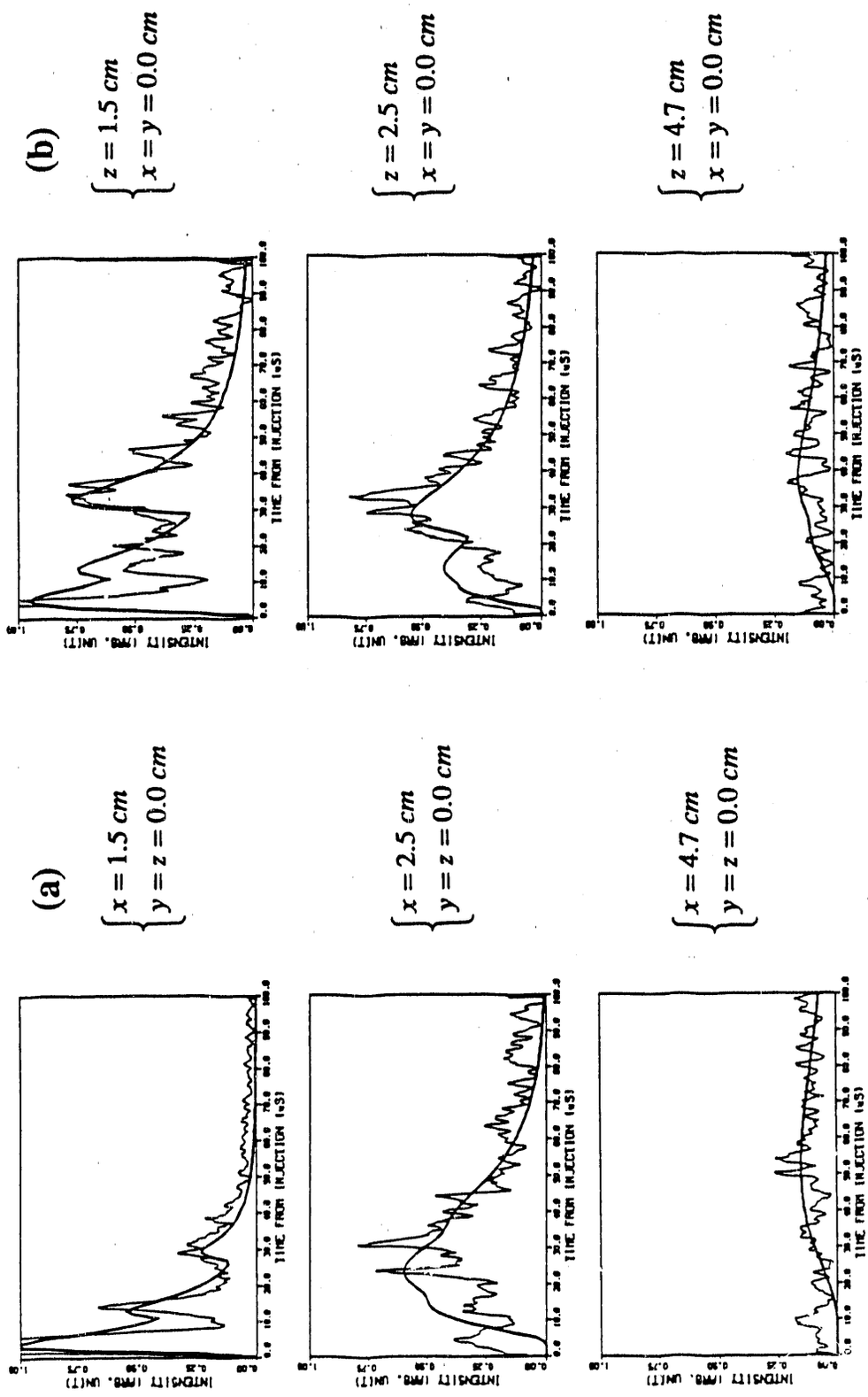

Figure 4.2 The C_{II} light measurement and the fitted solution of equation (3.5.11) (solid line) at high toroidal magnetic field (B_t =3.5 (kG)) in (a)the minor-radial and (b)the toroidal directions .

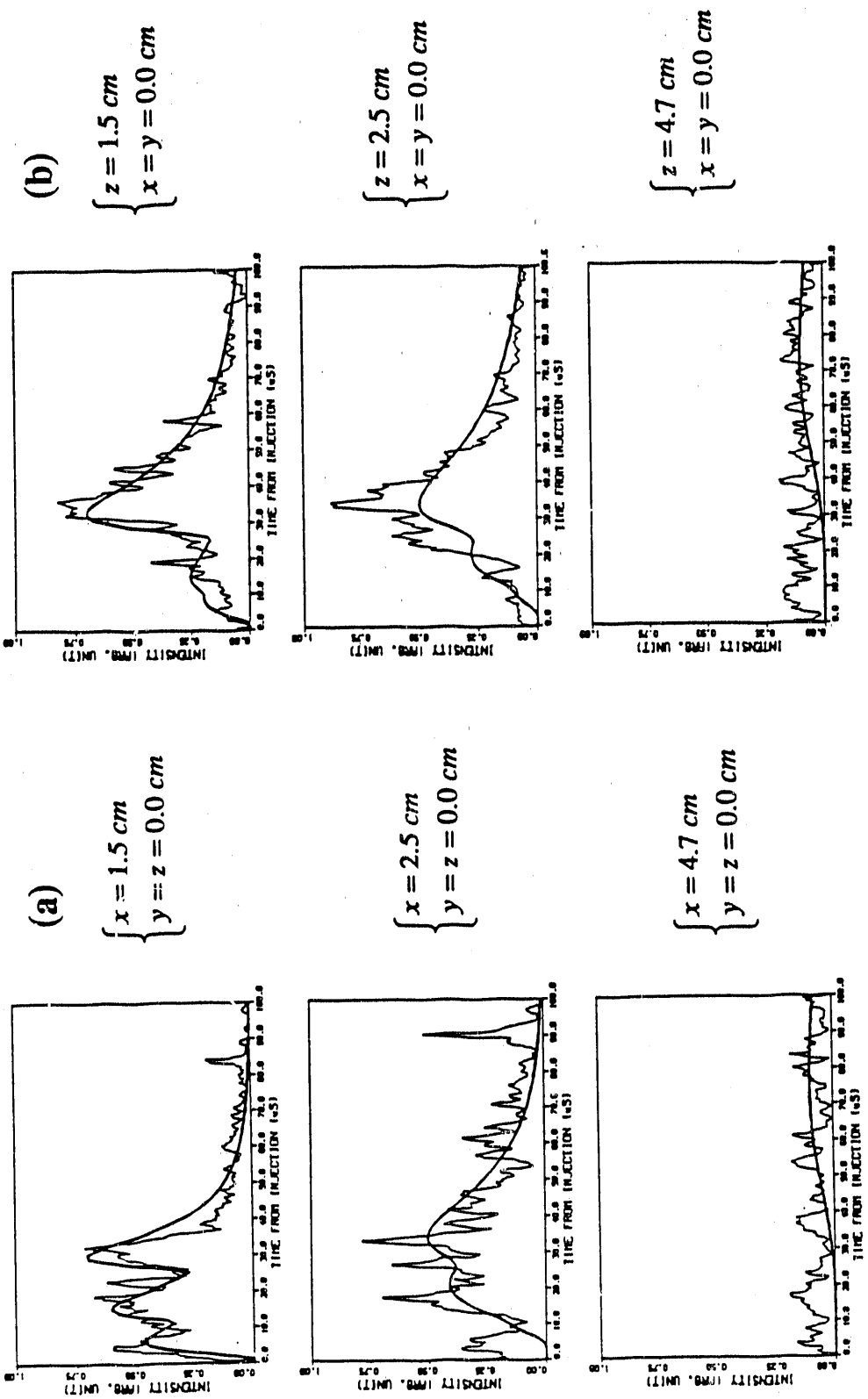

Figure 4.3 The C_{III} light measurement and the fitted solution of equation (3.5.11) (solid line) at low toroidal magnetic field (B_t =1.95 (kG)) in (a)the minor-radial and (b)the toroidal directions .

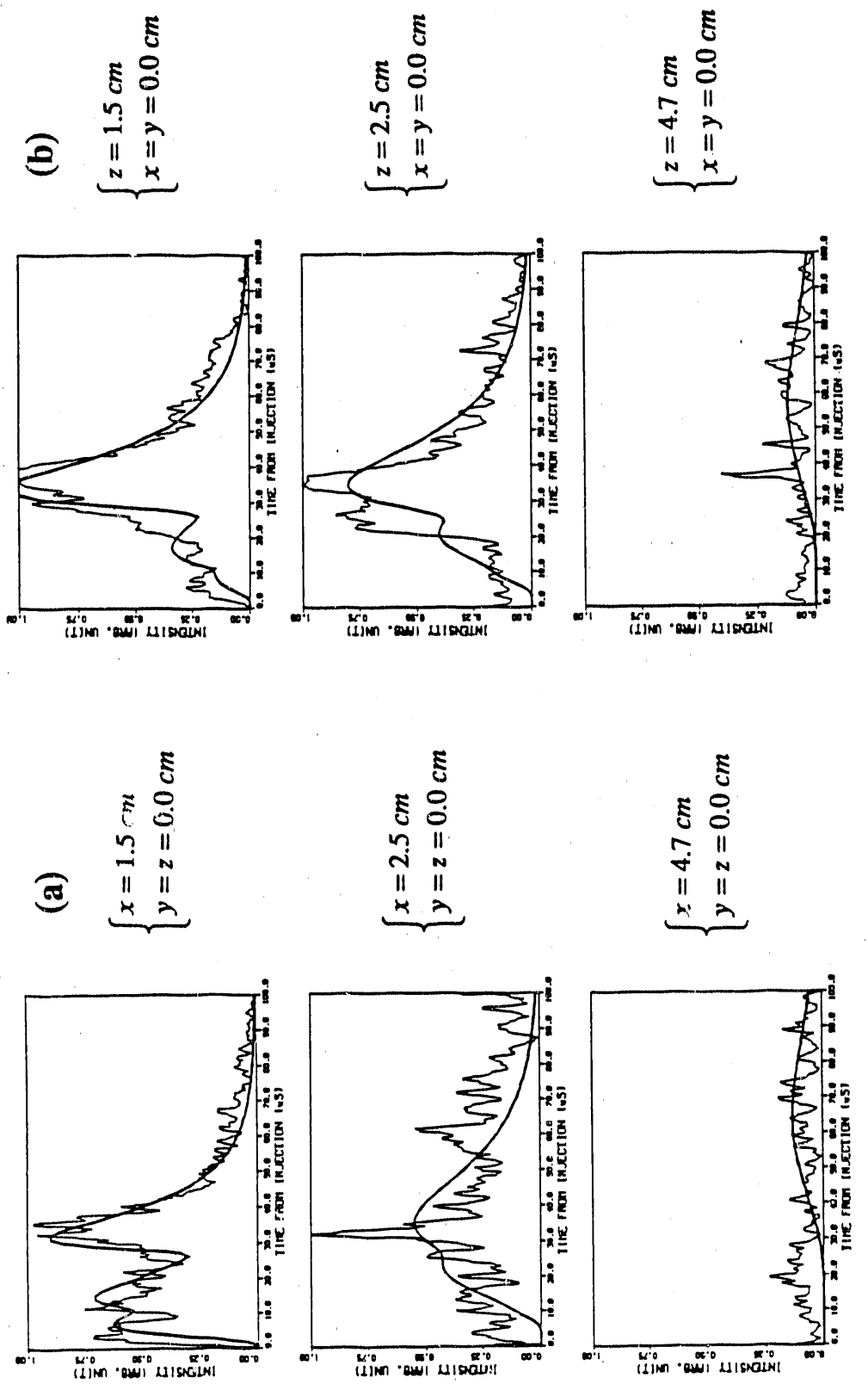

Figure 4.4 The C_{III} light measurement and the fitted solution of equation (3.5.11) (solid line) at high toroidal magnetic field (B_t =3.5 (kG)) in (a) the minor-radial and (b) the toroidal directions.

B-field, and Fig.4.4(a) and (b) for high B-field. In all of the numerical fitting, the ionization time $\left[\frac{1}{I}\right]$ is fixed at 30.0 (μsec) according to the electron temperature ($4-10$ (eV)) and density ($1-3\times10^{14}$ (cm^{-3})) in the HBT plasmas[18]. But in order to get the best fit on the tail part of the data (e.g. when $t \geq 50.0$ (μsec)), $\left[\frac{1}{I}\right]$ has to be varied between 20.0 (μsec) to 40.0 ($musec$).

We next present a list of the five adjustable parameters used in the numerical fitting for each case at different spatial location in the plasma and different magnetic field. The shot that we have chosen for the fitting are selected to the "good" shot which is taken under a normal operating condition and has a good plasma current profile and good internal magnetic field structure according to other diagnostics, such as magnetic probe, Rogowski coil, etc..

- Case 1: for C_{II} light (shown in Fig.4.1(a)):

$$\begin{cases} \textit{Low Toroidal B-field at } B_t = 1.95\ (kG), \\ \textit{Along Minor-radial Direction}: x = 1.5\ cm,\ 2.5\ cm,\ 4.7\ cm \text{ and} \\ \qquad\qquad y = z = 0.0\ cm, \end{cases}$$

$$\begin{cases} D_{2\parallel} = 14.0\ (m^2/sec), \\ D_{2\perp} = 9.5\ (m^2/sec), \\ \frac{1}{I} = 30.0\ (\mu sec). \end{cases}$$

- Case 2: for C_{II} light (shown in Fig.4.1(b)):

$$\begin{cases} \textit{Low Toroidal B-field at } B_t = 1.95\ (kG), \\ \textit{Along Toroidal Direction}: z = 1.5\ cm,\ 2.5\ cm,\ 4.7\ cm \text{ and} \\ \qquad\qquad x = y = 0.0\ cm, \end{cases}$$

$$\begin{cases} D_{2\parallel} = 14.0\ (m^2/sec)\ , \\ D_{2\perp} = 9.5\ (m^2/sec)\ , \\ \frac{1}{I} = 30.0\ (\mu sec)\ . \end{cases}$$

- Case 3: for C_{II} light (shown in Fig.4.2(a)):

$$\begin{cases} \textit{High Toroidal B-field at } B_t = 3.5\ (kG)\ , \\ \textit{Along Minor-radial Direction}: x = 1.5\ cm,\ 2.5\ cm,\ 4.7\ cm \text{ and} \\ \qquad y = z = 0.0\ cm\ , \end{cases}$$

$$\begin{cases} D_{2\parallel} = 14.0\ (m^2/sec)\ , \\ D_{2\perp} = 5.5\ (m^2/sec)\ , \\ \frac{1}{I} = 30.0\ (\mu sec)\ . \end{cases}$$

- Case 4: for C_{II} light (shown in Fig.4.2(b)):

$$\begin{cases} \textit{High Toroidal B-field at } B_t = 3.5\ (kG)\ , \\ \textit{Along Toroidal Direction}: z = 1.5\ cm,\ 2.5\ cm,\ 4.7\ cm \text{ and} \\ \qquad x = y = 0.0\ cm\ , \end{cases}$$

$$\begin{cases} D_{2\parallel} = 14.0\ (m^2/sec)\ , \\ D_{2\perp} = 5.5\ (m^2/sec)\ , \\ \frac{1}{I} = 30.0\ (\mu sec)\ . \end{cases}$$

- Case 5: for C_{III} light (shown in Fig.4.3(a)):

$$\begin{cases} \textit{Low Toroidal B-field at } B_t = 1.95\ (kG)\ , \\ \textit{Along Minor-radial Direction}: x = 1.5\ cm,\ 2.5\ cm,\ 4.7\ cm \text{ and} \\ \qquad y = z = 0.0\ cm\ , \end{cases}$$

$$\begin{cases} D_{2\parallel} = 14.0\ (m^2/sec), \\ D_{2\perp} = 9.5\ (m^2/sec), \\ D_{3\parallel} = 3.8\ (m^2/sec), \\ D_{3\perp} = 3.3\ (m^2/sec), \\ \frac{1}{I} = 30.0\ (\mu sec). \end{cases}$$

- Case 6: for C_{III} light (shown in Fig.4.3(b)):

$$\begin{cases} \textit{Low Toroidal B-field at } B_t = 1.95\ (kG), \\ \textit{Along Toroidal Direction}: z = 1.5\ cm,\ 2.5\ cm,\ 4.7\ cm \text{ and} \end{cases}$$

$$x = y = 0.0\ cm,$$

$$\begin{cases} D_{2\parallel} = 14.0\ (m^2/sec), \\ D_{2\perp} = 9.5\ (m^2/sec), \\ D_{3\parallel} = 3.8\ (m^2/sec), \\ D_{3\perp} = 3.3\ (m^2/sec), \\ \frac{1}{I} = 30.0\ (\mu sec). \end{cases}$$

- Case 7: for C_{III} light (shown in Fig.4.4(a)):

$$\begin{cases} \textit{High Toroidal B-field at } B_t = 3.5\ (kG), \\ \textit{Along Minor-radial Direction}: x = 1.5\ cm,\ 2.5\ cm,\ 4.7\ cm \text{ and} \end{cases}$$

$$y = z = 0.0\ cm,$$

$$\begin{cases} D_{2\parallel} = 14.0\ (m^2/sec), \\ D_{2\perp} = 5.5\ (m^2/sec), \\ D_{3\parallel} = 3.8\ (m^2/sec), \\ D_{3\perp} = 2.0\ (m^2/sec), \\ \frac{1}{I} = 30.0\ (\mu sec). \end{cases}$$

- Case 8: for C_{III} light (shown in Fig.4.4(b)):

$$\begin{cases} \textit{High Toroidal } B\textit{-field at } B_t = 3.5\ (kG), \\ \textit{Along Toroidal Direction}: z = 1.5\ cm,\ 2.5\ cm,\ 4.7\ cm \text{ and} \end{cases}$$

$$x = y = 0.0\ cm,$$

$$\begin{cases} D_{2\parallel} = 14.0\ (m^2/sec), \\ D_{2\perp} = 5.5\ (m^2/sec), \\ D_{3\parallel} = 3.8\ (m^2/sec), \\ D_{3\perp} = 2.0\ (m^2/sec), \\ \frac{1}{I} = 30.0\ (\mu sec). \end{cases}$$

Another eleven shots, not shown here, are also numerically fitted to obtain additional diffusion coefficients according to the procedure just described. The scattering of these parallel diffusion coefficients at different locations and directions are summarized in Fig.4.5, and the perpendicular diffusion coefficients are presented in Fig.4.6 in the same way. It should be pointed out that the diffusion coefficients obtained from the measurements at distance 4.7 (cm) from the source are not plotted in either Fig.4.5 and Fig.4.6 since the signal-to-noise ratio is close to one and the fitting is not reliable. Finally the perpendicular diffusion coefficients for C^+ and C^{++} ions are plotted *versus* the toroidal magnetic field in Fig.4.7.

From these numbers of the diffusion coefficients obtained in the numerical fitting, we can summarize our conclusions as follow. First, the four diffusion coefficients, $D_{2\parallel}$, $D_{2\perp}$, $D_{3\parallel}$, and $D_{3\perp}$, are found to be independent of the location of the observation point, as would expected if the diffusion model is correct. Second, the dependence on the toroidal magnetic field is observed only for perpendicular diffusion coefficients. The toroidal magnetic field may affect the parallel diffusion coefficient through the electron temperature and density, but there is no evidence to show the direct dependence of the

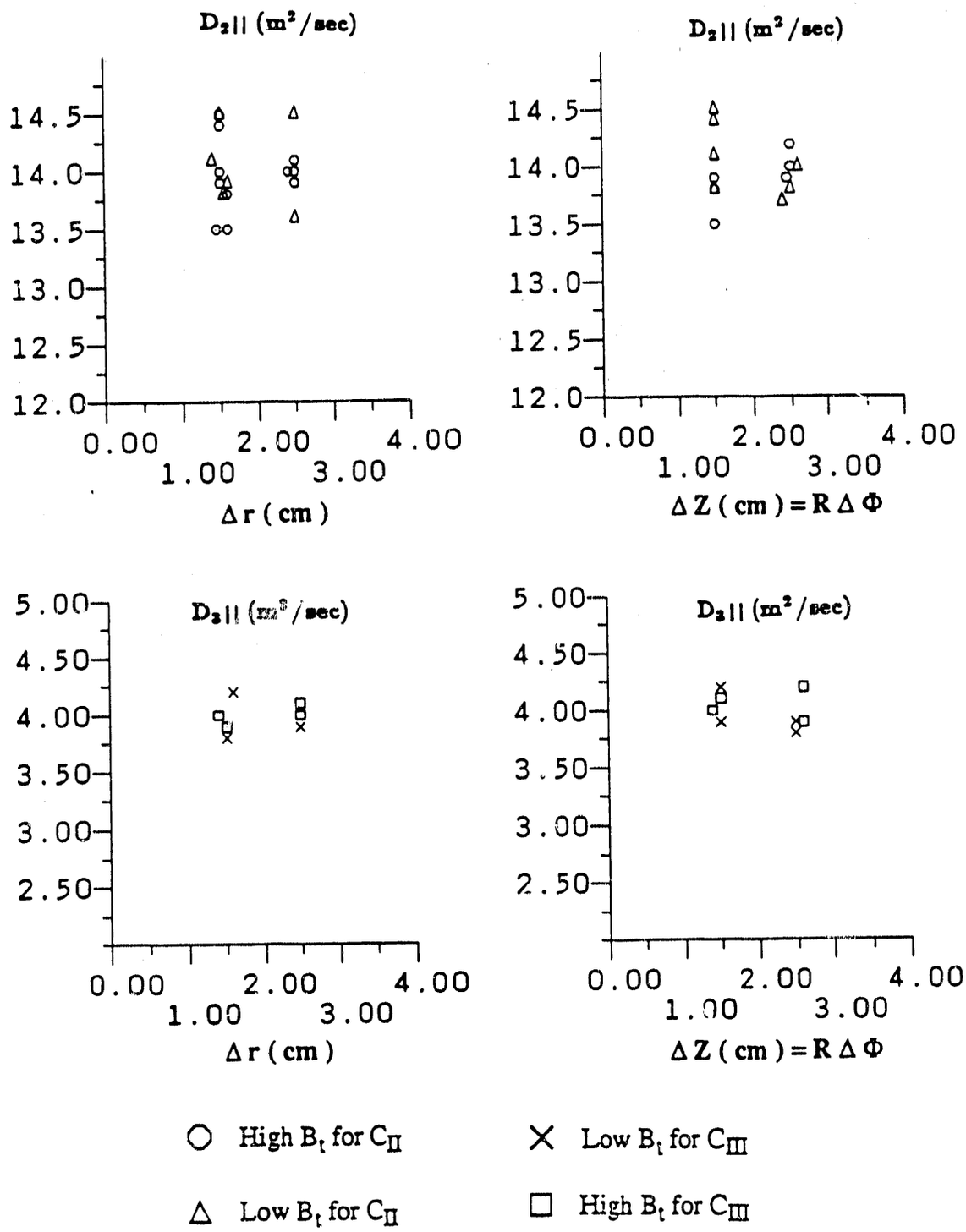

Figure 4.5 The parallel diffusion coefficients for C_{II} and C_{III} at different radial and toroidal locations from the source point. Low B_t is for B_t =1.95 (kG) and high B_t is for B_t =3.5 (kG).

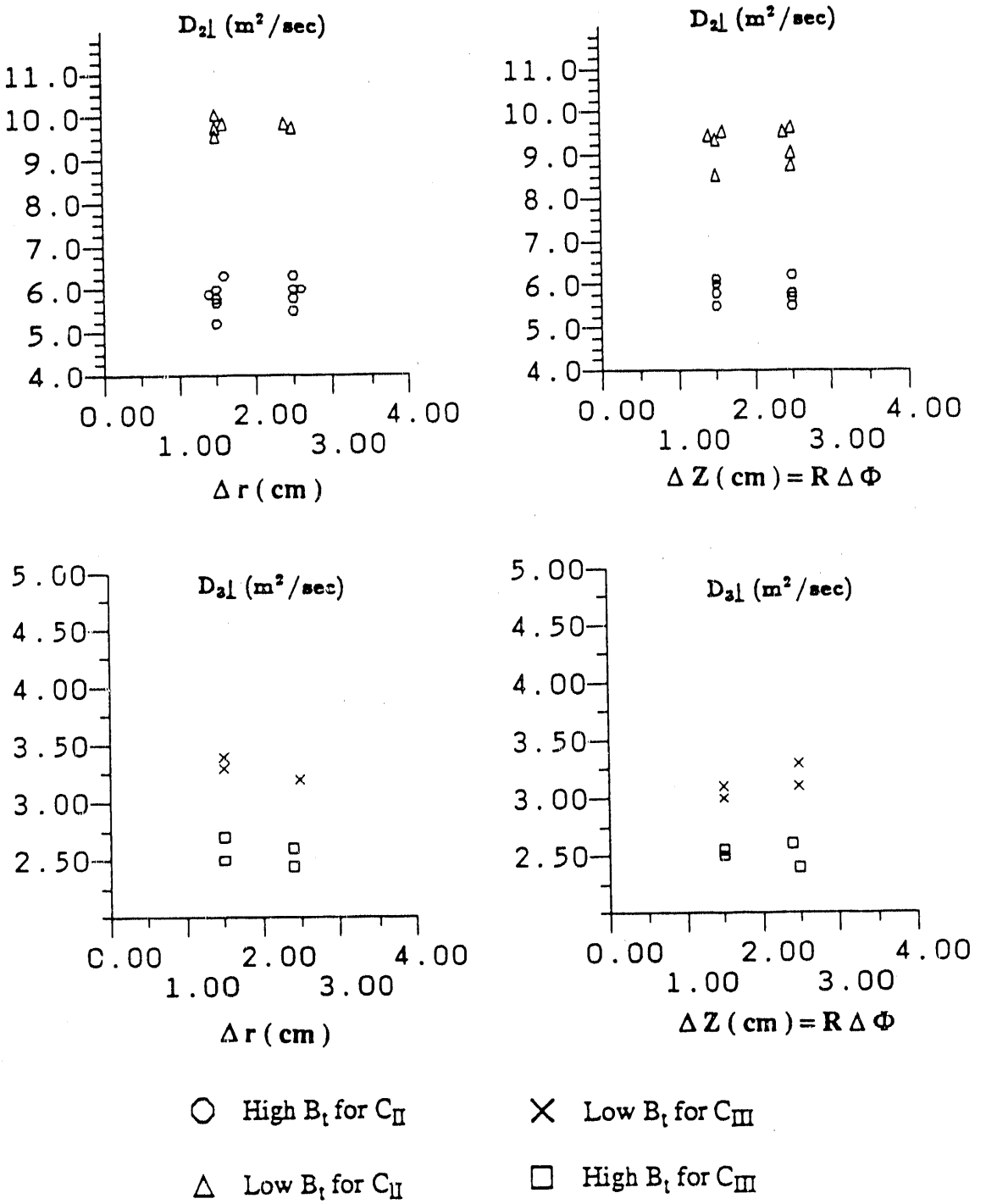

Figure 4.6 The perpendicular diffusion coefficients for C_{II} and C_{III} at different radial and toroidal locations from the source point. Low B_t is for B_t =1.95 (kG) and high B_t is for B_t =3.5 (kG) .

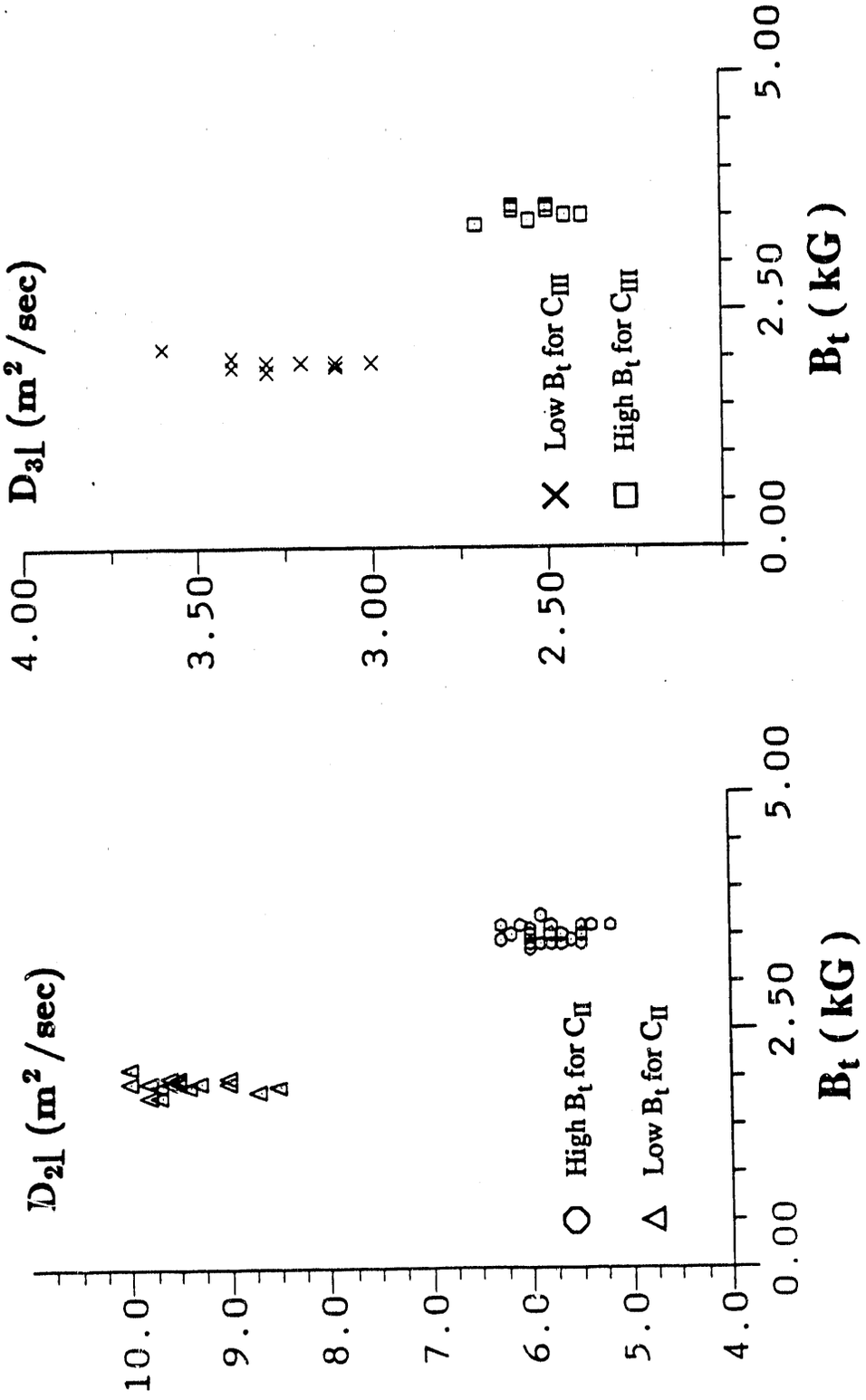

Figure 4.7 The perpendicular diffusion coefficients for (a) C_{II} and (b) C_{III} at different toroidal magnetic field.

parallel diffusion coefficients on the magnetic field.

Several other issues must be pointed out. First, in the calculation of the theoretical curves, a 5% change in the dominant diffusion coefficient can result in a visibly different curve. The fitting sensitivity decreases as the observation distance from the source point increases. When the view point is 4.7 (cm) away from the carbon tip, this sensitivity drops to about $10-15\%$.

Second, in the fitting processes we found that it is difficult to keep the relative levels of the three initial pulses of carbon light exactly proportional to the peak values of the discharge current from the carbon probe. If there were only one pulse from the source this trouble could be avoided by normalizing the data to arbitrary unit. But in our case, these relative levels have to be shifted as much as $30-40\%$ from the proportionality obtained from the source discharge current, for some shots, to get the best diffusion coefficient fit. These uncertainties could arise from either the fluctuations of the source discharge (see section 2.4), or some instability which can cause a sudden bulk motion of the plasma *into* or *out of* the small volume of a chordal measurement.

Finally, there is some fluctuation in the starting time from the three pulses in the firing of the carbon probe. This shift is usually very small ($1-2$ (μsec)) compared with the characteristic diffusion time scale ($50-100$ (μsec)). Normally this fluctuation is compensated by the corresponding shift in the model curve according to the discharge current profile shot by shot and can be neglected.

4.3 Convection Effect

A convection effect would arise from a bulk motion of the plasma, possibly in both the minor-radial and toroidal directions. This motion could come from either toroidal rotation of plasma or minor-radial plasma expansion. Some instabilities can also cause a convective motion.

Now we consider the carbon probe to be located at the origin of the *static* coordinate system $O-xyz$ (i.e. the lab frame), while another coordinate system, say $O'-x'y'z'$, is moving with the plasma at the *convective velocity* $\vec{V}_c(t)$. Since the convective velocity is much smaller than the speed of light (i.e. non-relativistic case), then, according to Galilean relativity, the transformation of time and space coordinates between these two systems is:

$$\begin{cases} t = t' \\ \vec{r} = \vec{r}' + \vec{V}_c\, t \end{cases} \tag{4.3.1}$$

The diffusion problem can be written in the system of either $O-xyz$ or $O'-x'y'z'$ as follows:

$$\frac{\partial}{\partial t} n(t,\vec{r}) = D\,\nabla^2 n(t,\vec{r}) - A\, n(t,\vec{r}) + S(t,\vec{r}) \tag{4.3.2}$$

$$(\textit{in } O-xyz \textit{ system}),$$

or

$$\frac{\partial}{\partial t} n(t,\vec{r}') = D\,\nabla'^2 n(t,\vec{r}') - A\, n(t,\vec{r}') + S(t,\vec{r}') \tag{4.3.3}$$

$$(\textit{in } O'-x'y'z' \textit{ system}).$$

Note here we have assumed that the diffusion coefficients are the same in both systems. The operator ∇^2 and ∇'^2 is the same in the two systems because:

$$\begin{aligned} \nabla^2 &= \frac{\partial^2}{\partial \vec{r}^2} = \frac{\partial}{\partial \vec{r}}\left[\frac{\partial}{\partial \vec{r}}\right] = \left[\frac{\partial}{\partial \vec{r}'}\frac{\partial \vec{r}'}{\partial \vec{r}}\right]\left[\frac{\partial}{\partial \vec{r}'}\frac{\partial \vec{r}'}{\partial \vec{r}}\right] \\ &= \frac{\partial}{\partial \vec{r}'}\left[\frac{\partial}{\partial \vec{r}'}\right] = \frac{\partial^2}{\partial \vec{r}'^2} = \nabla'^2 . \end{aligned} \tag{4.3.4}$$

Even though equations (4.3.2) and (4.3.3) have the same form, the source terms in these two equations are different. In $O-xyz$ system, the source is at rest $\vec{V}_{source} = 0$. But in $O'-x'y'z'$ system, according to the transformation (4.3.1), the source is now in

motion at the speed of:

$$\vec{V}'_{source} = \vec{V}_{source} - \vec{V}_c = -\vec{V}_c \,. \tag{4.3.5}$$

This indicates that the convection effect in the $O-xyz$ system is equivalent to the diffusion problem in $O'-x'y'z'$ system where the source is moving at the negative speed of the convection motion.

Since the *Green's function* of problem (4.3.3) is:

$$G\,(t,\,x',y',z') = \frac{1}{8\,\pi^{3/2}} \frac{e^{-At}}{\sqrt{D_x t}\sqrt{D_y t}\sqrt{D_z t}} \times$$

$$\exp\left[-\frac{x'^2}{4D_x t} - \frac{y'^2}{4D_y t} - \frac{z'^2}{4D_z t} \right], \tag{4.3.6}$$

we compare with the *Green's function* of problem (4.3.2) expressed in equation (3.5.6) and we have the following relation between the solutions obtained in the two coordinate systems[25] (proof is omitted here):

$$n\,(t,\vec{r}\,') = n\,(t,\vec{r} - \vec{V}_c\,t\,)\,. \tag{4.3.7}$$

This is generally true for all of the three models. Next, for simplicity, we discuss only the delta function source model, but it turns out that the conclusions obtained here are also applicable to the other two models.

The solution of problem (4.3.3) is:

$$n\,(t,\,x',y',z') = \frac{1}{8\,\pi^{3/2}} \frac{e^{-At}}{\sqrt{D_x t}\sqrt{D_y t}\sqrt{D_z t}} \times$$

$$\exp\left[-\frac{(x - V_{c,x}t)^2}{4D_x t} - \frac{(y - V_{c,y}t)^2}{4D_y t} - \frac{(z - V_{c,z}t)^2}{4D_z t} \right]. \tag{4.3.8}$$

When the convective velocity $\vec{V}_c = 0$, then we have $n\,(t,\,x',y',z') = n\,(t,\,x,y,z\,)$. Also from equation (4.3.8), when $|\vec{r}\,| \gg |\vec{V}_c\,t\,|$, the convective term is negligible, here $|\vec{r}\,|$ is

the distance between the observation point and the source point, and t is the characteristic diffusion time. Since $r^2 \approx Dt$, then we can express the criterion for the negligence of convective effect as:

$$|\vec{V}_c| \ll \left[\frac{D}{t} \right]^{1/2} . \tag{4.3.9}$$

This means that when the diffusion coefficient is large enough, or the observation point is close enough to the source, then the convection effect is weak and the process is dominated by diffusion.

Next is a numerical example for the estimation of equation (4.3.8). The average perpendicular diffusion coefficient is about $D = 5.0\ (m^2/sec)$ for either $D_{2\perp}$ and $D_{3\perp}$, or low and high magnetic field cases, then the quantity $\left[\frac{D}{r} \right]^{1/2}$ on the right hand side of equation (4.3.8), for $r = 1.5$, 2.5, and 4.7 (cm), is 333.0, 200.0 and 106.0 (m/sec), respectively. Taking the average value of $\left[\frac{D}{r} \right]^{1/2} = 200.0\ (m/sec)$, then $V_c \ll 2 \times 10^4$ (cm/sec) is required to neglect the convection flow in the minor-radial direction. This is also means that the plasma should move, convectively, $\ll 1.0\ (cm)$ in $50.0\ (\mu sec)$, which is the characteristic time scale for the carbon ion diffusion. According to the internal magnetic probe data, the toroidal magnetic field lines are stationary as to radial motion during $50.0\ (\mu sec)$ time scale. Therefore, if the plasma flows, it would have to *cross* the magnetic field lines. However, this could occur only by resistive flow, and can be estimated from the plasma resistivity. Since the initial configuration of magnetic field will decay away in a diffusion time[28]:

$$\tau_d = \frac{4\pi\sigma_\perp L^2}{c^2} \quad (in\ CGS\ unit)\ , \tag{4.3.10}$$

where L is the characteristic length scale of spatial variation of $\vec{B}$ (chosen as the plasma

radius $L = a = 5.0\ (cm)$); $\sigma_\perp = \frac{1}{\eta_\perp}$ is the plasma conductivity across $\vec{B}$. The plasma resistivity transverse to the magnetic field, $\eta_\perp$, is given by the following formula[29]:

$$\eta_\perp = 1.04 \times 10^{-4} \frac{Z \ln \Lambda}{T_e(eV)^{3/2}} \quad (\Omega \cdot m) \tag{4.3.11}$$

$$(\textit{in MKS Unit}),$$

or

$$\eta_\perp = 1.16 \times 10^{-14} \frac{Z \ln \Lambda}{T_e(eV)^{3/2}} \quad (\textit{second}) \tag{4.3.12}$$

$$(\textit{in Gaussian Unit}).$$

When we choose $T_e = 10\ (eV)$, $Z = 1$, and $\ln \Lambda = 10$, then $\eta_\perp = 3.7 \times 10^{-15}\ (sec)$, the magnetic diffusion time is:

$$\begin{aligned}
\tau_d &= \frac{4\pi L^2}{\eta_\perp c^2} \\
&= \frac{4\pi \times 5.0^2\ (cm^2)}{3.7 \times 10^{-15}\ (sec) \times 9 \times 10^{20}\ (cm^2/sec^2)} \\
&= 9.43 \times 10^{-5}\ (sec) = 94.3\ (\mu sec).
\end{aligned}$$

If we use this characteristic time to estimate the plasma radial flow, the convective velocity should be

$$\begin{aligned}
V_c &= \frac{a}{\tau_d} = \frac{5.0\ (cm)}{9.43 \times 10^{-5}\ (sec)} \\
&= 5.3 \times 10^4\ (cm/sec) = 530.0\ (m/sec).
\end{aligned}$$

However, from the H_α light measurement which will be discussed in chapter six, the emissivity contour in the plasma cross section doesn't change much during the time scale mentioned above. This indicates that the plasma radial flow is not as high as the estimate, and the convection is not strong enough to affect the radial diffusion of carbon

ions in the characteristic diffusion time scale.

The criterion to neglect convection when taking the measurement in the toroidal direction is also $V_c \ll 2 \times 10^4$ (cm/sec) since the parallel diffusion coefficient is in the same order as the perpendicular one.

A noteworthy point from equation (4.3.8) is that the toroidal convection flow can also affect the radial diffusion process, and vice versa, because if one sets $x \neq 0$ and $y = z = 0$ in equation (4.3.8), the parallel diffusion coefficient D_z still appears in the exponential part through the factor $-\frac{(V_{c,z}t)^2}{4D_z t}$. This is easy to understand physically since toroidal convection will carry away the carbon ions (in the toroidal direction) from the volume located along the minor-radial direction where the measurement is being made. The toroidal plasma rotation in Torus II (the early version of HBT) was measured by studying the Doppler shift of the 4,686 *A He II* line[30]. It was found that, typically, the toroidal flow motion is in the same direction as the plasma current at an average velocity of $V_{c,z} = V_\Phi \simeq 10^6$ (cm/sec), a small fraction of the plasma ion thermal speed. This is much larger than the criterion value 10^4 (cm/sec), so the toroidal rotation could affect the diffusion measurement of carbon ions. However, the toroidal flow in Torus II was observed to damp out in ~ 10 (μsec).

In order to get a quantitative estimate of the convection effect, some solutions, under different conditions, of equation (4.3.8), are plotted in Fig.4.8(a) and (b), Fig.4.9(a) and (b), and Fig.4.10(a) and (b) at three different locations in the minor-radial direction in the laboratory frame. The toroidal convection velocity used in the calculation as shown in the figures, is $V_{c,z} = 0.0$, 1.0, 10.0, 100.0, 1,000.0 and 10,000.0 (m/sec), and the radial convection velocity is $V_{c,x} = 0.0$ in (a) and 500.0 (m/sec) in (b), respectively.

From these plots we can see that up to 500.0 (m/sec) radial convection velocity

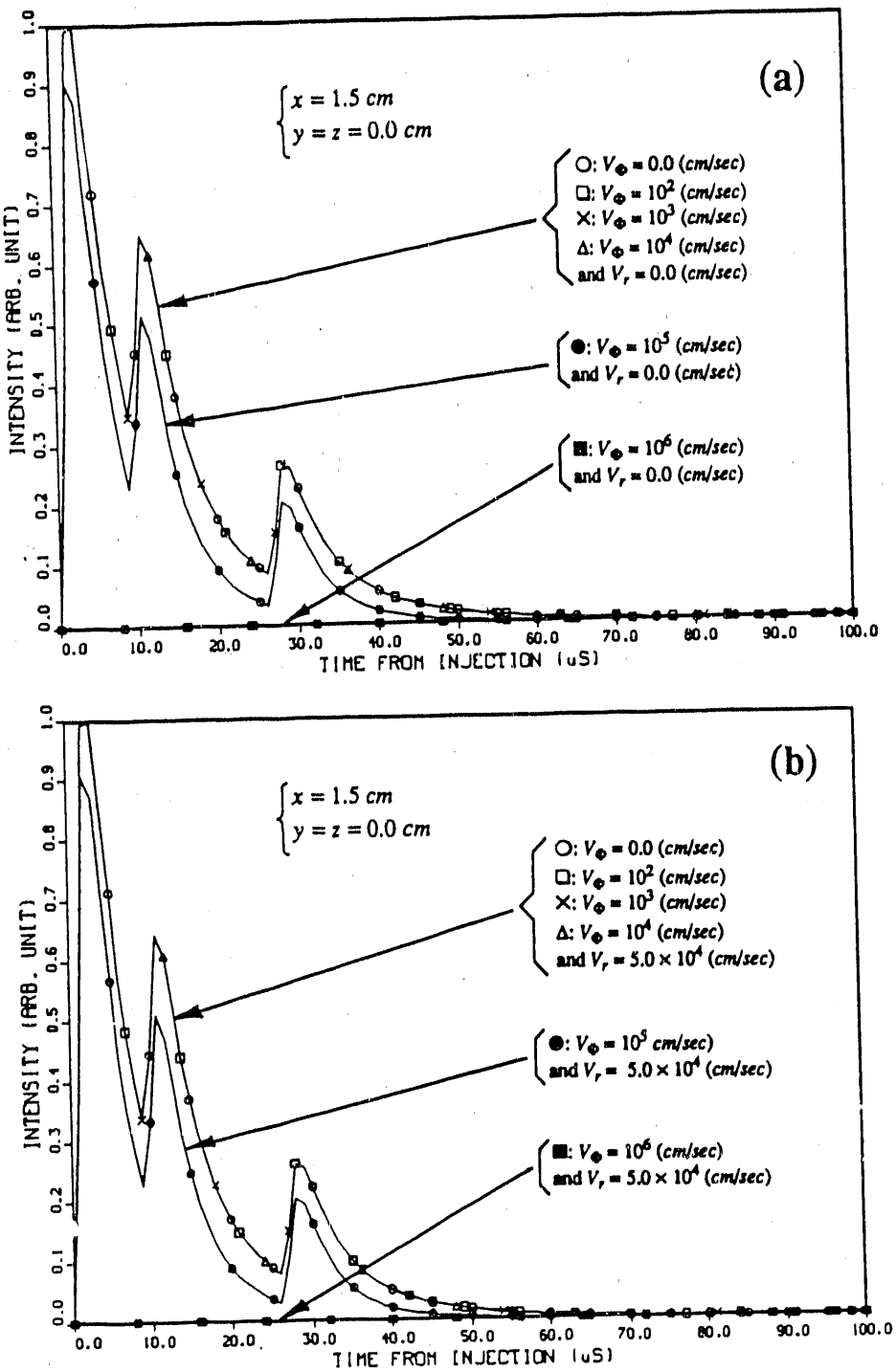

Figure 4.8 The solutions of equation (4.3.8) at $x = 1.5$ (cm) and $y = z = 0.0$ from five differe t toroidal convection velocities. The radial convection velocity is (a)zero and (b)500.0 (m/sec), respectively .

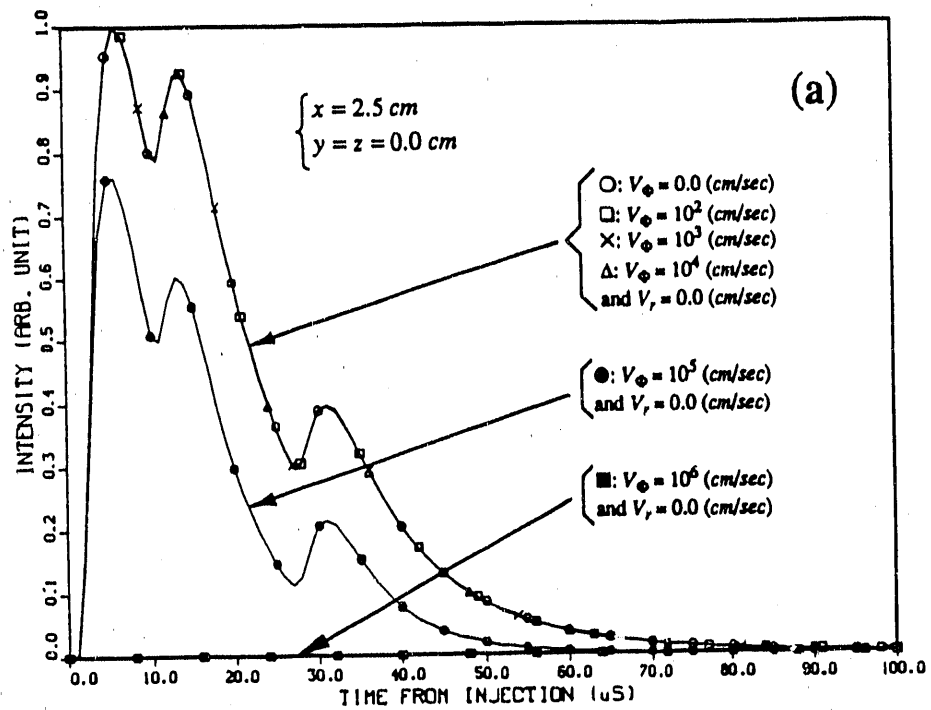

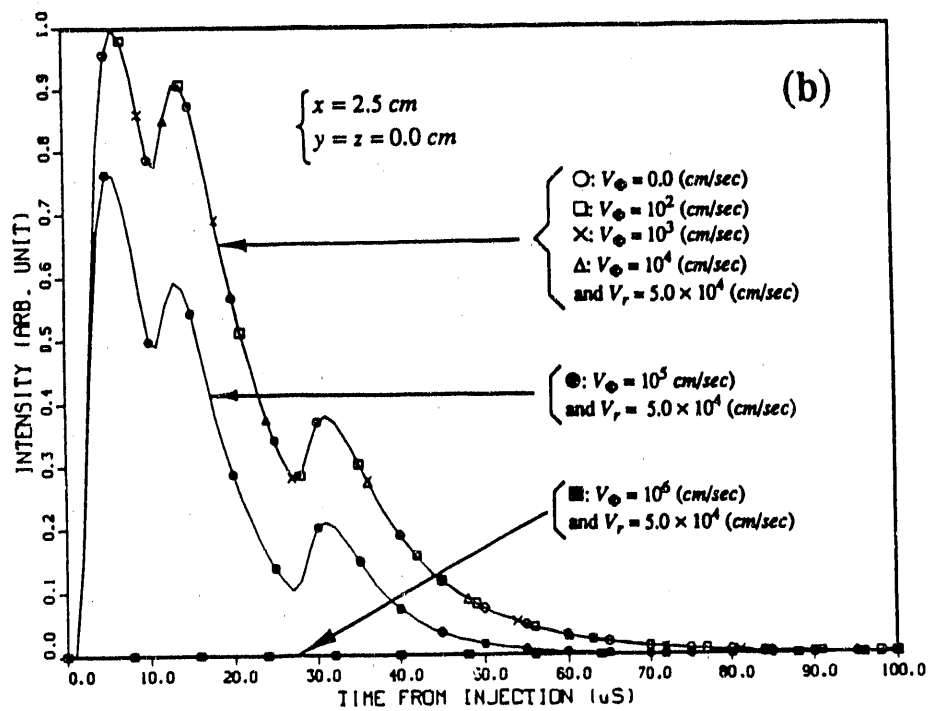

Figure 4.9 The solutions of equation (4.3.8) at $x = 2.5$ (cm) and $y = z = 0.0$ from five different toroidal convection velocities. The radial convection velocity is (a) zero and (b)500.0(m/sec), respectively .

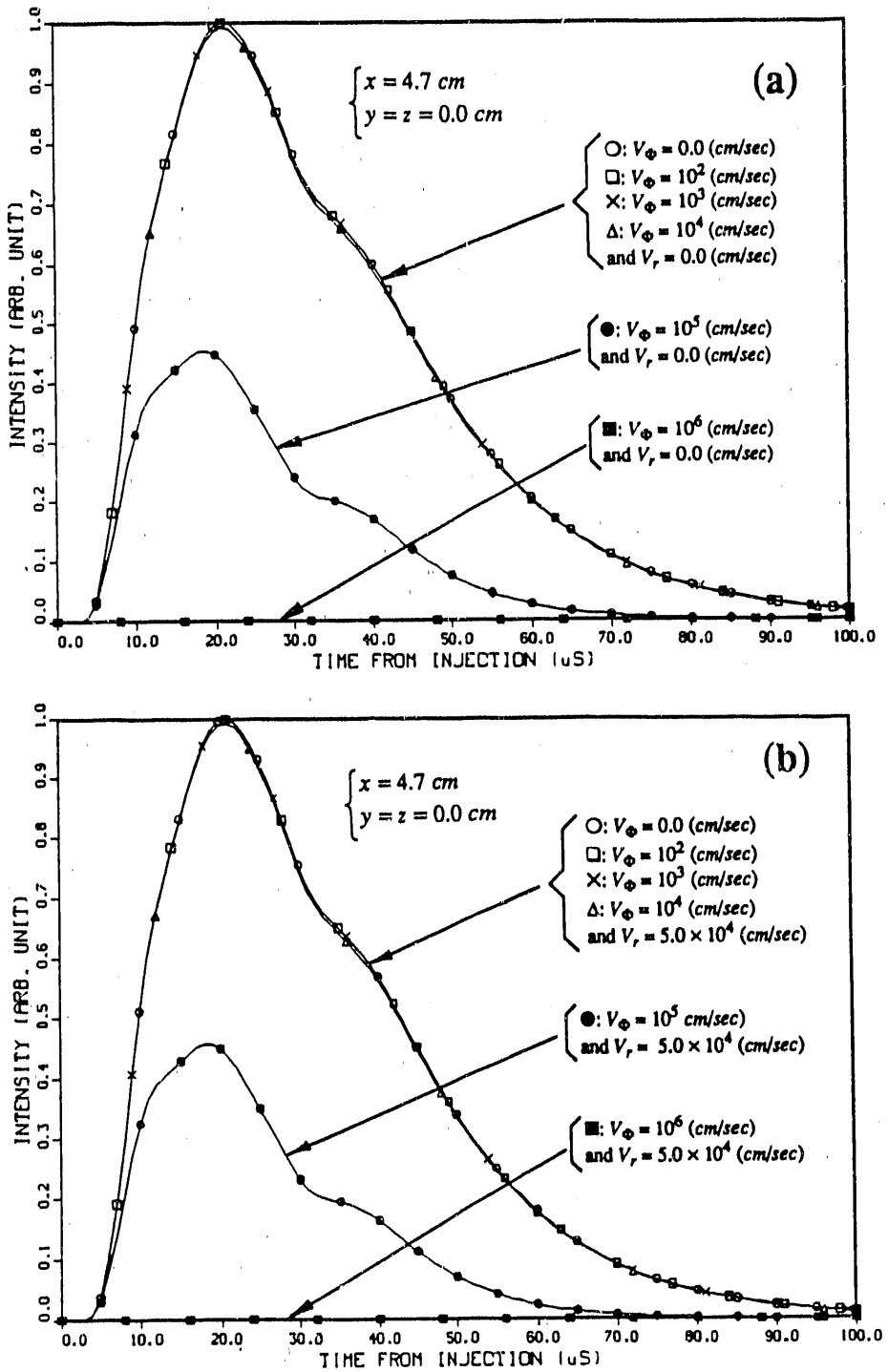

Figure 4.10 The solutions of equation (4.3.8) at x=4.7 (cm) and y=z= 0.0 from five different toroidal convection velocities. The radial convection velocity is (a) zero and (b)500.0(m/sec), respectively .

doesn't measurably affect the diffusion process, and a similar number is also true for the toroidal diffusion. However, when the toroidal convection velocity is 1,000.0 (m/sec), there is an obvious effect on the radial diffusion, quite different from that when there is only a small convection. When the toroidal convective velocity is in the range of 10,000.0 (m/sec), the solution is nearly zero because the convection effect is so strong that almost all of the carbon ions are quickly moved away by the convective flow. Experimentally, we don't observe this phenomena, so the plasma toroidal flow, if it exists, must happen only in the early time of the discharge and should quickly decay to a very small value (lower than 100.0–1,000.0 (m/sec)).

4.4 Error Analysis

In obtaining the diffusion coefficients of carbon ions, several sources of error exist not only in the measurement of the spectral emission from the ions but also in the numerical fitting of the light signal. These errors are discussed below.

(a) The uncertainty in determination the ionization time $\left[\frac{1}{I}\right]$ from C^{+} to C^{++} state. The value of $\left[\frac{1}{I}\right]$ used in the simulation was varied between $20-40$ (μsec). The average duration times for the three pulses in the source discharge are 8.0 (μsec), 16.0 (μsec) and 18.0 (μsec), all shorter than the value of $\left[\frac{1}{I}\right]$. So during the early time of the diffusion process this effect is not strong and only about $40-50$ (μsec) later does the ionization process become more important through the factor e^{-It}. Variation in $\left[\frac{1}{I}\right]$ can occur because of the the uncertainties in the plasma parameters n_e and T_e, and thus $D_{||}$ and $D_{\perp}$ are effected by the ionization rate. For example, when using the formula from the corona model (see section 3.3) or the data for the ionization rate coefficient as shown in Fig.3.8, the uncertainties in n_e and T_e will cause the ionization

time to vary within a certain range; this range becomes larger especially when T_e is lower.

(b) The uncertainty in determination the distance from the carbon probe to the observation point. As we mentioned before, the region of the field of view defines a small volume in a channel due to the magnification of the camera lens and the diameter of the optical fiber. The smaller this volume is, the more accurate the measurement is.

(c) The noise on the light signals, which result either from the photon statistics in the plasma emission or from the PMT noise. This noise introduces uncertainty in the numerical fitting procedure.

Next is an example to illustrate the relationships among these errors, in which we find numerical estimates of the relative errors of the diffusion coefficients. For simplicity, we assume that both the perpendicular and the parallel diffusion coefficients have the same order of relative error, and then the C^+ ion density from the delta function source model can be written as:

$$n_{II} = \frac{N}{8\pi^{3/2}} \frac{e^{-\frac{t}{\tau_{ion.}}}}{D_2^{3/2}\, t^{3/2}} \exp\left[-\frac{x^2+y^2+z^2}{4 D_2 t} \right]$$

$$= n_{II}\,(\,t,\, x,\, ,y,\, z,\, \tau_{ion.},\, D_2\,)\,. \qquad (4.4.1)$$

Since n_{II} is the function of $t, x, y, z, \tau_{ion.}$, and D_2, then the total derivative [31-32] of n_{II} is:

$$\Delta n_{II} = \frac{N}{8\pi^{3/2}} \frac{e^{-\frac{t}{\tau_{ion.}}}}{D_2^{3/2}\, t^{3/2}} \exp\left[-\frac{x^2+y^2+z^2}{4 D_2 t} \right] \times$$

$$\left[\frac{t}{\tau_{ion.}^{\,2}} \Delta\tau_{ion.} - \frac{3}{2}\frac{\Delta D_2}{D_2} - \frac{1}{2 D_2 t}\,(\,x\Delta x + y\Delta y + Z\Delta z\,) \right]. \qquad (4.4.2)$$

Note here we have assumed that $\Delta t = 0$, i.e. the time delay caused by the electronics can be neglected and the time measurement is accurate. The quantities $\Delta\tau_{ion.}$, Δn_{II}, Δx, Δy, and Δz are the uncertainties of the ionization time, the measurement of the light emission from carbon ions, and the spatial resolution of the optical system. It is also assumed that all of these errors are *independent* and *uncorrelated*. ΔD_2 is the uncertainty of the diffusion coefficient resulting from all of the uncertainties discussed above. Equation (4.4.2) can be rewritten as:

$$\frac{\Delta n_{II}}{n_{II}} = \frac{t}{\tau_{ion.}}\Delta\tau_{ion.} - \frac{3}{2}\frac{\Delta D_2}{D_2} - \frac{1}{2D_2 t}(x\Delta x + y\Delta y + Z\Delta z). \qquad (4.4.3)$$

Now we use $\Delta^*\tau_{ion.}$, $\Delta^* n_{II}$, $\Delta^* x$, $\Delta^* y$, $\Delta^* z$, and $\Delta^* D_2$ to denote the *maximum absolute error* of the quantities $\tau_{ion.}$, n_{II}, x, y, z and D_2, respectively, then the *maximum relative error* of the diffusion coefficient can be expressed as:

$$\delta^* D_2 = \frac{\Delta^* D_2}{|D_2|} = \frac{2}{3}\left[\left|\frac{t}{\tau_{ion.}^2}\right|\Delta^*\tau_{ion.} + \frac{\Delta^* n_{II}}{|n_{II}|} + \right.$$

$$\left. \frac{1}{|2D_2 t|}(|x|\Delta^* x + |y|\Delta^* y + |z|\Delta^* z)\right]. \qquad (4.4.4)$$

When taking the measurement along the minor-radial direction, i.e. $y = z = 0$, then equation (4.4.4) is further simplified as:

$$\delta^* D_2 = \frac{\Delta^* D_2}{|D_2|}$$

$$= \frac{2}{3}\left[\left|\frac{t}{\tau_{ion.}^2}\right|\Delta^*\tau_{ion.} + \frac{\Delta^* n_{II}}{|n_{II}|} + \frac{|x|}{|2D_2 t|}\Delta^* x \right]. \qquad (4.4.5)$$

Equation (4.4.5) indicates several issues. First, $\delta^* D_2$ is a function of time. When time t increases, $\delta^* D_2$ increases as $\frac{2}{3}\left|\frac{t}{\tau_{ion.}^2}\right|\Delta^*\tau_{ion.}$ and thus the uncertainty of the ionization time becomes more and more important as time increases. Second, $\frac{\Delta^* n_{II}}{|n_{II}|}$

represents the ratio of noise-to-signal which is also a function of time, and becomes larger since the signal decreases as t increases. Third, $\frac{|x|}{|2D_2 t|}\Delta^* x$ means that the closer to the source, the smaller is the relative error of the measurement. Also, a larger diffusion coefficient results in smaller relative error since the diffusion process is much more dominant than other processes. The contribution $\frac{\Delta^* n_{II}}{|n_{II}|}$ is smaller as either the diffusion coefficient becomes larger or the observation point becomes closer to the source. Finally, equation (4.4.5) indicates that when the maximum absolute error $\Delta^* x$ is fixed, the way to improve the accuracy of the diffusion coefficient measurement is to do the numerical fitting early on, using the signal measured close to the source.

Now we shall put some numerical values into equation (4.4.5). We set $\Delta^*\tau_{ion.} = 20.0$ (μsec) because this is the maximum uncertainty in the numerical fitting, $\Delta^* x = 0.3$ (cm) (this comes from the bench calibration of the lens and optical fiber system), and choose the average characteristic time for the first fitting of each pulse as $t = 10.0$ (μsec), with $\frac{\Delta^* n_{II}}{|n_{II}|} = 10\%$ at this time. If the typical value of D_2 is chosen as $D_2 = 11.5$ (m^2/sec) as the average between $D_{2\|}$ and $D_{2\perp}$, then we have the maximum relative error of the diffusion coefficient obtained at location $x = 1.5$ (cm) is:

$$\delta^* D_2 = \frac{\Delta^* D_2}{|D_2|} = \frac{2}{3}\left[\frac{10\times 20}{30^2} + 0.1 + \frac{0.015\times 0.003}{2\times 11.5\times 10\times 10^{-6}}\right]$$

$$= \frac{2}{3}[\,0.22 + 0.1 + 0.195\,] = 34.3\% \,. \qquad (4.4.6)$$

Thus, in the best case (i.e. at $x = 1.5$ (cm) from the probe) the maximum relative error is about $\pm 34.3\%$, and at $x = 2.5$ (cm) the error is about $\pm 43.1\%$. However, when at $x = 4.7$ (cm), the maximum relative error is about $\pm 100\%$ or higher not only because the observation point is too far away from the source, but also because the ratio of noise-to-signal becomes as high as 100%.

The error analysis for the diffusion coefficient D_3 is difficult, mathematically, because the solution of C^{++} ion density includes a complicated integral (see equation (3.5.15) in Chapter Three). However, both the C^{+} and C^{++} ion densities depend on the ionization time $\tau_{ion.}$, except that in one case this is a positive source while the other is a negative source, so the error caused by the uncertainty of $\tau_{ion.}$ should be the same for D_3 as for D_2. Also, there is a similar noise-to-signal ratio for the measurements of C_{II} and C_{III} light, so it is reasonable to conclude that D_3 has a similar experimental error as D_2.

CHAPTER FIVE
CARBON ION DIFFUSION IN HBT

5.1 Introduction

In this chapter, we start our discussion with a classical transport theory which describes particle diffusion in a cylindrical plasma, giving a simple derivation of the relation between the perpendicular and parallel diffusion coefficients of carbon ions. Then we made a modification to this relation due to the toroidal geometry of the magnetic field, i.e. the neoclassical transport theory. We use these formula to fit the diffusion data obtained in Chapter Four. Bohm diffusion is also discussed as a comparison.

Our impurity transport falls into the Pfirsch-Schluter (or hydrodynamic) regime for low-temperature and high-density plasma, and a MHD treatment is applicable to describe the diffusion process. The reason for using the fluid model is that for this kind of plasma the collision frequency $\left[\frac{1}{\tau_{cp}}\right]$ of impurity ions with plasma ions is large, and the mean free path ($V_{th,c}\,\tau_{cp}$) of the impurity ion is much shorter than the *connection length*, which is the distance between the inside region of good curvature and the outside region of bad curvature of the torus[33]. The connection length is also a characteristic length of the *banana* orbit for a trapped particle which can complete a bounce orbit in less than a collision time. In this regime (i.e. the banana regime), the plasma is collisionless; the particle orbit effect becomes dominant. Kinetic theory should be used in this regime rather than the fluid model. When $V_{th,c}\,\tau_{cp} \leq R_0\,q$, a carbon ion will suffer several collisions with plasma protons before it finishes one banana orbit. So the connection length does provide a basic length scale to distinguish the intrinsic properties of particle transport (see also section 5.3). The criterion for Pfirsch-Schluter region is:

$$V_{th,c}\,\tau_{cp} \le R_0\,q\,, \tag{5.1.1}$$

where $V_{th,c}$ is the thermal velocity of carbon ions, τ_{cp} is the mean collision time between a carbon ion and a plasma proton, R_0 is the major radius of the torus and q is the plasma safety factor. We can also rewrite equation (5.1.1) in the following form:

$$\tau_{cp} \le \frac{R_0\,q}{V_{th,c}} = 1.4\times 10^{-5}\,\frac{q}{\sqrt{T_c\,(eV)}}\quad (sec)\,. \tag{5.1.2}$$

Taking $T_c = 5.0\,(eV)$, $q \simeq 1.5$ for the HBT plasma, then $\tau_{cp} \le 9.4\ (\mu sec)$. From chapter three we know that at $T_c = 5.0\,(eV)$, $\tau_{cp} = 0.4\ (\mu sec)$, which is much smaller than the criterion value. So it is reasonable for us to adopt a fluid equation approach to calculate the transport of carbon ions in the HBT plasma.

5.2 Classical Impurity Diffusion

In our experiment there are three types of particles in the HBT plasma: electrons, protons and carbon ions, with the number density n_e, n_p and n_c, respectively; but the carbon ion density is much smaller than the plasma density, i.e. $n_c \ll n_e \simeq n_p$. According to the relaxation time calculations in Chapter Three, the collisions of carbon ions with electrons can be neglected because of the large mass difference. The self collisions among carbon ions (either C^+ or C^{++} ions) can be ignored too since their densities are very low comparing with plasma density. The principle mechanism which drives the impurity diffusion is the collision between carbon ions and protons. The physical picture is that a small amount of carbon ions (both C^+ and C^{++} ions), which are released from a point source located on the magnetic axis, eventually diffuse through a proton background via the collisions between carbon ions and protons. This is similar to the case of diffusion in a weakly ionized plasma, where the charged particles collide primarily with neutral atoms rather than with one another. The equation of motion for carbon ions can be written as:

$$m_c\, n_c \frac{d\vec{V}_c}{dt} = Z\, e\, n_c\, (\vec{E} + \vec{V}_c \times \vec{B}) - k\, T_c\, \nabla n_c - \vec{R}_{cp}\,, \tag{5.2.1}$$

where m_c is the mass, $\vec{V}_c$ the velocity, Z the charge number and T_c the temperature of carbon ion, respectively. $\vec{E}$ and $\vec{B}$ are the electric and magnetic fields. The term $\vec{R}_{cp}$ is the friction force on the carbon ions due to the collisions with plasma protons, and can be written as $\vec{R}_{cp} = n_c\, m_{cp}\, \nu_{cp}\, (\vec{V}_p - \vec{V}_c)$, where $\nu_{cp} = \frac{1}{\tau_{cp}}$ is the collision frequency between carbon ions and protons, and $m_{cp} = \frac{m_c\, m_p}{m_c + m_p} \approx m_p$ is the reduced mass of carbon ion and proton. Since $|\vec{V}_c| \ll |\vec{V}_p|$ so we have $\vec{R}_{cp} \approx -\, n_c\, m_p\, \nu_{cp}\, \vec{V}_p$. We further assume that the collisions between carbon ions and protons are elastic, then the momentum conservation will be hold and $m_p\, \vec{V}_p = -\, m_c\, \vec{V}_c$ is true for each collision. So the friction term can be approximately expressed as $\vec{R}_{cp} = n_c\, m_c\, \nu_{cp}\, \vec{V}_c$. Here, as an approximation, we consider only the motion of carbon ions and neglect the motion of protons. This is also equivalent to assuming that plasma protons form a uniform scattering background since protons can set up an equilibrium much quickly than carbon ions. The reason for the simplification is that only under these assumptions can a simple formula be derived which describes the relation between perpendicular and parallel diffusion coefficients.

A more rigorous treatment for impurity transport in the minor-radius direction in the Pfirsch-Schluter regime can be found in reference [34]. However, for the transport of carbon ions in HBT plasma, the diffusion along the minor-radial direction is also coupled with the one along the toroidal direction, and this is explained as below.

The diffusion process of carbon ions is governed by the continuity equation:

$$\frac{\partial n_c}{\partial t} + \nabla \cdot \vec{\Gamma}_c = S_c\,, \tag{5.2.2}$$

or,

$$\frac{\partial n_c}{\partial t} + \nabla_\perp \cdot \vec{\Gamma}_{c,\perp} + \nabla_{||} \cdot \vec{\Gamma}_{c,||} = S_c \,, \tag{5.2.3}$$

where $\vec{\Gamma}_c$ and S_c are the flux and source of carbon ions, and perpendicular ($\perp$) and parallel ($||$) are referred to the toroidal magnetic field. Here we have neglected the *Hall* diffusion term which will be explained soon. Since $\vec{\Gamma}_{c,\perp} = -D_\perp \nabla_{c,\perp} n_c$ and $\vec{\Gamma}_{c,||} = -D_{||} \nabla_{c,||} n_c$, where $D_\perp$ and $D_{||}$ are considered to be independent of space and time, then the continuity equation can be written as:

$$\frac{\partial n_c}{\partial t} - S_c = D_\perp \nabla_\perp{}^2 n_c + D_{||} \nabla_{||}{}^2 n_c \,. \tag{5.2.4}$$

For most large present-day tokamaks, the diffusion of impurities along magnetic field lines is much quicker than the diffusion crossing field lines, and the mean free path of the impurity ion is comparable with the major radius, so the term $\nabla_{||}{}^2 n_c$ is zero because there is almost no local accumulation of impurity ions along the toroidal direction. Another reason for $\nabla_{||}{}^2 n_c = 0$ is that for most impurity transport studies the source term is toroidally axisymmetric, i.e. a ring or shell source. Therefore, a 1-D (in the minor-radial direction) model is good enough to describe the inward transport of impurities. However, in our carbon probe experiment, the source is a pulsed point source. Also, the HBT plasma is collisionally dominanted because of its low temperature and high density, and $D_{||}$ is in the almost the same order as $D_\perp$, i.e. the parallel diffusion is stronger than, but comparable with, the perpendicular diffusion. So, $\nabla_{||}{}^2 n_c$ is not zero. Since the source releases a finite amount of carbon ions in each discharge, the density contours of carbon ions will be a set of nested ellipsoids.

Return to equation (5.2.1), and choose the direction of $\vec{B}$ as the $\hat{z}$–axis, and $\hat{x}$– and $\hat{y}$– axes in the plane which is perpendicular to $\vec{B}$. Since the collision frequency ν_{cp} is much larger than the characteristic time change rate $\frac{d}{dt}$, as any macroscopic changes are obtained by many microscopic collisions, the left hand site of (5.2.1) can be set to

zero compared with other terms in the equation. Then (5.2.1) can be reduced to the following component form:

$$n_c\, m_c\, \nu_{cp}\, V_{cx} = Z\, e\, n_c\, E_x - k\, T_c \frac{\partial n_c}{\partial x} + Z\, e\, n_c\, B\, V_{cy}\,, \tag{5.2.5}$$

$$n_c\, m_c\, \nu_{cp}\, V_{cy} = Z\, e\, n_c\, E_y - k\, T_c \frac{\partial n_c}{\partial y} - Z\, e\, n_c\, B\, V_{cx}\,, \tag{5.2.6}$$

$$n_c\, m_c\, \nu_{cp}\, V_{cz} = Z\, e\, n_c\, E_z - k\, T_c \frac{\partial n_c}{\partial x}\,. \tag{5.2.7}$$

Define the *parallel mobility*, $\mu_{\|}$, and the *parallel diffusion coefficient*, $D_{\|}$, of carbon ions as follows:

$$\mu_{\|} = \frac{|Z\, e|}{m_c\, \nu_{cp}}\,, \tag{5.2.8}$$

and

$$D_{\|} = \frac{k\, T_c}{m_c\, \nu_{cp}}\,, \tag{5.2.9}$$

then (5.2.5)-(5.2.7) can be rewritten as:

$$[\,1 + (\,\Omega_c\, \tau_{cp}\,)^2\,]\, V_{cx} = \mu_{\|}\, E_x - \frac{D_{\|}}{n_c} \frac{\partial n_c}{\partial x} + (\,\Omega_c\, \tau_{cp}\,)^2 \frac{E_y}{B} - (\,\Omega_c\, \tau_{cp}\,)^2 \frac{k\, T_c}{Z\, e\, B} \frac{1}{n_c} \frac{\partial n_c}{\partial y}\,, \tag{5.2.10}$$

$$[\,1 + (\,\Omega_c\, \tau_{cp}\,)^2\,]\, V_{cy} = \mu_{\|}\, E_y - \frac{D_{\|}}{n_c} \frac{\partial n_c}{\partial y} - (\,\Omega_c\, \tau_{cp}\,)^2 \frac{E_x}{B} + (\,\Omega_c\, \tau_{cp}\,)^2 \frac{k\, T_c}{Z\, e\, B} \frac{1}{n_c} \frac{\partial n_c}{\partial x}\,, \tag{5.2.11}$$

$$V_{cz} = \mu_{\|}\, E_z - \frac{D_{\|}}{n_c} \frac{\partial n_c}{\partial z}\,. \tag{5.2.12}$$

Where $\Omega_c = \dfrac{|Z\, e|B}{m_c}$ is the gyrofrequency of carbon ions. We further define the *perpen-*

dicular mobility, $\mu_\perp$, the *Hall mobility*, μ_H, the *perpendicular diffusion coefficient*, $D_\perp$, and the *Hall diffusion coefficient*, D_H, of carbon ions as follows:

$$\mu_\perp = \frac{\mu_\parallel}{1 + (\Omega_c \tau_{cp})^2}, \tag{5.2.13}$$

$$\mu_H = \frac{\mu_\parallel (\Omega_c \tau_{cp})}{1 + (\Omega_c \tau_{cp})^2}, \tag{5.2.14}$$

$$D_\perp = \frac{D_\parallel}{1 + (\Omega_c \tau_{cp})^2}, \tag{5.2.15}$$

and

$$D_H = \frac{D_\parallel (\Omega_c \tau_{cp})}{1 + (\Omega_c \tau_{cp})^2}, \tag{5.2.16}$$

then equations (5.2.10)-(5.2.12) can be written in the following vector form of the flux of carbon ions, driven either by the electric field:

$$\begin{bmatrix} \Gamma_{cx} \\ \Gamma_{cy} \\ \Gamma_{cz} \end{bmatrix} = n_c \begin{bmatrix} V_{cx} \\ V_{cy} \\ V_{cz} \end{bmatrix} = n_c \begin{bmatrix} \mu_\perp & \mu_H & 0 \\ -\mu_H & \mu_\perp & 0 \\ 0 & 0 & \mu_\parallel \end{bmatrix} \begin{bmatrix} E_x \\ E_y \\ E_z \end{bmatrix}, \tag{5.2.17}$$

i.e.:

$$\vec{\Gamma}_c = n_c \vec{V} = n_c \overleftrightarrow{\mu} \cdot \vec{E}, \tag{5.2.18}$$

or by the number density gradient of carbon ions themselves:

$$\begin{bmatrix} \Gamma_{cx} \\ \Gamma_{cy} \\ \Gamma_{cz} \end{bmatrix} = n_c \begin{bmatrix} V_{cx} \\ V_{cy} \\ V_{cz} \end{bmatrix} = -n_c \begin{bmatrix} D_\perp & D_H & 0 \\ -D_H & D_\perp & 0 \\ 0 & 0 & D_\parallel \end{bmatrix} \begin{bmatrix} \nabla_x n_c \\ \nabla_y n_c \\ \nabla_z n_c \end{bmatrix}, \tag{5.2.19}$$

i.e.:

$$\vec{\Gamma}_c = n_c \vec{V} = -n_c \overleftrightarrow{D} \cdot \nabla n_c . \tag{5.2.20}$$

Where $\overleftrightarrow{\mu}$ and $\overleftrightarrow{D}$ are the *mobility* and *diffusion coefficient tensors*, respectively.

The only off-diagonal element in $\overleftrightarrow{D}$ is the *Hall* diffusion coefficient, D_H, which is

smaller than the transverse diffusion coefficient $D_\perp$, since $D_H \approx (\Omega_c \tau_{cp}) D_\perp$ when $(\Omega_c \tau_{cp}) \ll 1$, $D_H \approx \frac{D_\perp}{2}$ when $(\Omega_c \tau_{cp}) \approx 1$, and $D_H \approx \frac{D_\perp}{(\Omega_c \tau_{cp})}$ when $(\Omega_c \tau_{cp}) \gg 1$. The *Hall* diffusion is in the direction perpendicular to both $\vec{B}$ and ∇n_c. Since the carbon probe is a point source, then the *Hall* diffusion can happen in any radial direction from the source on the plane which is perpendicular to the toroidal magnetic field.

Equations (5.2.10) and (5.2.11) can be combined into the vector form:

$$\vec{V}_{c,\perp} = \mu_\perp \vec{E}_\perp - D_\perp \frac{\nabla_\perp n_c}{n_c} + \frac{(\Omega_c \tau_{cp})^2}{1+(\Omega_c \tau_{cp})^2} (\vec{V}_{c,E} + \vec{V}_{c,D}) . \qquad (5.2.21)$$

Where $\vec{V}_{c,E}$ and $\vec{V}_{c,D}$ are the $\vec{E} \times \vec{B}$ and *diamagnetic drifts* of carbon ions, respectively, defined as:

$$\vec{V}_{c,E} = \frac{\vec{E} \times \vec{B}}{B^2} , \qquad (5.2.22)$$

and

$$\vec{V}_{c,D} = - \frac{k T_c \nabla n_c \times \vec{B}}{Z_c e n_c B^2} . \qquad (5.2.23)$$

Note in equation (5.2.23) we have assumed that T_c is independent of the space coordinate.

In equation (5.2.21), the first term $\mu_\perp \vec{E}_\perp$ is the drift velocity of the carbon ion driven by the perpendicular electric field, which can be estimated as $k T_c / a e$ where a is the plasma minor radius. Since

$$|\mu_\perp \vec{E}_\perp| = \frac{\mu_\parallel}{1+(\Omega_c \tau_{cp})^2} E_\perp \approx \frac{\mu_\perp}{2} E_\perp$$

$$= \left[\frac{Z_c e}{m_c \nu_{cp}} \right] \left[\frac{k T_c}{a e} \right] = \frac{Z_c k T_c \tau_{cp}}{m_c} ,$$

we get the numerical formula as:

$$|\mu_\perp \vec{E}_\perp| = 4.02 \times 10^6 \, Z_c \, T_c \, (eV) \, \tau_{cp} \, (sec) \quad (m/sec) \, . \tag{5.2.24}$$

Note here we have assumed that $(\Omega_c \tau_{cp})^2 \sim 1$. If $(\Omega_c \tau_{cp})^2 > 1$, $|\mu_\perp \vec{E}_\perp|$ will be smaller than the value from (5.2.21). For $Z_c = 1$, $T_c = 5$ (eV), since $\tau_{cp} = 0.5$ (μsec), we $|\mu_\perp \vec{E}_\perp| = 2.0$ (m/sec).

The second term in (5.2.21), $-D_\perp \dfrac{\nabla_\perp n_c}{n_c}$, is the drift velocity by the density gradient of carbon ions themselves, i.e. the *Fick's law* of diffusion. Since $\dfrac{\nabla_\perp n_c}{n_c} \sim \dfrac{1}{L}$, where L is the density scale length, and $L \approx 0.5$ (cm) is a reasonable estimate for our experiment, we have:

$$\left| -D_\perp \frac{\nabla_\perp n_c}{n_c} \right| \approx \frac{D_\perp}{L} \tag{5.2.25}$$

$$= \frac{5.0 \, (m^2/sec)}{5 \times 10^{-3} \, (m)} = 10^3 \, (m/sec) \, ,$$

which is much larger than $|\mu_\perp \vec{E}_\perp|$; so the drift from the perpendicular electric field can be neglected compared with the diffusion term.

The other two terms in equation (5.2.21), $\vec{V}_{c,E}$ and $\vec{V}_{c,D}$, are the usual $\vec{E} \times \vec{B}$ and diamagnetic drifts perpendicular to the gradients of the electric potential and number density of carbon ions. These two drifts are slowed down by collisions with plasma protons since the drag factor

$$\frac{(\Omega_c \tau_{cp})^2}{1.0 + (\Omega_c \tau_{cp})^2} = \frac{1}{1.0 + \left[\dfrac{\nu_{cp}}{\Omega_c} \right]^2} \to 0$$

when $\nu_{cp} \to \infty$. The $\vec{E} \times \vec{B}$ drift can be calculated using the following formula:

$$|\vec{V}_{c,E}| = \frac{E \, (V/m)}{B \, (T)} \quad (m/sec) \, . \tag{5.2.26}$$

Since $E \approx \left[\frac{k\,T_c}{a\,e} \right] = \frac{5\,eV}{5.0\,(cm)\cdot e} = 100.0\,(V/m)$, then $V_{c,E} = 333.3\,(m/sec)$. Multiplying by the drag factor, the $\vec{E} \times \vec{B}$ drift is about 200.0 (m/sec), which is still smaller than the diffusion velocity term and is therefore neglected. The magnitude of $\vec{V}_{c,D}$ is easily computed from the formula:

$$|\vec{V}_{c,D}| = \frac{k\,T_c\,(eV)}{B\,(T)}\,\frac{1}{L\,(m)}\quad (m/sec)\,. \tag{5.2.27}$$

When we choose $k\,T_c = 5\,(eV)$, $B = 0.3\,(T)$, and $L = 0.5\,(cm)$, then $V_{c,D} = 3.3 \times 10^3\,(m/sec)$, which is larger than the diffusion velocity. However, the "diamagnetic drift" is a term which describes the fluid drift perpendicular to $\nabla\,n_c$ and $\vec{B}$, even though the guiding centers of the carbon ions are stationary. So the diamagnetic drift is not a convective flow and it doesn't actually remove the carbon ions away from the source volume in question.

A similar estimate can be made for equation (5.2.12) which describes the motion of carbon ions along the toroidal magnetic field. Since

$$E_z = \left[\frac{V_{loop}}{2\,\pi\,R} \right] \approx \frac{1.0\,(V)}{2\,\pi \times 0.25\,(m)} = 0.64\,(V/m)\,,$$

i.e. $E_z \ll E_\perp$, and so $\mu_\parallel\,E_z \ll D_\parallel\,\frac{\nabla_\parallel\,n_c}{n_c}$. Therefore, the motion of carbon ions along the magnetic field is also dominated by diffusion rather than a drift from the toroidal electric field.

The product $(\,\Omega_c\,\tau_{cp}\,)^2$ is a very important quantity in the diffusion process of carbon ions. When $(\,\Omega_c\,\tau_{cp}\,)^2 \ll 1$, the magnetic field has little effect on the diffusion since the mean free path of carbon ion is much smaller than its *Larmor* radius. When $(\,\Omega_c\,\tau_{cp}\,)^2 \gg 1$, the magnetic field significantly retards the rate of diffusion across $\vec{B}$ as now the *Larmor* radius is smaller than the mean free path of carbon ion and a collision will happen only after several gyrations.

Next are some numerical formulae for the calculations where the subscripts c and p denote the carbon ion and proton, respectively.

- (a): The Coulomb logarithm for mixed ion-ion collisions[35]:

$$\ln \Lambda_{cp} = \ln \Lambda_{pc}$$
$$= 23 - \ln \left[\frac{Z_c Z_p (\mu_c + \mu_p)}{\mu_c T_p + \mu_p T_c} \left[\frac{n_p Z_c^2}{T_p} + \frac{n_c Z_p^2}{T_c} \right]^{1/2} \right], \qquad (5.2.28)$$

where $\mu_c = \frac{m_c}{m_p} = 12$ and $\mu_p = \frac{m_p}{m_p} = 1$ are the mass of carbon ion and proton expressed in units of proton mass; T_c and T_p are the temperatures, Z_c and Z_p the charge numbers, and n_c and n_p the number densities (cm^{-3}) of carbon ions and protons, respectively. Since $n_c \ll n_p$, and we assume $T_c = T_p$, we have:

$$\ln \Lambda_{cp} \approx 23 - \ln \left[\frac{Z_c^2 \, n_p^{1/2} \, (cm^{-3})}{T_c^{3/2} \, (eV)} \right]. \qquad (5.2.29)$$

The average value of $\ln \Lambda_{cp}$ is about 7–10 for HBT plasma (see Table 3).

Table 3: The Coulomb logarithm $\ln\Lambda_{cp}$ of the carbon ions at different plasma *densities** and *temperatures*†

		4	5	6	7	8	9	10
1.0	$Z_c = 1$	8.96	9.30	9.57	9.80	10.00	10.18	10.34
	$Z_c = 2$	7.58	7.91	8.18	8.41	8.61	8.79	8.95
2.0	$Z_c = 1$	8.61	8.95	9.22	9.45	9.65	9.83	9.99
	$Z_c = 2$	7.23	7.56	7.84	8.07	8.27	8.44	8.60
3.0	$Z_c = 1$	8.41	8.75	9.02	9.25	9.45	9.63	9.79
	$Z_c = 2$	7.03	7.36	7.63	7.87	8.07	8.24	8.40

* The plasma density is $n_e = n_i = 1.0, 2.0$ and 3.0×10^{14} (cm^{-3}).

† The temperature varies as $T_c = T_e = T_i = 4, 5, \ldots, 10$ (eV).

- (b): The gyrofrequency of carbon ion:

$$\Omega_c = 9.58 \times 10^7 \frac{Z_c\, B\ (T)}{A_c} \quad (rad/sec)\,, \tag{5.2.30}$$

where $A_c = 12$ and Z_c are the atomic mass and the charge number of the carbon ion, respectively, and B is the magnetic filed in *Tesla* (T).

- (c): The *Larmor radius* of carbon ion:

Since the thermal velocity of carbon ions on the plane which is perpendicular to $\vec{B}$ is:

$$V_{c,\perp} = \left[\frac{2\,k\,T_c}{m_c}\right]^{1/2} = 4.01 \times 10^3 \sqrt{T_c\ (eV)} \quad (m/sec)\,, \tag{5.2.31}$$

then the *Larmor* radius is:

$$\rho_c = \frac{V_{c,\perp}}{\Omega_c} = \frac{(2\,k\,T_c\,m_c)^{1/2}}{Z_c\,e\,B}$$
$$= 5.0 \times 10^{-4} \frac{\sqrt{T_c\ (eV)}}{Z_c\,B\ (T)} \quad (m)\,. \tag{5.2.32}$$

At $T_c = 5.0\ (eV)$ and $B = 0.3\ (T)$, $\rho_c = 3.7\ (mm)$ for $Z_c = 1$, and $\rho_c = 1.9\ (mm)$ for $Z_c = 2$.

- (d): The collision time of the carbon ion with a proton:

$$\tau_{cp} = 3.91 \times 10^7 \frac{A_c^{1/2}\,T_c^{3/2}\ (eV)}{Z_c^2\,Z_p^2\,n_p\ (cm^{-3})\ \ln \Lambda_{cp}} \quad (sec)\,. \tag{5.2.33}$$

- (e): The mean free path of carbon ion:

$$\lambda_{mfp} = V_{c,th}\,\tau_{cp} = \left[\frac{3\,k\,T_c}{m_c}\right]^{1/2} \tau_{cp}$$
$$= 6.65 \times 10^{11} \frac{T_c^2\ (eV)}{Z_c^2\,n_p\ (cm^{-3})\ \ln \Lambda_{cp}} \quad (m)\,. \tag{5.2.34}$$

At $T_c = 5\ (eV)$ and $n_p = 2 \times 10^{14}\ (cm^{-3})$, $\lambda_{mfp} = 9.2\ (mm)$ for $Z_c = 1$ and $2.3\ (mm)$ for

$Z_c = 2$.

- (f): The $(\Omega_c \tau_{cp})^2$ factor:

$$(\Omega_c \tau_{cp})^2 = 1.4 \times 10^{31} \frac{B^2 (T) T_c^3 (eV)}{Z_c^2 Z_p^4 A_c n_p^2 (cm^{-3}) (\ln \Lambda_{cp})^2} . \qquad (5.2.35)$$

If we write $n_p = N_p \times 10^{14}$ (cm^{-3}) and B in kG, since $A_c = 12$, $Z_p^4 = 1$, then

$$(\Omega_c \tau_{cp})^2 = 1.1667 \frac{B^2 (kG) T_c^3 (ev)}{Z_c^2 N_p^2 (\ln \Lambda_{cp})^2} . \qquad (5.2.36)$$

The value of $(\Omega_c \tau_{cp})^2$ at different plasma densities and temperatures are listed in Table 4 for the case of low magnetic field ($B = 2.0$ (kG)), and in Table 5 for the case of high magnetic field ($B = 3.5$ (kG)). The corresponding value for $Z_c = 2$ is about 1/4 of that for $Z_c = 1$ if we neglect the small variation in $\ln \Lambda_{cp}$. So for the HBT plasma, $(\Omega_c \tau_{cp})^2$ is about 0.2 – 5.4 for the low B-field operation and about 0.5 – 16.6 for the high B-field operation at the plasma density $n_p = 3 \times 10^{14}$ (cm^{-3}).

- (g): The parallel diffusion coefficient:

$$D_{\|} = \frac{1}{3} V_{c,ave}^2 \tau_{cp} = \frac{1}{3} \left[\frac{8 k T_c}{\pi m_c} \right] \tau_{cp} = 0.85 \left[\frac{k T_c}{m_c} \right] \tau_{cp} . \qquad (5.2.37)$$

Where $V_{c,ave}$ is the average velocity of carbon ions assuming a Maxwellian distribution. Using equation (5.2.33) $D_{\|}$ can be numerically expressed as:

$$D_{\|} = 3.2 \times 10^{15} \frac{T_c^{5/2} (eV)}{Z_c^2 Z_p^2 A_c^{1/2} n_p (cm^{-3}) \ln \Lambda_{cp}} \quad (m^2/sec) . \qquad (5.2.38)$$

Since $\sqrt{A_c} = 3.464$, $Z_p^2 = 1$, and also write $n_p = N_p \times 10^{14}$ (cm^{-3}), then (5.2.30) becomes:

$$D_{\|} = 9.24 \frac{T_c^{5/2} (eV)}{Z_c^2 N_p \ln \Lambda_{cp}} \quad (m^2/sec) . \qquad (5.2.39)$$

Table 4: The $(\Omega_c \tau_{cp})^2$ factor of the carbon ions for different plasma densities* and temperatures† at $B_t = 2.0\ (kG)$

		4	5	6	7	8	9	10
1.0	$Z_c = 1$	3.72	6.74	11.01	16.67	23.89	32.83	43.65
	$Z_c = 2$	1.30	2.33	3.77	5.66	8.06	11.01	14.57
2.0	$Z_c = 1$	1.01	1.82	2.96	4.48	6.41	8.80	11.69
	$Z_c = 2$	0.36	0.64	1.02	1.54	2.18	2.98	3.94
3.0	$Z_c = 1$	0.47	0.85	1.38	2.08	2.97	4.08	5.41
	$Z_c = 2$	0.17	0.30	0.48	0.72	1.02	1.39	1.84

Table 5: The $(\Omega_c \tau_{cp})^2$ factor of the carbon ions for different plasma densities* and temperatures† at $B_t = 3.5\ (kG)$

		4	5	6	7	8	9	10
1.0	$Z_c = 1$	11.39	20.66	33.71	51.04	73.18	100.54	133.68
	$Z_c = 2$	3.98	7.14	11.53	17.33	24.68	33.71	44.61
2.0	$Z_c = 1$	3.08	5.58	9.08	13.72	19.64	26.96	35.80
	$Z_c = 2$	1.09	1.95	3.14	4.70	6.69	9.14	12.08
3.0	$Z_c = 1$	1.44	2.59	4.22	6.37	9.10	12.48	16.57
	$Z_c = 2$	0.51	0.92	1.47	2.20	3.12	4.26	5.63

* The plasma density is $n_e = n_i = 1.0$, 2.0 and $3.0 \times 10^{14}\ (cm^{-3})$.

† The temperature varies as $T_c = T_e = T_i = 4, 5, \ldots, 10\ (eV)$.

As $D_{\|}$ depends on Z_c as $\frac{1}{Z_c^2}$, then $D_{2\|} \approx 4.0\, D_{3\|}$ if we neglect the slow variation in $\ln \Lambda_{cp}$.

- (h): The perpendicular diffusion coefficient:

If $(\Omega_c \tau_{cp})^2$ is about unity, then $D_{\perp}$ should be calculated using the equations (5.2.15), (5.2.36) and (5.2.39). However, if $(\Omega_c \tau_{cp})^2 \gg 1$, the following limiting form will be adopted:

$$D_{\perp} = \frac{D_{\|}}{1 + (\Omega_c \tau_{cp})^2} \approx \frac{D_{\|}}{(\Omega_c \tau_{cp})^2} = \frac{\frac{1}{3} V_{c,ave}^2 \tau_{cp}}{\Omega_c^2 \tau_{cp}^2}$$

$$= \frac{\frac{1}{3}\left[\frac{8}{\pi}\frac{k T_c}{m_c}\right]}{\Omega_c^2 \tau_{cp}} \approx \frac{\left[\frac{2 k T_c}{m_c}\right]}{2 \Omega_c^2 \tau_{cp}} = \frac{V_{c,\perp}^2}{2 \Omega_c^2 \tau_{cp}} = \frac{\Omega_c^2 \rho_c^2}{2 \Omega_c^2 \tau_{cp}},$$

i.e.

$$D_{\perp} \approx \frac{\rho_c^2}{2 \tau_{cp}}. \tag{5.2.40}$$

Where $V_{c,\perp} = \left[\frac{2 k T_c}{m_c}\right]^{1/2}$ is the perpendicular (with respect to the magnetic field $\vec{B}$) velocity of carbon ion. Equation (5.2.40) shows that in a strongly magnetized plasma the perpendicular diffusion is a random-walk process with a step length ρ_c, the *Larmor* radius, rather than the mean free path λ_{mfp} of carbon ion, since now $\rho_c \ll \lambda_{mfp}$. More detailed calculations gives the following formula:

$$D_{\perp} = 2.28 \times 10^{-16} \frac{\sqrt{A_c}\, n_p\, (cm^{-3}) \ln \Lambda_{cp}}{B^2\, (T) \sqrt{T_c\, (eV)}} \quad (m^2/sec), \tag{5.2.41}$$

If the magnetic field B is in (kG), and write the plasma density as $n_p = N_p \times 10^{14}\ (cm^{-3})$, then equation (5.2.41) can be expressed as:

$$D_{\perp} = 7.89 \frac{N_p \ln \Lambda_{cp}}{B^2\,(kG)\sqrt{T_c\,(eV)}} \quad (m^2/sec)\,, \tag{5.2.42}$$

An important feature of equation (5.2.41) is that $D_{\perp}$ is independent of Z_c, the charge number of the carbon ions, except for the weak dependence on Z_c in the Coulomb logarithm $\ln \Lambda_{cp}$. This can be explained from equation (5.2.40) since $\rho_c^2 \sim \frac{1}{Z_c^2}$ and $\tau_{cp} \sim \frac{1}{Z_c^2}$. The Z_c-dependence of $D_{\perp}$ is cancelled out when the plasma is strongly magnetized because for higher Z_c carbon ions, which have smaller *Larmor* radius, the collision time between carbon ions and protons is also smaller, resulting in the factor $\frac{\rho_c^2}{\tau_{cp}}$ unchanged. But this is not true for a weakly magnetized plasma since now several collisions between carbon ion and protons can happen during one gyration of a carbon ion. Our carbon probe experiment belongs to this case and the Z_c-dependence is observed.

5.3 Neoclassical Impurity Diffusion

So far, we have discussed the diffusion process of carbon ions only in the simplest configuration of magnetic field, i.e. the $\vec{B}$ field lines are straight and uniform. There are three length scales when we discuss the transport of carbon ions: the connection length $R_0\,q$, the plasma minor radius a and the mean free path of carbon ions λ_{mfp}. The approximation of uniform cylindrical geometry of the magnetic field, discussed in section 4.2, is true as long as $\lambda_{mfp} \ll a$ since now the temporal and spatial variations of the magnetic field and other plasma parameters are slow and small compared with τ_{cp} and λ_{mfp}. In the carbon probe experiment $a = 5.0\ (cm)$ and $\lambda_{mfp} \leq 0.9\ (cm)$ at $T_c = 5.0\ (eV)$ and $n_p = 2.0 \times 10^{14}\ (cm^{-3})$, so $\lambda_{mfp} < a$. However, $\lambda_{mfp} \sim \frac{T_c^2}{n_p}$, which is highly dependent on the temperature of carbon ions; e.g. $\lambda_{mfp} = 4.0\,(cm) \sim a$ if we choose $T_c = 10.0\ (eV)$ and $n_p = 2.0 \times 10^{14}\ (cm^{-3})$. When $\lambda_{mfp} \sim a$, but $\ll R_0\,q$, the non-uniformity

of the magnetic field due to the toroidal geometry can not be neglected because a carbon ion will experience the toroidal effect during a gyration. The modification to the theory discussed in previous section is the so called *neoclassical* transport theory. Since now $\lambda_{mfp} \ll R_0\, q$, a fluid model can be used to describe the transport impurities, and this regime is usually called the *Pfirsch–Schluter* regime. However, for high-temperature and low-density plasmas, $\lambda_{mfp} \sim R_0\, q$, or $\lambda_{mfp} \gg R_0\, q$, the particle orbit effect of impurity ions, which are trapped in the local magnetic mirror along the torus, becomes more and more important for the transport process; these cases are the *plateau* and *banana* regimes[36-40], respectively, and will not be discussed here.

Rutherford[34] calculated the impurity transport in the Pfirsch-Schluter regime in 1974 and pointed out that the classical inward diffusion of high-Z impurity in toroidal plasmas is enhanced by the Pfirsch-Schluter effect. In this regime, the inward flux, according to the 1-D model, can be expressed as:

$$\Gamma_I^{FS} = -\frac{1}{Z_I}\,\Gamma_i = \frac{q^2\,\rho_i^2}{Z_I\,\tau_{i\,I}\,T_i}$$

$$\times\left\{\left[C_1 + \frac{C_2^2}{C_3}\right]\left[\frac{\partial p_i}{\partial r} - \frac{n_i}{n_I\,Z_I}\,\frac{\partial p_I}{\partial r}\right] - \frac{5}{2}\,\frac{C_2}{C_3}\,n_i\,\frac{\partial T_i}{\partial r}\right\}, \qquad (5.3.1)$$

where the subscripts i and I refer to the plasma ions (i.e. the protons) and impurity ions, respectively; $q = \dfrac{r\,B_t}{R\,B_\theta}$ is the safety factor, and $\rho_i = \dfrac{(2\,m_i\,T_i)^{1/2}}{e\,B_t}$ is the *Larmor* radius of the plasma ion. The three coefficients, C_1, C_2 and C_1, are functions of α, defined as $\alpha = \dfrac{n_I\,Z_I^2}{n_i}$,that characterizes the strength of the impurity effects. It is useful to compare α with Z^*, the *Z–effective*[41], defined as $n_e\,Z^* = \sum_s n_s\,Z_s^2$, where the electron density n_e satisfies charge neutrality $n_e = \sum_s n_s\,Z_s$. In our carbon probe experiment, $\alpha \sim 0$ since

$n_I \ll n_i$, $C_1 = 1.00$, $C_2 = 2.21\,\alpha$ and $C_3 = 5.52\,\alpha$; then $\left[C_1 + \frac{C_2^2}{C_3} \right] = 1.00$ and $\frac{C_2}{C_3} \simeq 0.4$. The pressure and temperature profiles of the plasma protons can be approximated as spatially constant because their gradient scales are smaller than that of carbon ions, then equation (5.3.1) can be written as:

$$\Gamma_c^{FS} = -q^2 \frac{\rho_p^2}{\tau_{pc}} \frac{1}{Z_c^2} \left[\frac{T_c}{T_p} \right] \left[\frac{n_p}{n_c} \right] \left[\frac{\partial n_c}{\partial r} \right] . \tag{5.3.2}$$

Note here τ_{pc}, the 90 deflection time of protons by carbon ions, is different from τ_{cp}, the 90 deflection time of carbon ions by protons. According to the theory of collision times discussed in section 3.1, these two different deflection times can be calculated as follows.

• For τ_{pc}:

Since now the test particle is proton and field particle is carbon ion, $x = \frac{w_p}{w_c} = \left[\frac{3}{2} \right]^{1/2} \left[\frac{m_c}{m_p} \right]^{1/2} \left[\frac{T_p}{T_c} \right]^{1/2} \to \infty$ when assuming $T_p = T_c$. Note here we have assumed that the mass of carbon ion is much larger than that of proton; this is true for high-Z impurities. From equation (3.1.27), we have:

$$\tau_{pc} = 1.015 \times 10^7 \frac{A_p^{1/2} T_p^{3/2}}{Z_p^2 Z_c^2 n_c \ln \Lambda_{pc}} .$$

• For τ_{cp}:

Since now the test particle is carbon ion and field particle is proton, $x = \frac{w_c}{w_p} = \left[\frac{3}{2} \right]^{1/2} \left[\frac{m_p}{m_c} \right]^{1/2} \left[\frac{T_c}{T_p} \right]^{1/2} \to 0$ when assuming $T_p = T_c$ and for high-Z impurities. Equation (3.1.23) gives:

$$\tau_{cp} = 1.014 \times 10^7 \frac{A_c\, T_c\, T_p^{1/2}}{Z_c^2\, Z_p^2\, A_p^{1/2}\, n_p \ln \Lambda_{cp}} .$$

The ratio of τ_{pc} to τ_{cp} is:

$$\frac{\tau_{pc}}{\tau_{cp}} = \left[\frac{A_p}{A_c} \right] \left[\frac{T_p}{T_c} \right] \left[\frac{n_p}{n_c} \right] \left[\frac{\ln \Lambda_{cp}}{\ln \Lambda_{pc}} \right] . \tag{5.3.3}$$

Since $\ln \Lambda_{cp} = \ln \Lambda_{pc}$ according to equation (5.2.28), then we have:

$$\tau_{pc} = \left[\frac{m_p}{m_c} \right] \left[\frac{T_p}{T_c} \right] \left[\frac{n_p}{n_c} \right] \tau_{cp} . \tag{5.3.4}$$

As the *Larmor* radius of protons can be expressed as:

$$\rho_p^2 = \frac{2\, m_p\, T_p}{(\, e\, B_t\,)^2} = \left[\frac{2\, m_p\, T_p}{2\, m_c\, T_c} \right] \frac{2\, m_c\, T_c}{(\, Z_c\, e\, B_t\,)^2} Z_c^2$$

$$= \left[\frac{m_p}{m_c} \right] \left[\frac{T_p}{T_c} \right] Z_c^2\, \rho_c^2 , \tag{5.3.5}$$

then the flux of carbon ion in the minor radial direction is:

$$\Gamma_c^{FS} = -\, q^2 \left[\frac{\rho_c^2}{\tau_{cp}} \right] \left[\frac{T_c}{T_p} \right] \left[\frac{\partial\, n_c}{\partial\, r} \right] . \tag{5.3.6}$$

Finally, the collisional radial particle flux of carbon ions can be expressed as[42]:

$$\Gamma_c^{NEO} = \Gamma_c^{cl} + \Gamma_c^{FS} + \Gamma_c^{BP} , \tag{5.3.7}$$

where

$$\Gamma_c^{cl} = -\, \frac{1}{2} \left[\frac{8}{3\, \pi} \right] \left[\frac{\rho_c^2}{\tau_{cp}} \right] \left[\frac{\partial\, n_c}{\partial\, r} \right] \tag{5.3.8}$$

is the *classical* flux driven by the perpendicular component of the friction force $\vec{R}_{cp}$ (see equation (5.2.1)). The flux Γ_c^{FS}, as defined in equation (5.3.6), is the *Pfirsch–Schluter* flux, driven by the poloidal variation of the parallel friction force on a magnetic surface.

The flux Γ_c^{BP} is the long mean-free-path (in the *banana–plateau* regime) contribution to the neoclassical flux, driven by the pressure anisotropy associated with viscous forces; this term is only important for low collisionality and can be neglected in our case. Then equation (5.3.7) becomes:

$$\Gamma_c^{NEO} \approx \Gamma_c^{cl} + \Gamma_c^{FS}$$

$$= -\frac{\rho_c^2}{\tau_{cp}} \left[\frac{1}{2} \left[\frac{8}{3\pi} \right] + q^2 \right] \left[\frac{\partial n_c}{\partial r} \right] . \tag{5.3.9}$$

Comparing with $\Gamma_c^{NEO} = -D_\perp^{NEO} \left[\frac{\partial n_c}{\partial r} \right]$, we have the perpendicular particle diffusion coefficient of carbon ions as:

$$D_\perp^{NEO} = \frac{\rho_c^2}{\tau_{cp}} \left[\frac{1}{2} \left[\frac{8}{3\pi} \right] + q^2 \right] . \tag{5.3.10}$$

Using equations (5.2.32) and (5.2.33), the numerical value of $D_\perp^{NEO}$ is

$$D_\perp^{NEO} = 18.46 \frac{N_p \ln \Lambda_{cp}}{B^2 (kG) \sqrt{T_c (eV)}} (0.42 + q^2) \ (m^2/sec) , \tag{5.3.11}$$

where $n_p = N_p \times 10^{14}$ (cm^{-3}) is the plasma ion density. If we denote the perpendicular diffusion coefficient in (5.2.42) as $D_\perp = D_\perp^{cl}$, then (5.3.11) can be written as:

$$D_\perp^{NEO} = D_\perp^{cl} (0.98 + 2.34 q^2) \ (m^2/sec) . \tag{5.3.12}$$

If we neglect the weak dependence on Z_c in the Coulomb logarithm $\ln \Lambda_{cp}$, $D_\perp^{NEO}$ is also independent of Z_c as well as $D_\perp^{cl}$.

5.4 Bohm Diffusion

So far, the diffusion of carbon ions in the model is due to the binary collisions between carbon ions and plasma ions. However, other mechanism, such as the fluctuation in the density and the electric field of plasma, or some other micro instabilities,

may cause an $\vec{E} \times \vec{B}$ drift for a group of particles; this drift pattern resembles the motion of a *convective cell*[43-44]. The convection will bring about anomalous losses, and this could happen to impurity ions as well as the plasma ions and electrons. As a semiempirical formula, Bohm proposed that diffusion due to the fluctuating $\vec{E}$–field would be:

$$D_{Bohm} = \frac{1}{16} \frac{k\,T_e}{e\,B}, \tag{5.4.1}$$

which is scaled as $\frac{1}{B}$ rather than $\frac{1}{B^2}$. The numerical expression of the Bohm diffusion coefficient is:

$$D_{Bohm} = 0.625 \frac{T_e\,(eV)}{B\,(kG)} \quad (m^2/sec)\,. \tag{5.4.2}$$

The temperature in equation (5.4.2) is the plasma electron temperature. As the thermal equilibration time of carbon ions is very short (< 1.0 (μsec)) compared with the characteristic discharge time of the HBT plasma (~ 200.0 (μsec)), it is reasonable to choose $T_c = T_e$. Then we use $D_{Bohm} = \frac{1}{16} \frac{k\,T_c}{e\,B}$ as the Bohm diffusion coefficient of carbon ions to describe the impurity diffusion process driven by the microscopic fluctuations of an electric field rather than by the Coulomb collisions.

5.5 Discussion of Carbon Ion Diffusion in HBT

The diffusion coefficients obtained under different approximations are summarized below.

- When $\lambda_{mfp} \ll a \ll R_0\,q$:

  For $(\Omega_c\,\tau_{cp})^2 \leq 1$:

$$D_{2\perp} = \frac{D_{2\parallel}}{1 + (\Omega_c\,\tau_{cp})^2} \quad (for\ Z_c = 1)\,, \tag{5.5.1}$$

and

$$D_{3\perp} = \frac{D_{3\parallel}}{1+(\Omega_c\,\tau_{cp})^2} \quad (for\ Z_c = 2)\,, \tag{5.5.2}$$

where the subscripts 2 and 3 refer to $Z_c = 1$ (C^+ ions) and $Z_c = 2$ (C^{++} ions), respectively, and $D_{2\parallel}$ and $D_{3\parallel}$ are given from equation (5.2.39).

For $(\Omega_c\,\tau_{cp})^2 \gg 1$:

$$D_\perp^{cl} = D_{2\perp} \simeq D_{3\perp}\,, \tag{5.5.3}$$

where $D_\perp^{cl}$ is given in equation (5.2.41). Note equation (5.5.3) is independent on Z_c.

- When $\hat{\lambda}_{mfp} \sim a \ll R_0\,q$:

The neoclassical diffusion case, given in equation (5.3.12):

$$D_\perp^{NEO} = D_\perp^{cl}\,(0.98 + 2.34\,q^2)\quad (m^2/sec)\,.$$

Note here $D_\perp^{NEO}$ is also independent on Z_c.

The fill pressure of hydrogen gas is 10 *mTorr* in all of the carbon probe shots. The CO_2 interferometer measurements give the average of line-integrated electron density as $8.0 - 8.5 \times 10^{15}$ (cm^{-2}). Dividing the total length of the optical path inside the vacuum chamber $L = 28.4\,(cm)$, the averaged electron density is about 3.0×10^{14} (cm^{-3}), and the averaged ionization degree is ~ 100% (see also Chapter Six for details). The only uncertainty is the electron temperature since the Thomson scattering system could not be attached to the new vacuum chamber (see Chapter Two for details). Comparing the loop voltages with equivalent runs using the old chamber, the electron temperature would appear to be the same for the plasmas produced in these two different chambers. The electron temperature after 150.0 (μsec), at which the carbon probe was fired, is less than 10 (eV) from the Thomson scattering measurements in the old chamber. Therefore, in the fitting of the data of the diffusion coefficients, we keep the electron density fixed at $n_e = 3.0 \times 10^{14}$ (cm^{-3}), but let the carbon ion temperature T_c (here we have assumed $T_c = T_e$) be varied within a certain range, e.g. $T_c =$

$4.0 - 8.0\ (eV)$.

Fig.5.1 and Fig.5.2 are the fits of $D_{2\perp}$ and $D_{3\perp}$, respectively, according to (5.5.1) and (5.5.2). The best fit for both $D_{2\perp}$ and $D_{3\perp}$ is obtained at the combination of $n_e = 3.0 \times 10^{14}\ (cm^{-3})$ and $T_c = 4.0 - 5.0\ (eV)$. Taking the average of $T_c = 4.5\ (eV)$, then the parallel diffusion coefficients of $D_{2\|}$ and $D_{3\|}$ can be calculated using equation (5.2.39) as:

$$D_{2\|} = 9.24\ \frac{4.5^{5/2}}{1^2 \times 3.0 \times 8.59} = 15.4\ \ (m^2/sec)\ ,$$

and

$$D_{3\|} = 9.24\ \frac{4.5^{5/2}}{2^2 \times 3.0 \times 7.2} = 4.6\ \ (m^2/sec)\ .$$

Comparing with the averaged measurements of $D_{2\|} = 14.0\ (m^2/sec)$ and $D_{3\|} = 4.0\ (m^2/sec)$ (see Fig.4.5), there is about $10 - 15\%$ difference between the measured and calculated values of $D_{2\|}$ and $D_{3\|}$.

In Fig.5.3 and Fig.5.4, the fits are made using the classical and neoclassical diffusion coefficients $D_\perp^{cl}$ and $D_\perp^{NEO}$, respectively. From Fig.5.3, even including the $\pm 34\%$ to $\pm 43\%$ error bar, the fit of $D_\perp^{cl}$ is still not good at the same plasma parameters used in the fit of Fig.5.1 and Fig.5.2, i.e. $n_e = 3.0 \times 10^{14}\ (cm^{-3})$ and $T_c = 4.0 - 5.0\ (eV)$. A better fit can be obtained at $n_e = 1.0 \times 10^{14}\ (cm^{-3})$ and $T_c = 4.0 - 8.0\ (eV)$, but this violates the electron density measurements. This indicates that our HBT plasma is not strongly magnetized since $(\Omega_c\ \tau_{cp})^2$ is in the order of unity. In Fig.5.4, the curves from the neoclassical prediction $D_\perp^{NEO}$ are far away from the measured data at $n_e = 3.0 \times 10^{14}\ (cm^{-3})$ and $T_c = 4.0 - 8.0\ (eV)$. A best fit can be obtained at $n_e = 0.5 \times 10^{14}\ (cm^{-3})$ and $T_c \sim 50.0\ (eV)$, but this not true for the HBT plasma. This means that the enhancement of the carbon ion diffusion due to the Pfirsch-Schluter effect is not observed since now $\lambda_{mfe} \ll a$ and the toroidal effect is not important during each gyra-

tion of the carbon ion.

Also, comparing the fits of Fig.5.1-2 and Fig.5.3-4, the effect of the charge number Z_c is quite obvious; because of the high collisionality of the HBT plasma, the diffusion of the carbon ions is a 2-D problem. Only in a low collisionality of a plasma, can the Z_c-dependence be neglected and the diffusion of impurity ions be treated by a 1-D model.

The Bohm diffusion is plotted in Fig.5.5 as a comparison with the classical and neoclassical diffusion. At the same parameters, i.e. $n_e = 3.0 \times 10^{14}$ (cm^{-3}) (of course D_{Bohm} doesn't depend on n_e or Z_c) and $T_c = 4.0 - 8.0$ (eV), D_{Bohm} is smaller by ~ 5 than the values of $D_{2\perp}, D_{3\perp}, D_{\perp}^{cl}$ and $D_{\perp}^{NEO}$.

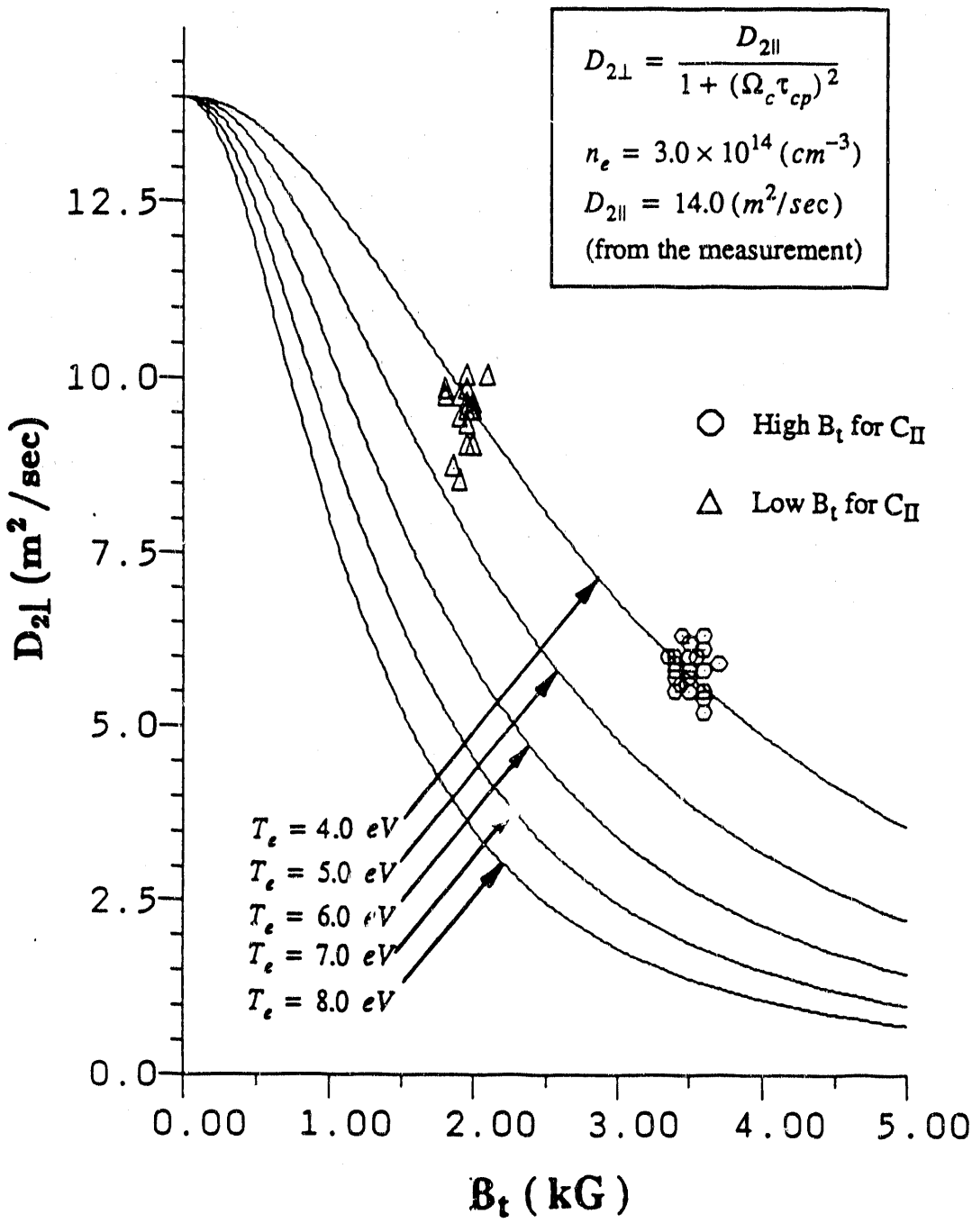

Figure 5.1 The fit of the measured perpendicular diffusion coefficients using the curves predicted by the 2-D classical transport theory for the C^+ ions at $n_e = 3 \times 10^{14}\,(cm^{-3})$ and $T_e = 4 \sim 8\,(eV)$.

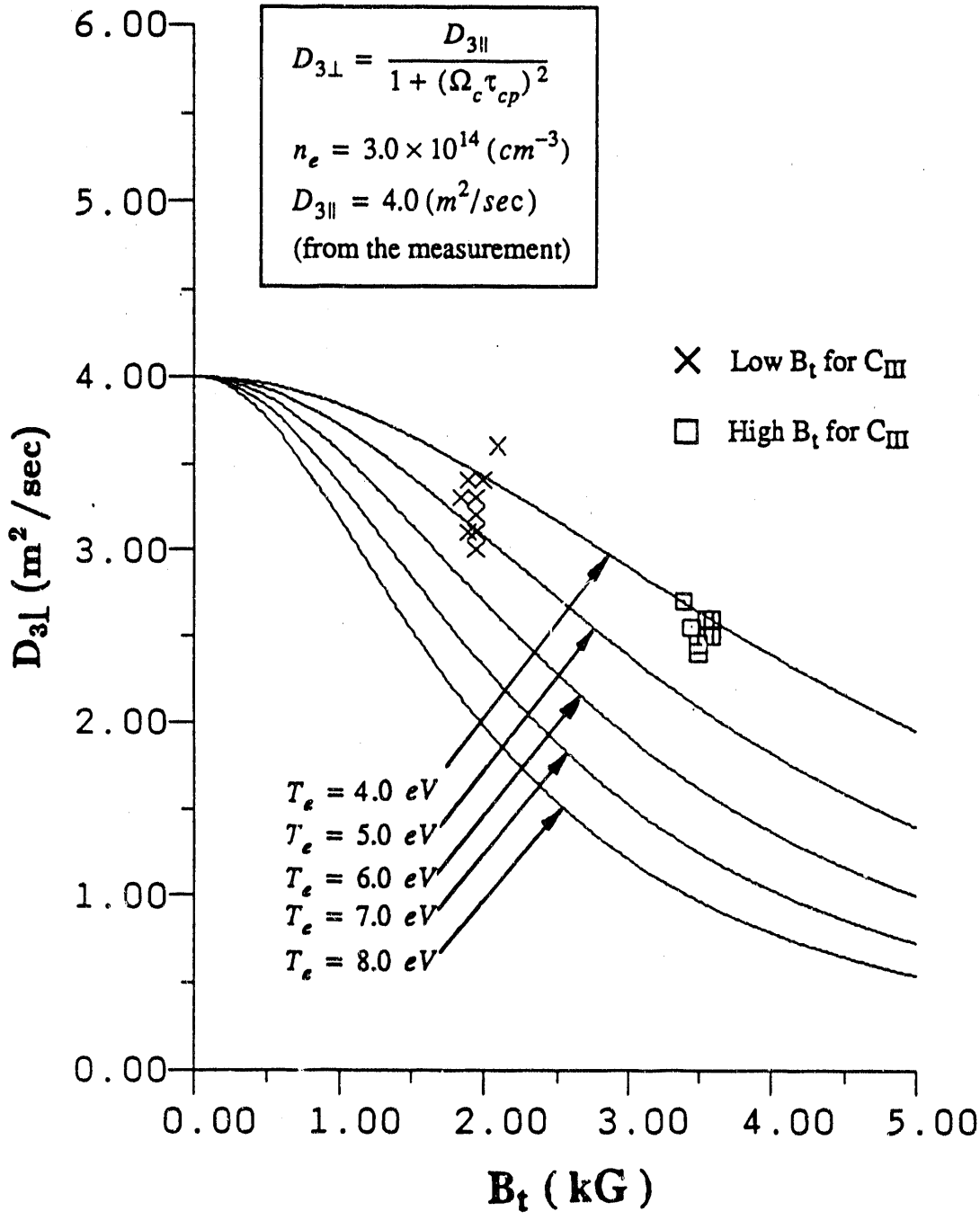

Figure 5.2 The fit of the measured perpendicular diffusion coefficients using the curves predicted by the 2-D classical transport theory for the C^{++} ions at $n_e = 3 \times 10^{14} (cm^{-3})$ and $T_e = 4 \sim 8 (eV)$.

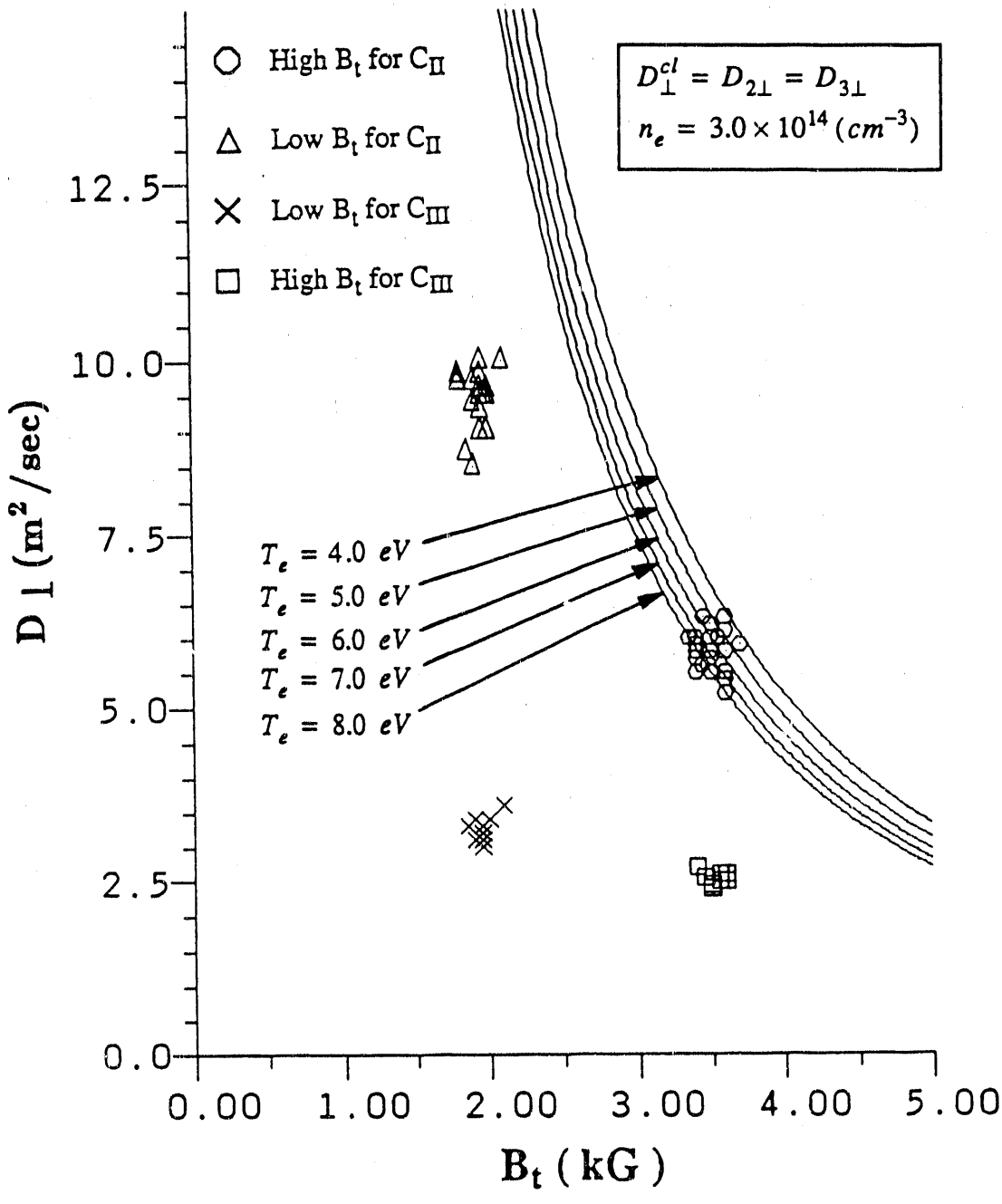

Figure 5.3 The fit of the measured perpendicular diffusion coefficients using the curves predicted by the 1-D classical transport theory for both the $C^+$and C^{++} ions at $n_e = 3 \times 10^{14}$ (cm^{-3}) and $T_e = 4\sim8$ (eV) .

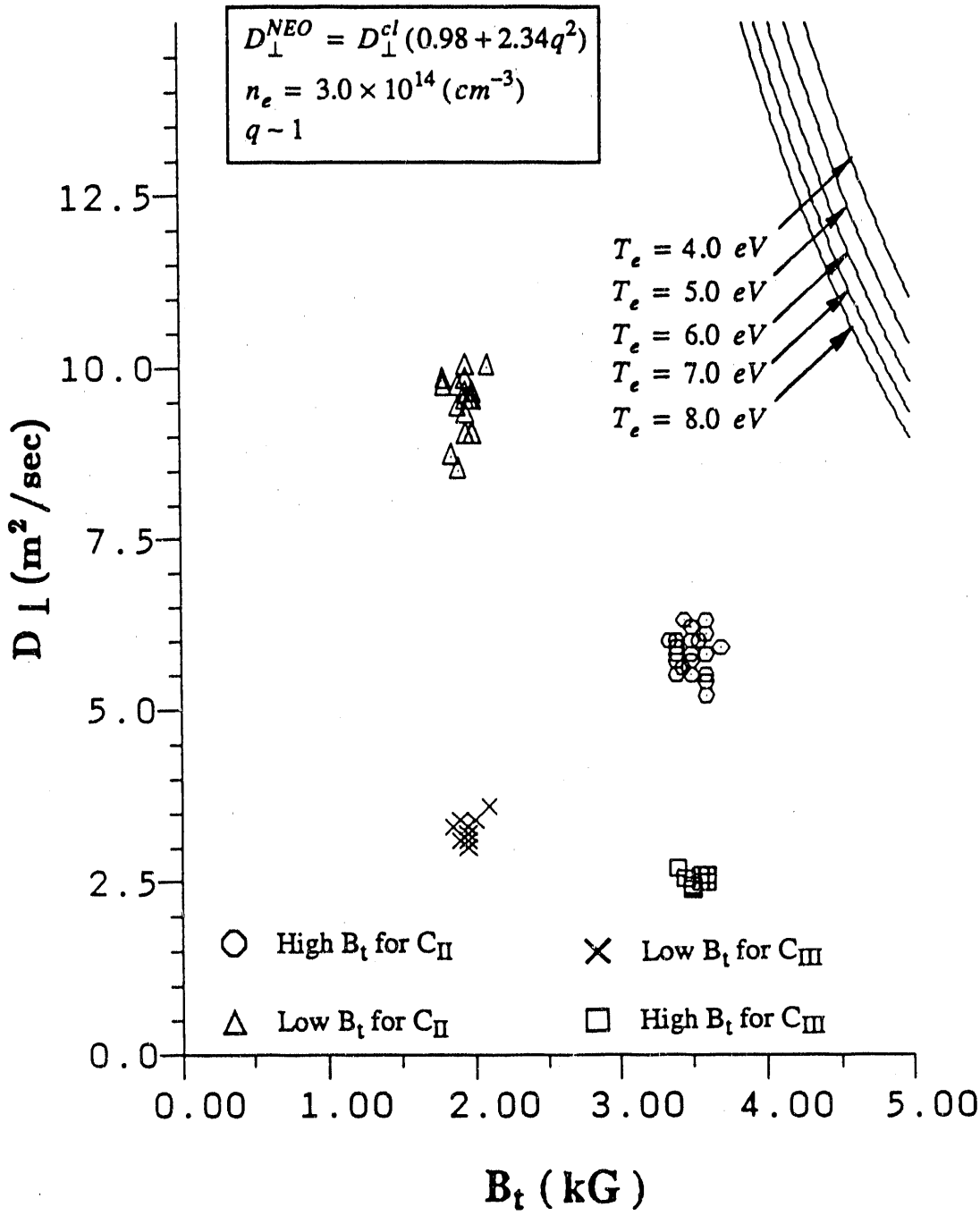

Figure 5 4 The fit of the measured perpendicular diffusion coefficients using the curves predicted by the 1-D neoclassical transport theory for both the $C^+$and C^{++} ions at $n_e = 3 \times 10^{14}\,(cm^{-3})$ and $T_e = 4 \sim 8\,(eV)$.

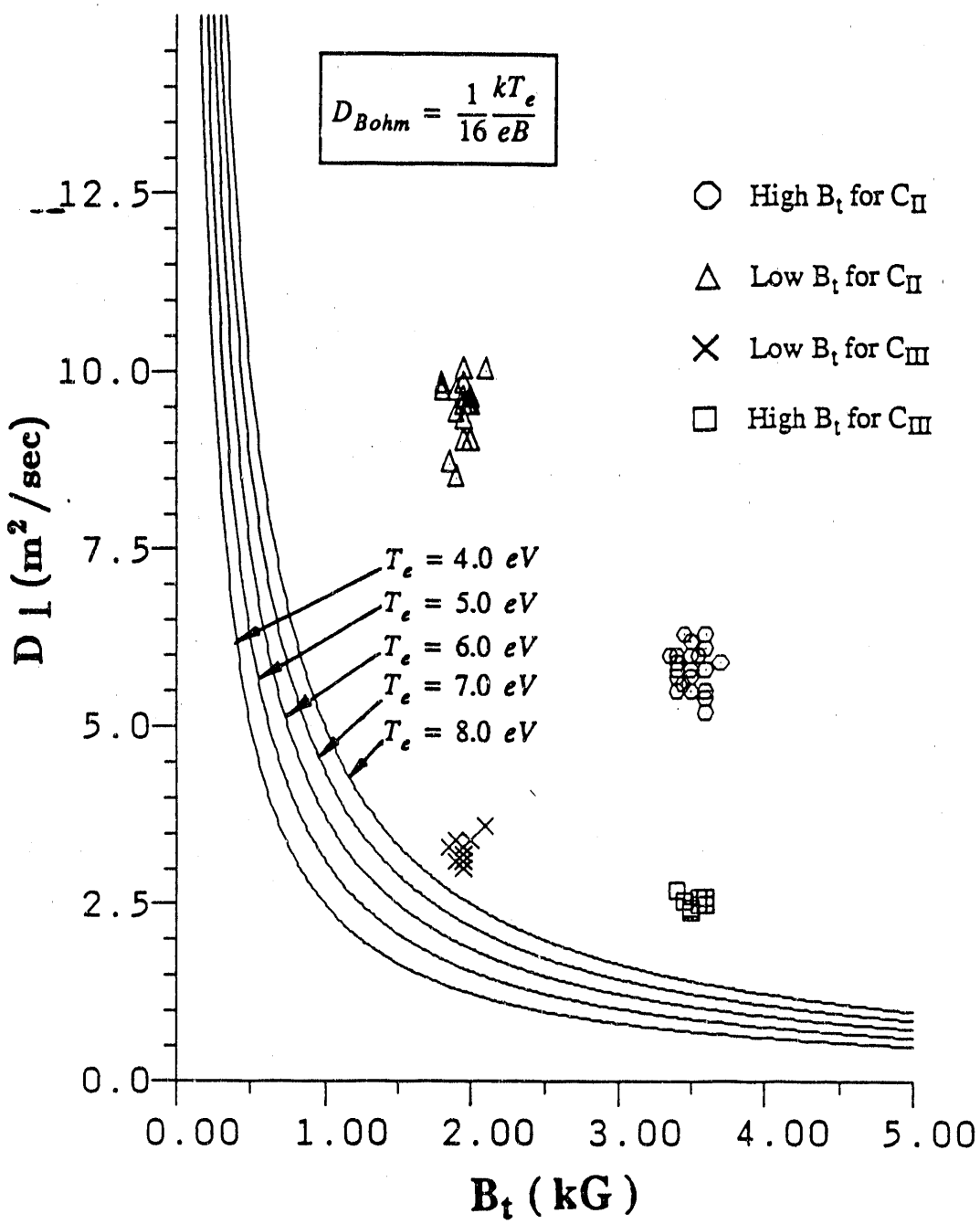

Figure 5.5 The fit of the measured perpendicular diffusion coefficients using the curves predicted by the Bohm diffusion formula for both the $C^+$and C^{++} ions at $n_e = 3 \times 10^{14}\,(cm^{-3})$ and $T_e = 4 \sim 8\,(eV)$.

CHAPTER SIX
H_α LIGHT MEASUREMENT

6.1 Introduction

H_α light (hydrogen Balmer alpha, 6,563 A) measurement plays a very important role in determining the behavior of plasmas in the edge zone, that is, near the wall. In this region neutral hydrogen, either H or H_2, exists and influx of these neutrals along the minor radius can be obtained by the measurement of H_α light emission. The influx can be used to calculate the recycling time of hydrogen between the wall and the plasma which relates to the study of plasma ion losses due to charge exchange with the neutrals. The profile of H_α light emission can also provide a way to obtain the shape (or the cross-section) of the plasma boundary, which should be found in the region where the H_α emissivity is lower than its peak value on the edge.

In this chapter some physics of the production of H_α light is briefly introduced; then the experimental setup and inversion technique are presented, and finally the influx and recycling time for either parallel and reverse bias shots at different fill pressures will be derived.

6.2 H_α Light Production

In the edge region, plasmas are usually characterized by low electron densities ($\leq 10^{13}$ (cm^{-3})) and low temperatures ($\leq 50\,(eV)$), and different molecular effects, such as ionization, charge exchange, excitation and radiative decay, and dissociation, can all influence the particle and energy transport at the edge[45-46]. The entering hydrogen molecules H_2 are mainly lost in three parallel electron-impact reactions:

$$e + H_2 \longrightarrow H^* + H + e \quad (dissociative\ \ excitation) \tag{6.2.1}$$

$$e + H_2 \longrightarrow H^* + H^+ + 2e \quad (dissociative\ \ ionization) \tag{6.2.2}$$

$$e + H_2 \longrightarrow H_2^+ + 2e \qquad (ionization) \qquad (6.2.3)$$

where H^* denotes a product atom which may, or not, be the source of H_α emission. Further electron impact collisions may be needed to form more excited atoms, such as the following reactions

$$e + H_1 \longrightarrow H^* + e \qquad (atomic\ excitation) \qquad (6.2.4)$$
$$e + H_2^+ \longrightarrow H^* + H_1 \qquad (dissociative\ recombination) \qquad (6.2.5)$$
$$e + H_2^+ \longrightarrow H^* + H_1 + e \qquad (dissociative\ excitation) \qquad (6.2.6)$$

Other collisional processes, such as radiative recombination, dissociation of H^{+3} ions, and charge exchange can be neglected because the cross section of these reactions is usually one or two orders lower than the reactions from (6.2.4) to (6.2.6).

The question is to find out the number of H_α photons produced per incoming molecule. More detailed analysis[47] shows that with less than 30% overall error, the composite H_α photon yield per molecule is $f \sim 0.05$ (*photons / molecule*) in the range of electron temperature $T_e = 10 \sim 100\ (eV)$. It should be pointed out that the electron collision times ($\sim 10^{-6}\ (sec)$) for low density plasma are much longer than the characteristic decay times of most excited atomic states, e.g. the lifetime $\approx 10^{-8}\ (sec)$ for $n=3 \rightarrow n=2$ and $\approx 0.16 \times 10^{-8}\ (sec)$ for $n=2 \rightarrow n=1$ according to the oscillator strength. Thus each excited product atom or ion may be taken to be in its ground state at the start of any collisional process.

6.3 Four Channel Optical System

The layout of the four channel optical system, as shown in Fig.6.1, is similar to the single channel system which is discussed in chapter 2. The H_α light emission is also collected by the wide angle Nikkon (f/2.0, 28 (mm)) camera lens and focused on 1–D optical fiber array. Now the sliding rectangular aperture is removed and some The remaining fibers, on which light from different parts of the field of view is imaged, form

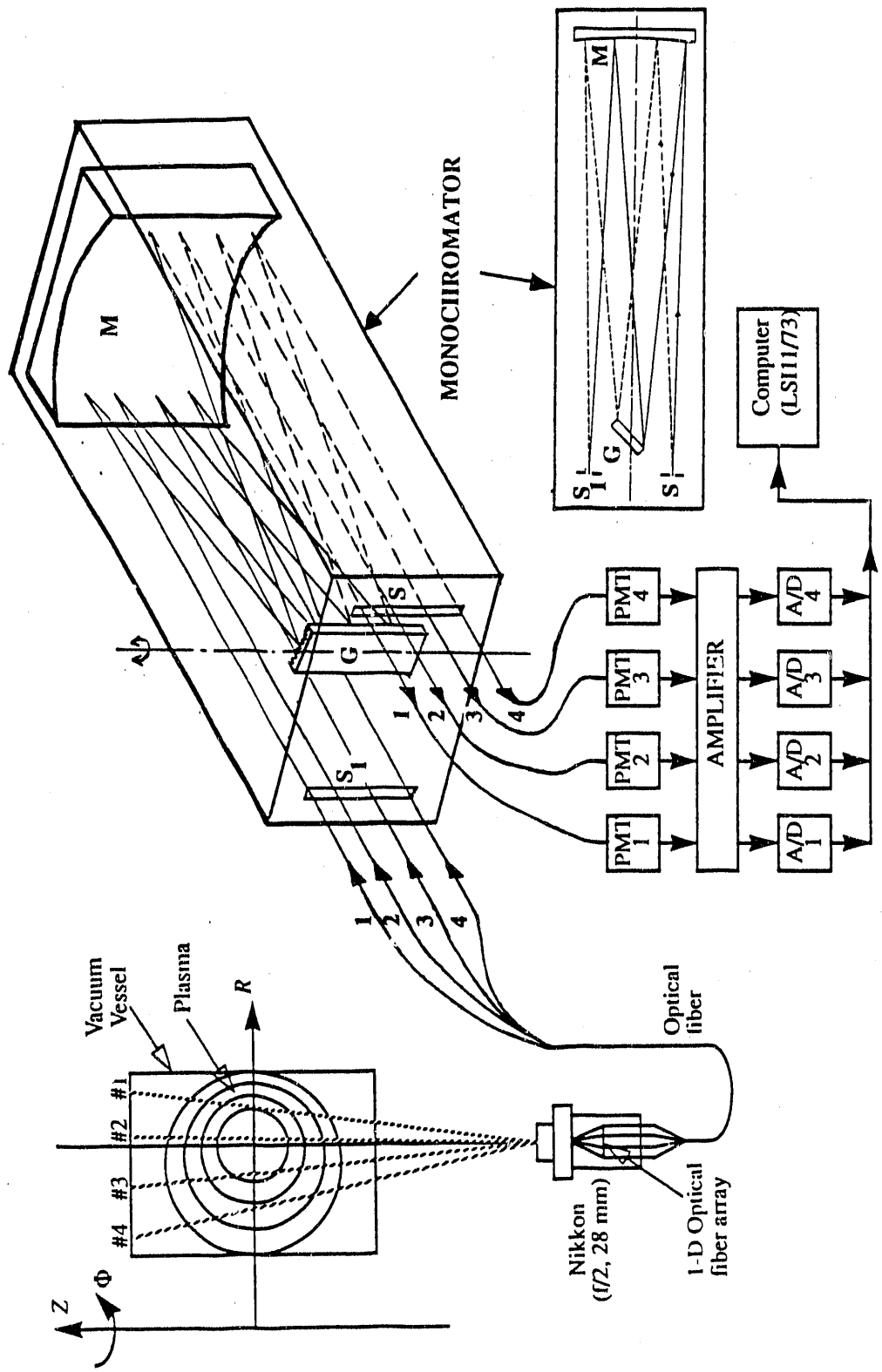

Figure 6.1 The layout of the four channel optical system.

several channels which provide the spatial resolution of the whole plasma volume. The light signals are transmitted to the Jarrel-Ash monochromator (Model 82-000) through long optical fibers (about 10 meters). The bench test shows that up to six channels of light can remain isolated from each other in the monochromator, i.e. the level of cross-talk among these channels can be neglected compared with the signal level[48]. But finally only four channels were used since the first and the last channels were blocked by the opening of the bottom port of the vacuum vessel. The spectral light output from the monochromator was coupled to four photomultiplier tubes (PMT's) through a fan-out structured 1–D optical fiber array, and amplified and recorded by the electronics and computer system.

6.4 Inversion

An inversion is needed to derive the local H_α light emissivity from the chordal spectral measurements. The most commonly used method is Abel inversion.

6.4.1 Abel Inversion

Assume an unknown axisymmetric quantity $\varepsilon(r)$, which is a function of radius r only, is located on the $\hat{z}$-axis in a cylindrical coordinate system. The measurement of $\varepsilon(r)$ in the experiment, see Fig.6.2, is the integrated signal along a chord (say, in the $\hat{x}$-direction) as follows:

$$I(y) = \int \varepsilon \, dx = 2 \int_y^R \frac{r\,\varepsilon(r)\,dr}{\sqrt{r^2 - y^2}} \tag{6.4.1}$$

since $x^2 + y^2 = r^2$ and $d\,x = \frac{r\,dr}{x}$. The integral $I(y)$ is a function of y, the position of a chord along which the integral measurement is taken. Abel inversion[49] gives the following formula for the derivation of $\varepsilon(r)$ according to the chordal integral $I(y)$:

$$\varepsilon(r) = -\frac{1}{\pi} \int_r^R \frac{dI(y)}{dy} \cdot \frac{dy}{\sqrt{y^2 - r^2}} \tag{6.4.2}$$

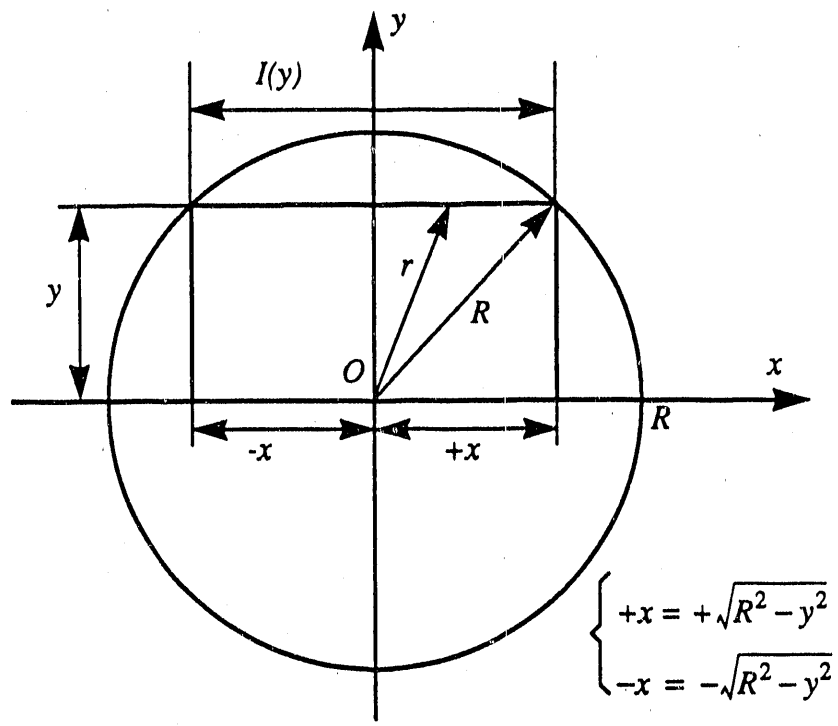

Figure 6.2 The diagram for Abel inversion .

When applying this equation to our experiment several difficulties appear. First it is hard to get the very accurate measurement of the chordal integral $I(y)$ and its first order derivative $\frac{dI(y)}{dy}$ will result in large error. Second, in our experiment, the chords actually used are not parallel but are inclined (see Fig.6.3), and this is not considered in equation (6.4.2). Third, because of the camera lens in the experimental setup, the chordal integral really should be $I(y) = \int \zeta(r, \theta)\, \varepsilon(r)\, dx$ rather than $I(y) = \int \varepsilon(r)\, dx$ as used in equations (6.4.1) and (6.4.2). The quantity $\zeta(r, \theta)$ is the weighting function of the plasma emissivity by the camera lens and describes the optical geometry properties of the lens system. Finally, $\varepsilon(r)$ may not be rigorously axisymmetric in fact, e.g. its contours may be a set of shifted circles. So it is necessary to modify this inversion to overcome these difficulties.

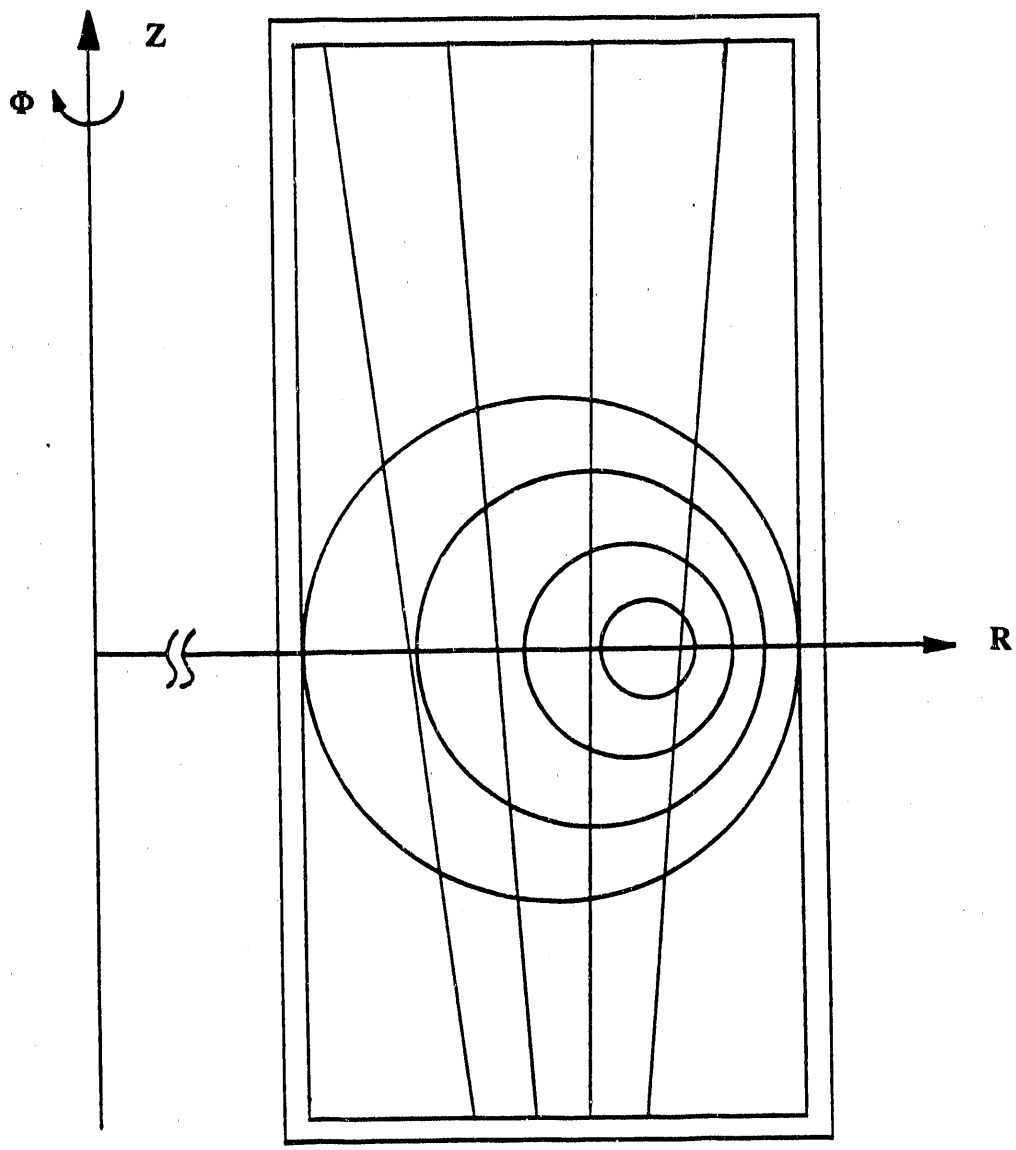

Figure 6.3 The inversion map with scale 1:2.

6.4.2 Improved Abel Inversion

First we assume that the contours of the emissivity are a set of shifted circles which correspond to the magnetic flux surfaces. The internal magnetic probe measurements tell us the cross section of the HBT plasma is almost circular. The real map (with scale 1:2) used in this inversion is shown in Fig.6.3, and the geometry for the improved inversion is shown in Fig.6.4. Since the magnetic center of the plasma is rather stable after the firing of the Maxwell bank, it is reasonable to assume the inversion map (i.e. the zones) is not a function of time. However, it is possible to divide the whole discharge into several temporal sections and use a different inversion map for each section to get more accurate results. The emissivity within each zone is also taken to be the same because the four channel chordal information is not enough to specify the profile over the entire cross section. The emissivities on the top and the bottom parts of the, tall but narrow, vacuum chamber are first assumed to have the same value as that in the outermost zone to satisfy the continuous variation of emissivity, however, later on we will see that the emissivity is very close to zero in this zone.

In order to get a general general expression between the chordal integral signals and the local H_α light emissivity we first define the *signal vector* $\vec{S}_{N\times 1}$ and the *emissivity vector* $\vec{D}_{N\times 1}$ [50-51]. Then the inversion can be expressed as

$$\vec{S}_{N\times 1}(\vec{r}, t) = \overleftrightarrow{A}_{N\times N} \cdot \vec{D}_{N\times 1}(\vec{r}, t) \tag{6.4.3}$$

or in the matrix form as

$$\begin{bmatrix} S_1 \\ S_2 \\ \cdot \\ \cdot \\ \cdot \\ S_N \end{bmatrix} = \begin{bmatrix} a_{11} & a_{12} & \cdots & a_{1n} \\ a_{21} & a_{22} & \cdots & a_{2n} \\ \cdot & \cdot & \cdots & \cdot \\ \cdot & \cdot & \cdots & \cdot \\ \cdot & \cdot & \cdots & \cdot \\ a_{n1} & a_{n2} & \cdots & a_{nn} \end{bmatrix} \begin{bmatrix} D_1 \\ D_2 \\ \cdot \\ \cdot \\ \cdot \\ D_N \end{bmatrix} \tag{6.4.4}$$

where $\overleftrightarrow{A}_{N\times N}$ is the so called *mapping matrix* and N is the number of channels or zones.

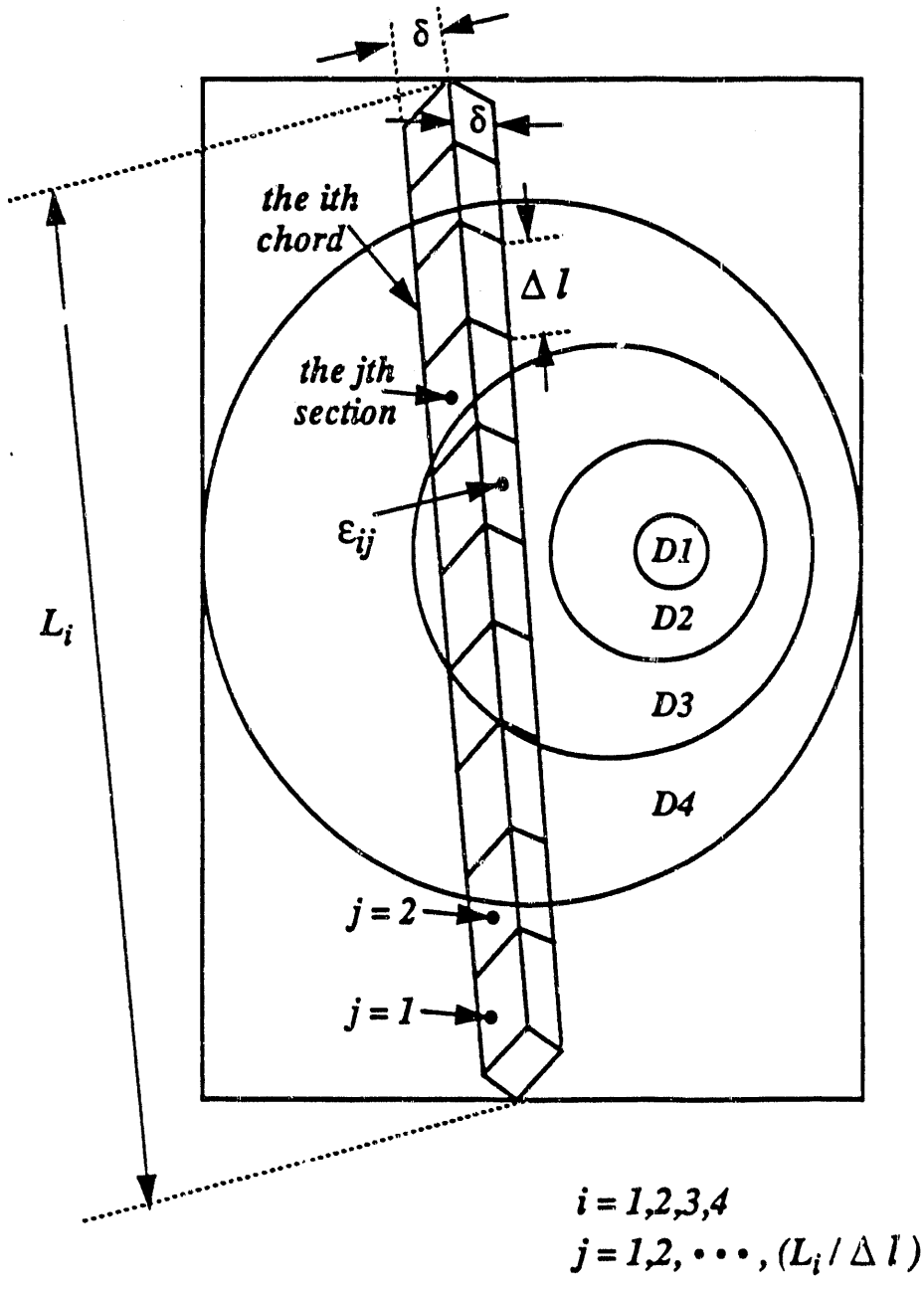

Figure 6.4 The geometry for the improved Abel inversion.

Here both the signal and emissivity vectors are functions of space and time, and the inversion matrix may or may not be the function of time. Then the emissivity vector can be obtained by solving the set of N linear equations:

$$\vec{D}_{N\times 1} = \overleftrightarrow{A}^{-1}_{N\times N} \cdot \vec{S}_{N\times 1} \tag{6.4.5}$$

where $\overleftrightarrow{A}^{-1}_{N\times N}$ is the so called *inversion matrix* which is the inverse of $\overleftrightarrow{A}_{N\times N}$. The number of the zones must be equal to the number of chords to get a unique solution. The numerical method used here is the *Gauss–Seidel* iterative method[52-53]. A sufficient condition for the convergence of the iteration is that the mapping matrix $\overleftrightarrow{A}_{N\times N}$ must be *strictly diagonally dominant*, in the sense that the magnitude of each diagonal element of $\overleftrightarrow{A}_{N\times N}$ is larger than the sum of the magnitudes of all the other elements in the same row, i.e.

$$|a_{ii}| > \sum_{\substack{j=1 \\ j\neq i}}^{n} |a_{ij}| \quad (i, j = 1,2,\ldots,n) \tag{6.4.6}$$

In our experimental arrangement this requirement is satisfied.

Now the question is to find the expression for each element, a_{ij} $(i,j=1,2,\ldots N)$, of matrix $\hat{A}_{N\times N}$. Define the *volume emission rate* of H_α light as:

$$D(\vec{r}, t) = \frac{number\ of\ photons\ (\lambda_0 \rightarrow \lambda_0 + \Delta\lambda)}{cm^3 \cdot second \cdot sr} \tag{6.4.7}$$

where $\lambda_0 = 6{,}563\,A$. Since the Jarrel-Ash Ebert Spectrometer has a 1,200 $(line/mm)$ replica grating which delivers a nominal spectral range of $2{,}000\,A$ to $8{,}000\,A$ with linear reciprocal first order dispersion of $\frac{16\,A}{mm}$ throughout this entire range, then $\Delta\lambda = \frac{16\,A}{mm} \times 259.0\ (\mu m) = 4.7\ (A)$ where $259.0\ (\mu m)$ is the width of the output slit in the monochromator. The dispersive characteristics of the grating spectrometer is that the exit slit allows only a portion of the dispersed spectrum to pass. The amount of light that the monochromator is able to deliver depends on the size of the slit and the solid

angle subtended by the grating at the slit which is going to be discussed in next section. The increased slit width permits a wider spectrum to be transmitted. The background signal level which comes from the continuous spectrum of plasma bremsstrahlung radiation is obtained by mistuning $\pm\, 10\,A$ (since $\Delta\lambda = 4.7\,A$) from $\lambda_{H_\alpha} = 6{,}563\,A$, and is completely negligible compared with the H_α light intensity.

The signal received in the ith channel (or chord) now can be written as:

$$S_i(\vec{r}, t) = \eta_{total} \iiint_{V_i} D(\vec{r}, t)\, d\Omega(\vec{r})\, \zeta(\vec{r})\, dV$$

$$= \frac{number\ of\ photons\ (\lambda_0 \rightarrow \lambda_0 + \Delta\lambda)}{second}. \tag{6.4.8}$$

The integral is taken over V_i, the whole volume of the ith chord. The distance between the plasma midplane and the lens ($Z_0 \simeq 33.0\,(cm)$) is much larger than the average transverse dimension of the field of view d; this is estimated as

$$\begin{aligned} d &= transverse\ magnification\ factor\ of\ the\ lens \times d_{fiber} \\ &= 11.0 \times 600.0\ (\mu m) = 0.66\ (cm), \end{aligned} \tag{6.4.9}$$

so the field of view of the chord is considered as a cylinder with the volume $V_i = \frac{1}{4}\pi d^2 L_i$ where L_i is the length of the ith chord.

The solid angle at point $\vec{r}$ in the field of view subtended at the observation point by dS, the aperture area of the camera lens, is $d\Omega(\vec{r}) = \frac{dS}{|\vec{r}|^2}$. Also as $dS \ll |\vec{r}|^2$, so $d\Omega(\vec{r}) \simeq d\Omega_0 = constant$ and calculated as

$$d\Omega_0 = \frac{dS}{Z_0^2} = \frac{1.54\ (cm)^2}{[\,33.0\ (cm)\,]^2} = 1.41 \times 10^{-3}\ (sr) \tag{6.4.10}$$

The quantity η_{total} indicates the total transmissive coefficient of the optical system which is much less than unity and dependent on the total loss in the system. η_{total} will

be discussed in detail in next section. The weighting function $\zeta(\vec{r})$ is measured in the following way: we move a light source along each chord and measure the output signal level from a PMT every $\Delta l = 1.0\ (cm)$. Since the output signal is small and somewhat contaminated by the noise from PMT the *lock–in* (or *phase–sensitive*) detection technique is used[54]. The weight factor at each point is obtained by normalizing the signal level reading to the maximum signal level reading of the whole measurements. Finally $\zeta(\vec{r})$ is re-normalized to unity. Note that if the lens is replaced by a collimator $\zeta(\vec{r})$ will be unity everywhere.

The whole volume of each chord is divided into 29 ~ 30 sections, depending on its location, with the volume

$$\begin{aligned}\Delta V &= \frac{1}{4}\pi d^2 \Delta l \\ &= \frac{1}{\pi} 3.14\,(0.66\,cm)^2\,(1.0\,cm)^2 \\ &= 0.342\,(cm)^3\,,\end{aligned} \tag{6.4.11}$$

and the weight factor $\zeta(\vec{r})$ is assigned each section, but differs from section to section.

After these assumptions and discussions, equation (6.4.8) now can be reduced to the following approximate expression:

$$\begin{aligned}S_i(\vec{r}, t) &= \eta_{total}\, d\Omega_0 \iiint_{V_i} D(\vec{r}, t)\,\zeta(\vec{r})\, dV \\ &= \eta_{total}\, d\Omega_0\, \Delta V \sum_{m=1}^{N_i} D_{im}\,\zeta_{im}\end{aligned} \tag{6.4.12}$$

where i is the *chord index* and m is the *section index*. Note here $N_i = \frac{L_i}{\Delta l}$ is the total number of sections in the ith chord and $V_i = N_i\,\Delta V$. The matrices D_{im} and ζ_{im} are the corresponding values of D and ζ in the mth section of the ith chord. Since the emissivity is considered the same in each zone so we get the following identity:

$$\sum_{m=1}^{N_i} D_{im}\,\zeta_{im} = \sum_{j=1}^{N} \left(\sum_{m=1}^{N_{ij}} \zeta_{im} \right) D_j \,, \tag{6.4.13}$$

where D_j is just the emissivity vector as defined before. Note here that N is the total number of zones (or channels, chords) but N_{ij} is the total number of sections in the ith chord occupied by the jth zone, and the term $\sum_{m=1}^{N_{ij}} \zeta_{im}$ denotes the summation of weight factors ζ_{im} over the sections occupied by the jth zone in the ith chord. Now equation (6.4.12) can be written into the following form:

$$S_i(\vec{r}, t) = \sum_{j=1}^{N} \left[\eta_{total}\, d\Omega_0\, \Delta V \sum_{m=1}^{N_{ij}} \zeta_{im} \right] D_j(\vec{r}, t). \tag{6.4.14}$$

Comparing with equation (6.4.4):

$$S_i = a_{ij}\, D_j \,, \tag{6.4.15}$$

finally the general expression of a_{ij}, the element of the mapping matrix, can be written as:

$$a_{ij} = \eta_{total}\, d\Omega_0\, \Delta V \sum_{m=1}^{N_{ij}} \zeta_{im} \,. \tag{6.4.16}$$

6.4.3 Numerical Simulation of the Inversion

Now we shall discuss some numerical values for the inversion. As we know that the quantity η_{total} is the *total transmissive coefficient* of the whole optical system due to the optical loss and can be factored as follows:

$$\eta_{total} = \eta_{i.f.} \times \eta_{plasma} \times \eta_{glass} \times \eta_{lens} \times \eta_{o.f.} \times$$

$$\eta_{f.m.} \times \eta_{mono.} \times \eta_{m.f.} \times \eta_{PMT} \,. \tag{6.4.17}$$

The first factor in the above equation, $\eta_{i.f.} = T^{N_i}$ is the total *Fresnel's reflection loss* due to the optical interfaces of the whole system and calculated using the for-

mula[55]

$$T^{N_t} = \left[1 - \left(\frac{n_t - n_i}{n_t + n_i} \right)^2 \right]^{N_t} = [\, 1 - R \,]^{N_t} \tag{6.4.18}$$

where R and T, depending only on the refractive indices n_t and n_i, are the *reflective* and *transmissive coefficients* for a single interface respectively, and $N_t = 10$ is the total number of interfaces in the whole optical system. Note equation (6.4.18) is symmetric about n_t and n_i and $n_i = 1.0$ is chosen for air. Next are some numerical values of these coefficients for different n_t:

$$\begin{cases} n_t = 1.5 : \; R = 4.0\% \,,\; T = 96.0\% \,,\; T^{N_t} = 66.5\% \,, \\ n_t = 1.6 : \; R = 5.3\% \,,\; T = 94.7\% \,,\; T^{N_t} = 58.0\% \,, \\ n_t = 1.7 : \; R = 6.7\% \,,\; T = 93.3\% \,,\; T^{N_t} = 50.0\% \,, \\ n_t = 1.8 : \; R = 8.2\% \,,\; T = 91.8\% \,,\; T^{N_t} = 42.7\% \,, \\ n_t = 1.9 : \; R = 9.6\% \,,\; T = 90.4\% \,,\; T^{N_t} = 36.3\% \,. \end{cases} \tag{6.4.19}$$

In our inversion the average value of $n_t = 1.8$ is chosen for the optical fibers and camera lens used in the observing system.

The factor η_{plasma} is the transmissive coefficient of plasma and $(1 - \eta_{plasma})$ is the loss of H_α light due to the absorption of plasma itself. However, the plasma is optically thin and absorption can be neglected, so $\eta_{plasma} \approx 100\%$. Similarly, η_{glass} is the transmissive coefficient of the quartz glass in the system, mainly including the glass window on the bottom port of vacuum vessel and the camera lens, and $\eta_{glass} \approx 100\%$ as the dimensions of these pieces of glass are very short compare with the total optical path and also they are highly transmissive.

η_{lens} describes the coupling of light from the camera lens into the optical fiber. The total plane focusing angle of the camera lens when a parallel light beam passing through it is

$$2\,\theta_{lens} = 2\,tg^{-1}\left[\frac{1}{2\,f/\#}\right] = 28^\circ \tag{6.4.20}$$

as for $f/\# = 2.0$. Then the corresponding solid focusing angle is

$$d\Omega_{lens} = \pi\,tg^2\,(\,\theta_{lens}\,) = 0.195\,(\,sr\,)\,. \tag{6.4.21}$$

For optical fiber, the total acceptance angle, $2\,\theta_{o.f.}$, is denoted by the *numerical aperture* which is defined as

$$N.A. = 2\,\theta_{o.f.} = 2\,\sin^{-1}\,(\sqrt{n_1^2 - n_2^2}\,)\;\;(\,rd\,)\,. \tag{6.4.22}$$

As $N.A. = 0.4\,(\,rd\,)$, so $\theta_{o.f.} = 11.5^\circ$ and the solid acceptance angle of the optical fiber is $d\Omega_{lens} = \pi\,tg^2\,(\,11.5^\circ\,) = 0.13\,(\,sr\,)$, and η_{lens} can be estimated as

$$\eta_{lens} \simeq \frac{d\Omega_{o.f.}}{d\Omega_{lens}} = \frac{0.13\,(\,sr\,)}{0.195\,(\,sr\,)} = 66.7\%\,. \tag{6.4.23}$$

The transmission coefficient of optical fiber is given by:

$$\eta_{o.f.} = 10^{-\frac{\alpha x}{10}} \tag{6.4.24}$$

where α is the *attenuation factor* in the unit dB/km and is the function of light wavelength. For $\lambda = 6{,}500\,A$, $\alpha \simeq 10\,(dB/km)$, so for a 10 (*meter*) long optical fiber the transmissive coefficient is

$$\eta_{o.f.} \simeq 10^{-\frac{10\times 0.01}{10}} = 97.7\%\,. \tag{6.4.25}$$

The factors of $\eta_{f.m.}$ and $\eta_{m.f.}$ are the coefficients of light coupling from fiber-to-monochromator and monochromator-to-fiber, respectively. The $f/\#$ of the monochromator is 8.5 so the plane acceptance angle is $\theta_{mono.} = 3.36^\circ$ and the acceptance solid angle is

$$d\Omega_{mono.} = \frac{\pi}{4\,(\,f/\#\,)^2} = 0.011\,(\,sr\,)\,. \tag{6.4.26}$$

First we have $\eta_{m.f.} = 100\%$ because $d\Omega_{mono.} \ll d\Omega_{o.f.}$. Next, since the cross-section area of the optical fiber $\Delta S_{o.f.}$ is larger than the opening area of the input slit ΔS_{slit}, then we have

$$\eta_{f.m.} = \left[\frac{\Delta S_{slit}}{\Delta S_{o.f.}} \right] \times \left[\frac{d\Omega_{mono.}}{d\Omega_{o.f.}} \right]$$

$$= 63.5\% \times 8.36\% = 5.3\% \,. \tag{6.4.27}$$

A big loss exists when light transmitted from the optical fiber into the monochromator, but on the output end the light will be totally collected by the optical fiber.

The internal transmission of a spectral line through the grating spectrometer depends on the reflective coefficients of both the concave mirror and the plane grating. Since they usually have very high reflective coefficients, it is reasonable to set the transmissive coefficient of the monochromator $\eta_{mono.} \approx 100\%$.

The factor η_{PMT} describes the light transmission between the fan-out structured optical fiber and the PMT's. It is a good approximation to set $\eta_{PMT} \approx 100\%$ since the area of the transparent photocathode in the PMT is much larger than the cross-section area of optical fiber and also the end of the fiber is very closely coupled to the photocathode.

Now we can get the total transmission coefficient of the whole system as:

$$\begin{aligned} \eta_{total} &= 42.7\% \times 66.7\% \times 97.7\% \times 98.2\% \times 5.3\% \\ &= 1.45\% \,. \end{aligned} \tag{6.4.28}$$

The element of the inversion matrix $\overleftrightarrow{A}^{-1}_{N\times N}$ is

$$\begin{aligned} a_{ij} &= 1.45\% \times 1.41 \times 10^{-3} \times 0.342 \times \sum_{m=1}^{N_{ij}} \zeta_{im} \\ &= 7.0 \times 10^{-6} \sum_{m=1}^{N_{ij}} \zeta_{im} \,. \end{aligned} \tag{6.4.29}$$

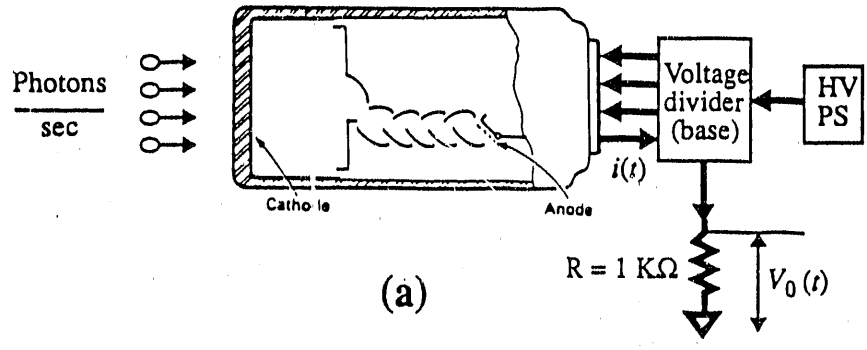

(a)

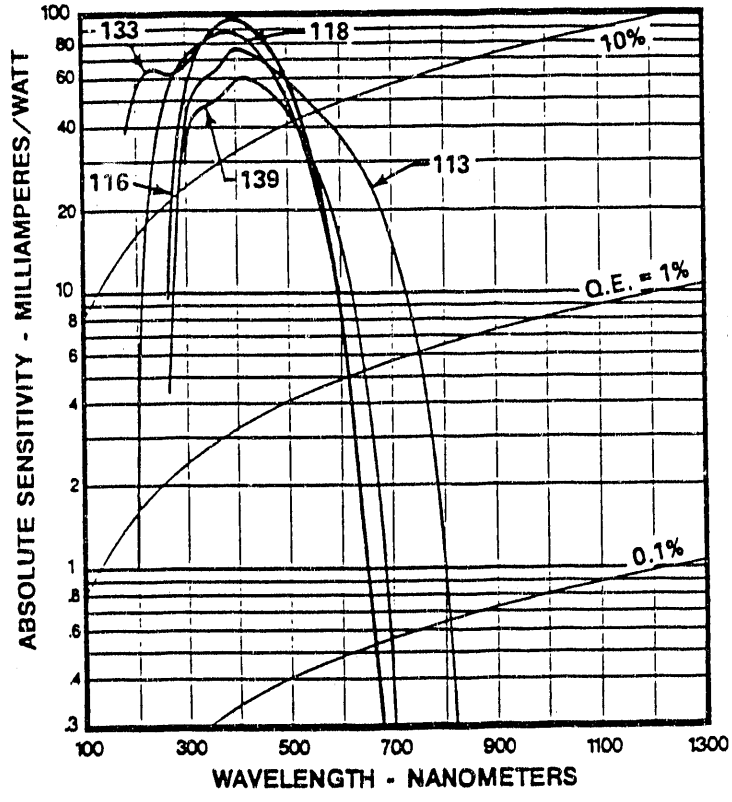

(b)

Figure 6.5 (a)The input photon flux is converted into output voltage by PMT and amplifier; (b)The photocathode spectral response characteristics.

It is useful to write down the dimensional equation of the inversion:

$$S_i \left[\frac{photons}{second} \right] = a_{ij} \, [\, cm^3 \cdot sr \,] \cdot D_j \left[\frac{photons}{cm^3 \cdot second \cdot sr} \right] . \qquad (6.4.30)$$

If we want the volume emission rate in all directions the 4π factor should be applied to the inverted D_j as mentioned above.

The signal measured is the voltage recorded by computer and we need to convert it into the photon flux collected by the PMT's (see Fig.6.5(a)). The *quantum efficiency* of PMT is defined as the average number of photoelectrons emitted from the photocathode per incident photon and can be calculated using the following formula[56]:

$$Q.E. = \frac{\sigma \times 1239.5 \times 100}{\lambda} \, \% \left[\frac{\#\ of\ electrons}{photon} \right] , \qquad (6.4.31)$$

where λ is the wavelength of incident photons in (*nanometers*), and σ is the cathode radiant sensitivity in (A/W). The typical photocathode spectral response characteristics are shown in Fig.6.5(b) and the curve #113 is the one that we used. For λ_{H_α} = 656.3 (nm), $\sigma = 25 \times 10^{-3}$ (A/W) and $Q.E.$ = 4.72% (electrons/photon).

The voltage signal from the A/D converter is

$$V_s = \frac{2\,mV}{count} \times N_c\,(t) \qquad (6.4.32)$$

where $\frac{2\,mV}{count}$ is the sensitivity of *LeCroy*−2256 digitizer and $N_c\,(t)$ is the number of counts. The sampling period used here is 200 (*nanosecond*). Since the termination resistance is $R = 10^3$ (Ω) in the amplifier circuit, the photoelectron current at the anode is

$$i_a\,(t) = \frac{V_s}{R} = 2.0\,N_c\,(t) \times 10^{-6} \quad (A) \qquad (6.4.33)$$

which can be related to the electron flux at the anode by

$$e^- \text{ flux at anode} = \frac{i_a(t)}{e}$$
$$= 1.25 \times 10^{13} N_c(t) \left[\frac{\text{\# of electrons}}{\text{second}} \right]. \qquad (6.4.34)$$

Since the gain of the PMT is $G = 3.5 \times 10^6$ so the electron flux at the cathode is

$$e^- \text{ flux at cathode} = \frac{e^- \text{ flux at anode}}{G}$$
$$= 3.57 \times 10^6 N_c(t) \left[\frac{\text{\# of electrons}}{\text{second}} \right]. \qquad (6.4.35)$$

Finally, the incident photon flux in the ith channel can be obtained by

$$S_i(t) = \frac{e^- \text{ flux at cathode}}{Q.E.}$$
$$= 3.57 \times 10^6 N_c(t) \left[\frac{\text{\# of electrons}}{\text{second}} \right] \times$$
$$\left[\frac{1}{0.0472} \right] \left[\frac{\text{photons}}{\text{\# of electrons}} \right], \qquad (6.4.36)$$

i.e.

$$S_i(t) = 7.57 \times 10^7 N_c(t) \left[\frac{\text{photons}}{\text{second}} \right]. \qquad (6.4.37)$$

6.5 Influxes and Recycling Time of Neutral Hydrogen

The physical model used here is that the plasma is hot and fully ionized in its central region but outside the plasma (i.e. in the region between the plasma and the vacuum vessel) there is cold neutral hydrogen molecule. A boundary layer exists between the plasma and the neutrals. The thickness of this layer can be estimated either by $\lambda_{layer} = v_{H_2} \cdot \tau_{H_2-e}$ where v_{H_2} is the thermal velocity of these cold neutral (which can be assumed to be at room temperature) and τ_{H_2-e} is the mean collision time between hydrogen molecules and plasma electrons, or by the peak region of H_α emissivity which we will find in next section. As the interaction with plasma electrons is the main

mechanism for the loss of H_2, so the hotter the plasma is, the thinner the boundary layer is.

We can give an estimate of the thickness of this boundary layer. According to the collisional data from reference [57], the rate for electron collisions with H_2 which includes all of the possible reactions from (6.2.1) to (6.2.6) by plasma electrons, is $< \sigma v > \approx 6.0 \times 10^{-9}$ (cm^3/sec) at the plasma density $n_e = 3.0 \times 10^{14}$ (cm^{-3}). Since at room temperature ($T_{H_2} = 300°K$), the thermal velocity of H_2 is:

$$v_{H_2} = \left[\frac{3\,k\,T_{H_2}}{m_{H_2}} \right]^{1/2} = 1.93 \times 10^5 \ (cm/sec)\,, \tag{6.5.1}$$

then the mean collision time is:

$$\begin{aligned} \tau_{H_2-e} &\approx \frac{1}{n_e < \sigma v >} \\ &= \frac{1}{10^{14} \times 6 \times 10^{-9}} = 1.67 \ (\mu sec)\,. \end{aligned} \tag{6.5.2}$$

The thickness of the boundary layer is:

$$\begin{aligned} \lambda_{layer} &= v_{H_2} \cdot \tau_{H_2-e} \\ &= 1.93 \times 10^5 \times 1.67 \times 10^{-6} = 0.32 \ (cm)\,, \end{aligned} \tag{6.5.3}$$

which is much smaller than the average plasma radius $a \approx 5.0\ cm$. This is the lowest limit for the thickness of the layer because the constant electron temperature profile is assumed. When we include the effect of temperature gradient at the edge region, then the lower temperature will result in smaller collisional rate and longer collision time, and λ_{layer} will be larger according to equation (6.5.3). As we have only four channels of signal and the width of these zone varies from 1.0 (cm) to 3.0 (cm) (see Fig.6.3), the resolution in this inversion may not be able to precisely find the position of the boundary layer, especially when the layer is just on the interface of two adjacent zones.

Since the plasma can fully absorb and ionize the entering molecules, Γ_r, a one-

dimensional (in the minor-radial direction) local influx of H_2 is defined as follows (see Fig.6.6):

$$\Gamma_r = \frac{number\ of\ H_2\ entering\ into\ plasma}{cm^2 \cdot second}. \tag{6.5.4}$$

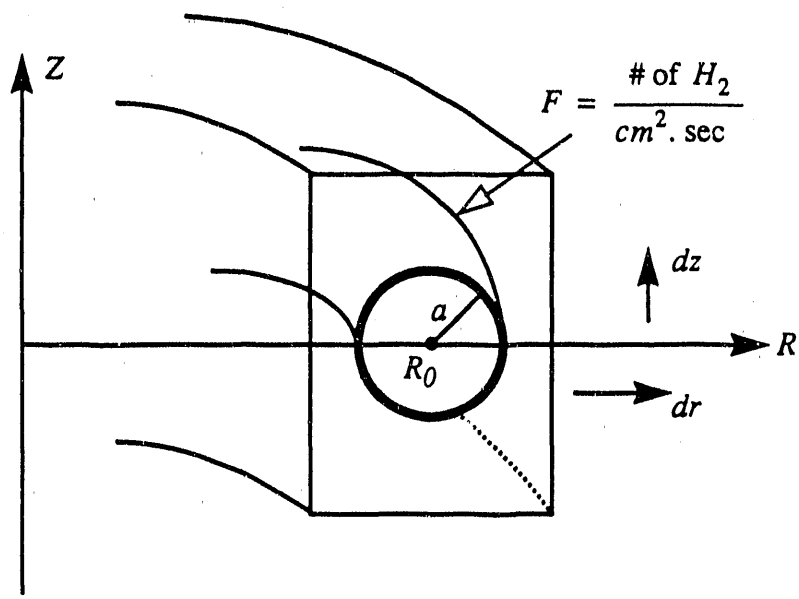

Figure 6.6 The geometry used to calculate the inward minor - radial H_2 flux .

This used to calculate the interchange process of H_2 at the edge region. Compare with the definition of H_α light emissivity:

$$D = \frac{number\ of\ H_\alpha\ photons}{cm^3 \cdot second} \tag{6.5.5}$$

and

$$\frac{D}{f} = \left[\frac{1}{0.05}\right] \frac{number\ of\ H_2}{cm^3 \cdot second}, \tag{6.5.6}$$

where $f = 0.05$ (H_α *photons* / H_2) is the composite H_α yield per hydrogen molecule discussed in section 6.2, the relation between the minor-radial influx of H_2, Γ_r, and the H_α light emissivity, D, now can be expressed as:

$$\Gamma_r = \frac{1}{S} \iiint_{V_p} \frac{D}{f} d^3v \tag{6.5.7}$$

where $S = 2\pi a \cdot 2\pi R_0 = 4\pi^2 a R_0$ is the total surface area of the plasma at the average boundary layer $r = a$ and at the average position $R = R_0$. The integral is taken over V_p, the entire plasma volume.

Since the influx can also be written as $\Gamma_r = n_{H_2} \cdot v_{H_2}$ where n_{H_2} and v_{H_2} are the density and thermal velocity of neutral hydrogen molecules, respectively, then n_{H_2} can be obtained by the following equation:

$$n_{H_2} = \frac{1}{S\, v_{H_2}} \iiint_{V_p} \frac{D}{f} d^3v \tag{6.5.8}$$

From the assumption of toroidal symmetry, the volume integral can be transformed into a surface integral over the plasma cross-section S_c (as shown in Fig.6.6):

$$\iiint_{V_p} \frac{D}{f} d^3v = 2\pi R_0 \iint_{S_c} \frac{D}{f} dR\, dZ\,. \tag{6.5.9}$$

Combing with $S = 4\pi^2 a R_0$, we get:

$$\Gamma_r = \frac{1}{2\pi a f} \iint_{S_c} D\, dR\, dZ\,. \tag{6.5.10}$$

and

$$n_{H_2} = \frac{1}{2\pi a f\, v_{H_2}} \iint_{S_c} D\, dR\, dZ\,. \tag{6.5.11}$$

Since all of the plasma electrons come from the ionization of neutral hydrogen molecules and each H_2 can give *two* electrons when fully ionized, the *effective particle lifetime* or *recycling time* for H_2 in the discharge can be obtained as:

$$\tau_p \approx \frac{V \cdot \bar{n}_e}{2 \cdot \Gamma_r \cdot S} \tag{6.5.12}$$

where $V = 2\,\pi\,R_0\,\pi\,a^2$ is the total volume of the plasma and $\bar{n}_e$ is the volume averaged electron density defined as follows:

$$\bar{n}_e = \frac{1}{V}\iiint_{V_p} n_e\, d^3v\ . \tag{6.5.13}$$

Then τ_p, in *seconds*, is:

$$\tau_p = \frac{a\,\bar{n}_e}{4\,\Gamma_r} = \frac{\pi\,a^2\,f\,\bar{n}_e}{2\iint_{S_c} D\,dR\,dZ}. \tag{6.5.14}$$

6.6 H_α Light Emission in HBT

The H_α light emission in HBT is measured in both parallel bias and reverse bias cases. For each case the inversion is taken and the inward flux of H_2 is calculated. In order to get a general point of view on the emissivity profile some 3–*D* plots at different viewing angle are presented too.

6.6.1 Parallel Bias Case

The four channels of raw data at 10 (*mTorr*) is shown in Fig.6.7(a) and the inverted H_α light emissivity (in 4π solid angle) at four different zones is shown in Fig.6.7(b). In Fig.6.8(a), the inward flux of H_2 is obtained from the cross-sectional integral defined in equation (6.5.10), and Fig.6.8(b) shows the 3–*D* plots of the emissivity profile at two different viewing angles, one from the outside and one from the inside of the plasma.

The line-integrated electron density measurements from the CO_2 interferometer and the plasma current measurement from the Rogowski coil is presented in Fig.6.9(a) and (b) for the parallel bias case. Since there are lots of neutrals in the top and bottom regions of the vessel, the derivation of plasma density in the central region using the total length of the vacuum vessel $L_{vessel} = 28.4\ (cm)$, is only the averaged electron den-

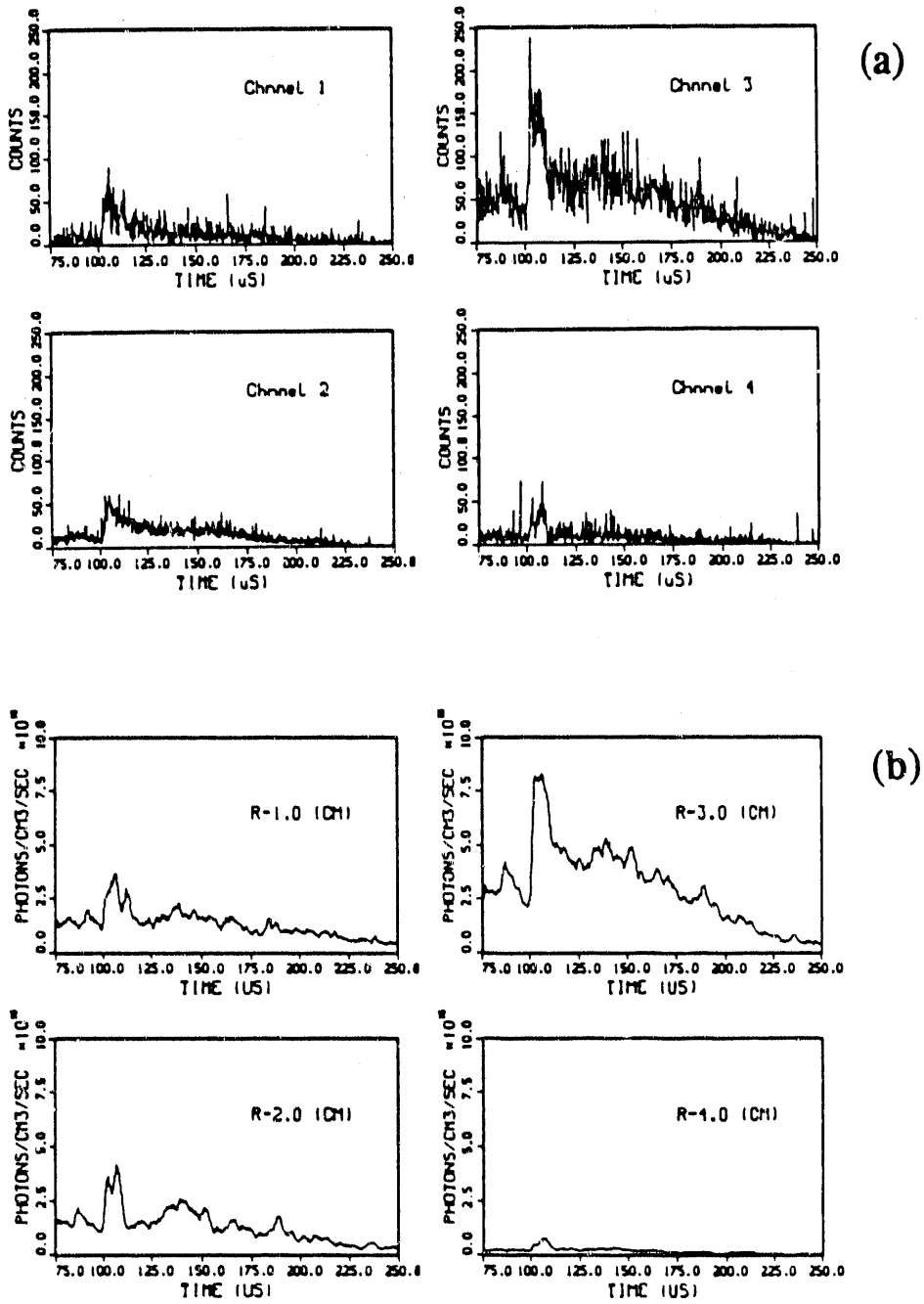

Figure 6.7 (a)The four chordal measurements of H_α light emission; (b)The inverted H_α emissivity in four zones. This is the parallel bias case .

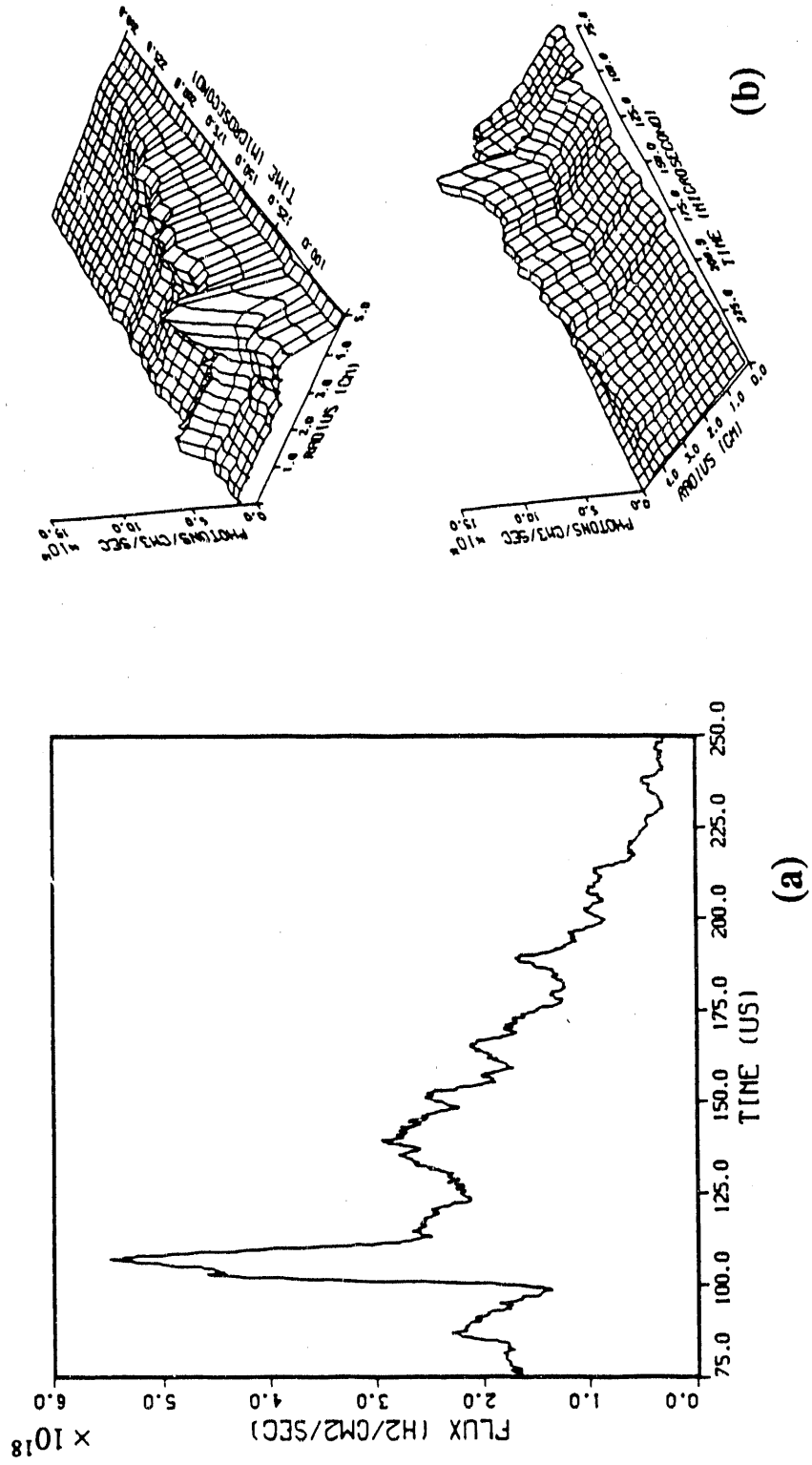

Figure 6.8 (a) The inward minor-radial flux of H_2 molecules; (b)H_α emissivity profile evolution, two different views (parallel bias case) .

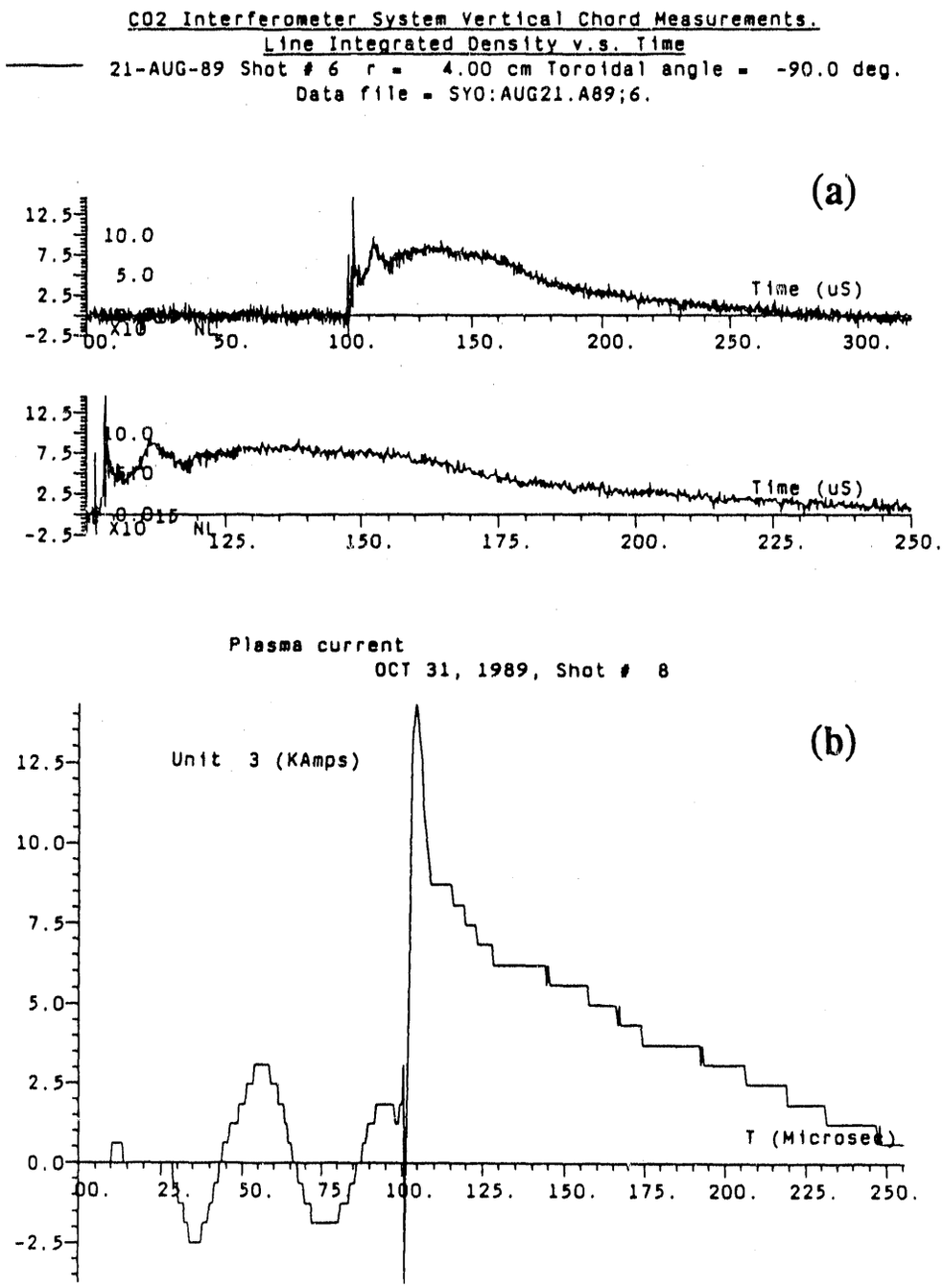

Figure 6.9 (a) The line integrated electron density from the CO_2 interferometer; (b)The total plasma current from the Rogowski coil. Both for parallel bias case at pressure 10 *mTorr*.

sity along the vertical chord of the measurement. As the line integrated electron density is

$$\int n_e \, dl = 8.5 \times 10^{15} \ (cm^{-2}) \ (\ at \ 10 \ mTorr \ ) , \tag{6.6.1}$$

then the averaged electron density is

$$\bar{n}_e = \frac{\int n_e \, dl}{L_{vessel}} = 2.98 \times 10^{14} \ (cm^{-3}) . \tag{6.6.2}$$

The effective plasma radius a used in equation (6.5.14) should be considered as the averaged radius of the zone on which the H_α light emissivity reaches its maximum value. For parallel case $a \approx \frac{6.0 + 3.0}{2} = 4.5 \ (cm)$. Then the neutral density of H_2 outside the boundary layer can be calculated as follows using equations (6.5.11):

$$n_{H_2} = \frac{\Gamma_r}{v_{H_2}} = \frac{2.8 \times 10^{18} \ (H_2/cm^2/sec)}{1.93 \times 10^5 \ (cm/sec)}$$

$$= 1.45 \times 10^{13} \ (H_2/cm^3) . \tag{6.6.3}$$

This is the equivalent of $\frac{1}{3}$ $(mTorr)$ at S.T.P., so the hydrogen gas in HBT is nearly fully ionized since the partial pressure of neutrals is much lower than the fill gas pressure.

The corresponding recycling time, according to equation (6.5.14), is:

$$\tau_p = \frac{a \, \bar{n}_e}{4 \, \Gamma_r} = \frac{4.5 \times 2.98 \times 10^{14}}{4 \times 2.8 \times 10^{18}}$$

$$= 1.205 \times 10^{-4} \ (\ sec \ ) = 120.5 \ (\mu sec) . \tag{6.6.4}$$

This is comparable with the observed characteristic time of discharge. We can compare

τ_p with τ_E, the energy confinement time estimated by the following equation[18]:

$$\tau_E \approx \frac{W_p}{I_p V_{loop} - \frac{d}{dt}(W_p + l_i I_p^2)}, \tag{6.6.5}$$

where W_p is the total plasma energy, I_p is the total plasma current, V_{loop} is the plasma loop voltage, and l_i is the internal inductance measured from the internal magnetic probe. A minimum of τ_E can be obtained from equation (6.6.5) by setting $\frac{d}{dt} = 0$. In Fig.6.9(b), at $t = 135$ (μsec), the plasma current $I_p = 6.3$ (kA) and is almost constant, so $\frac{d}{dt} \approx 0$ is satisfied. The total plasma energy can be calculated as:

$$W_p = \frac{3}{2}(k T_e + k T_i)\bar{n}_e V_p = 3 k T_e \bar{n}_e V_p, \tag{6.6.6}$$

where $V_p = \pi a^2 \cdot 2\pi R_0 = 2\pi^2 a^2 R_0$ is the total volume of the plasma. We choose $a = 4.5$ (cm), $k T_e = 4$ (eV), $V_{loop} = 10.0$ (V), and $\bar{n}_e = 2.98 \times 10^{14}$ (cm^{-3}), then $W_p = 5.53$ (J) and $\tau_E = 87.7$ (μsec). Since $\tau_p \approx 1.37\,\tau_E$, the recycling of the hot plasma ions with cold neutrals from the walls could be an important mechanism for the loss of plasma energy. Of course, electron heat conduction and the impurity radiation loss[58] could be responsible for an important reduction of the plasma energy confinement as well.

6.6.2 Reverse Bias Case

Similarly, Fig.6.10(a) and (b) are the measurements and inverted emissions of H_α light at 10 ($mTorr$), respectively. Fig.6.11(a) is the flux of H_2 and Fig.6.11(b) shows two 3–D plots of the emissivity profile at different viewing angle.

In the reverse bias case, the averaged radius of the zone for the peak value of the emissivity is $a \approx \frac{2.5 + 3.5}{2} = 3.0$ (cm). Then the neutral density and the recycling time are calculated as follows:

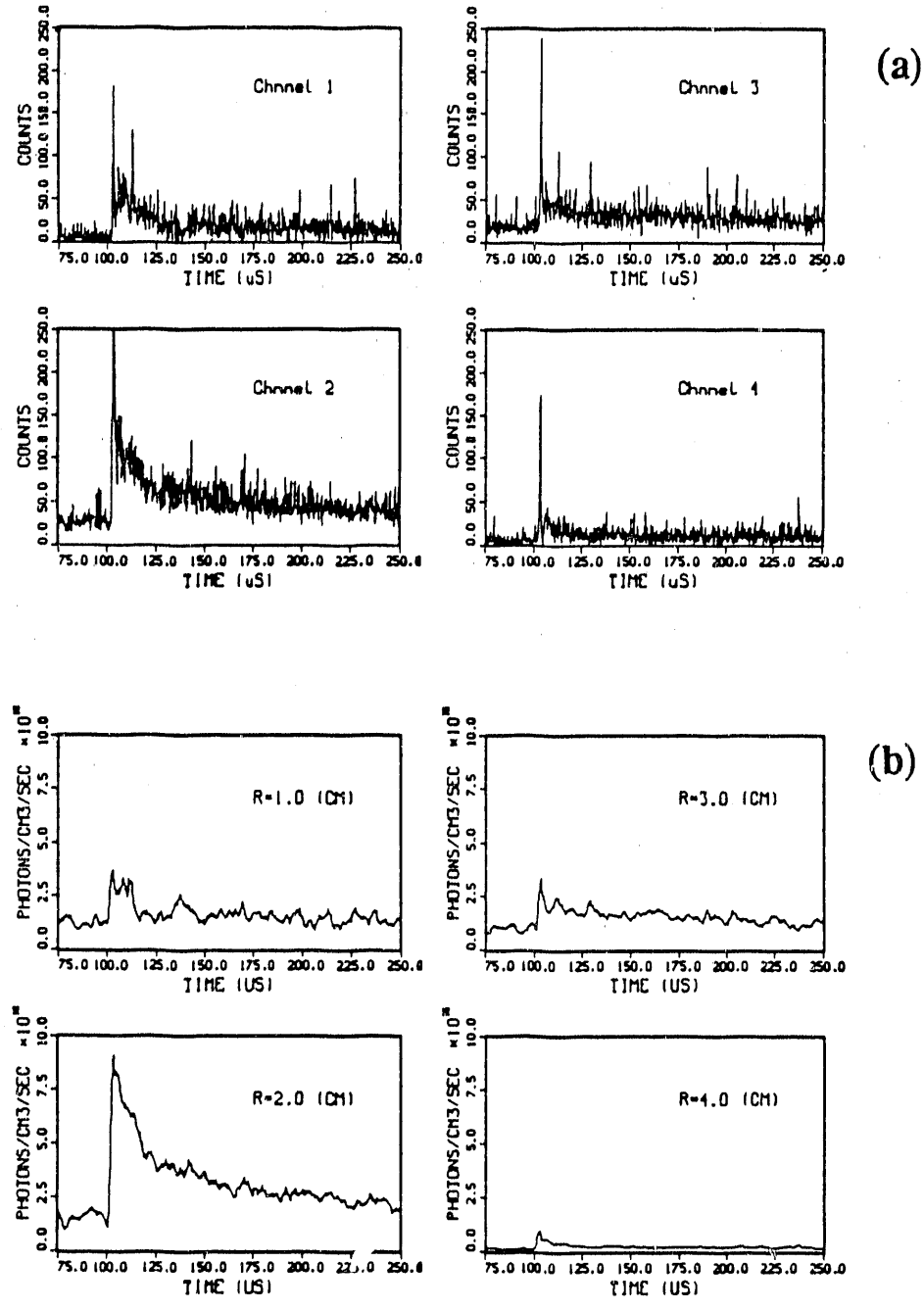

Figure 6.10 (a)The four chordal measurements of H_α light emission; (b)The inverted H_α emissivity in four zones. This is the reverse bias case .

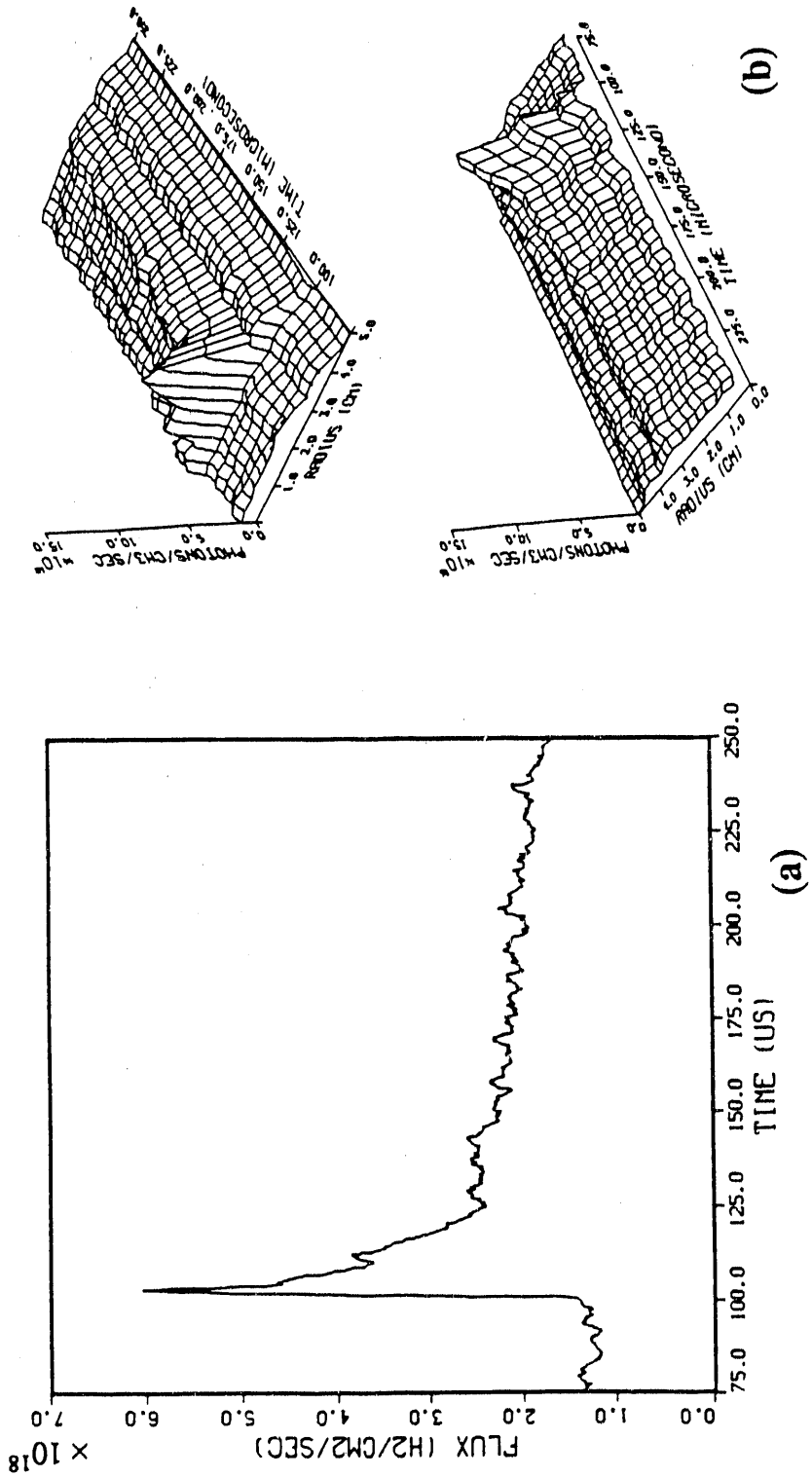

Figure 6.11 (a) The inward minor-radial flux of H_2 molecules; (b) H_α emissivity profile evolution, two different views (reverse bias case) .

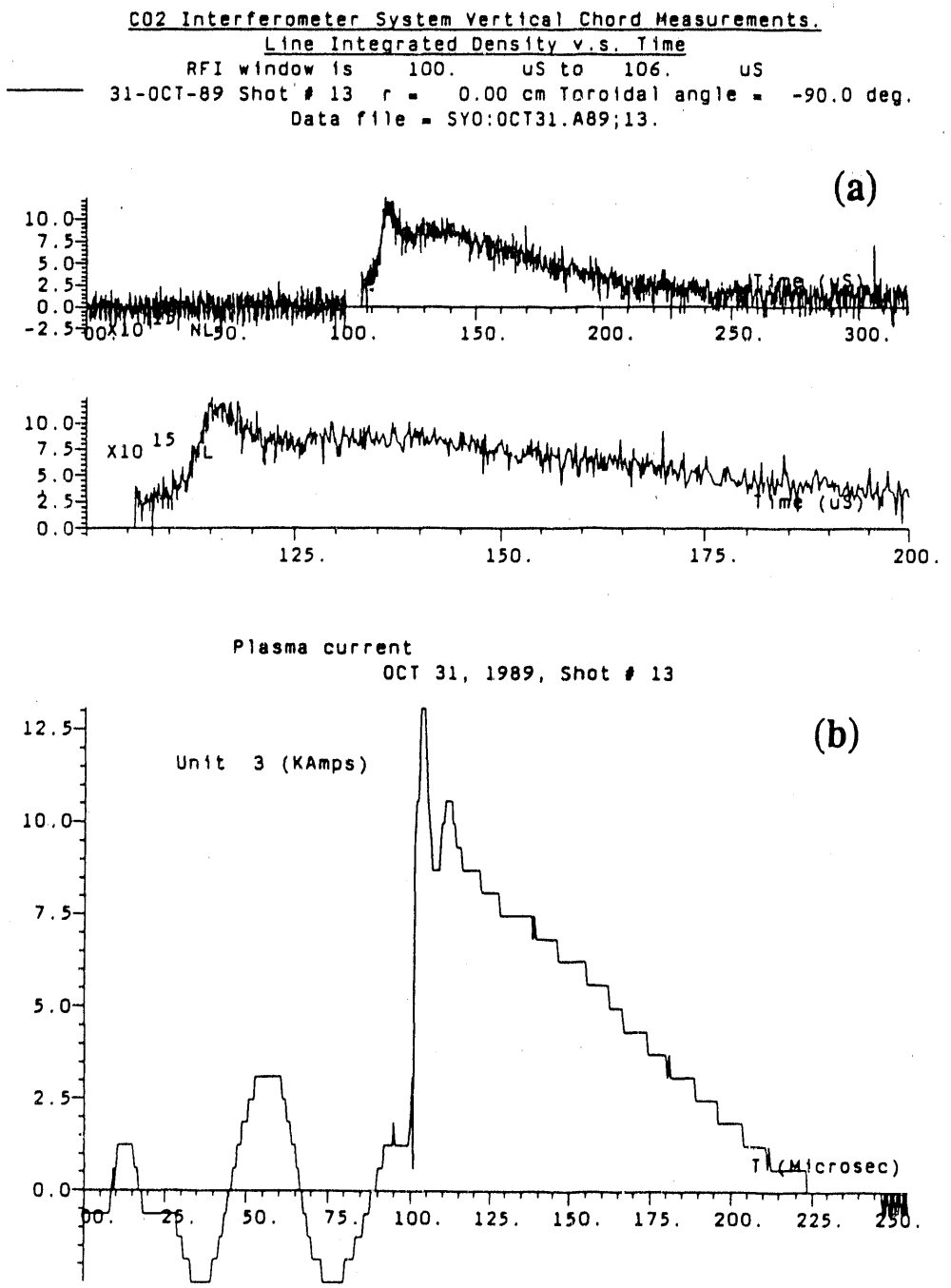

Figure 6.12 (a) The line integrated electron density from CO_2 interferometer; (b) The total plasma current from Rogowski coil. Both for reverse bias case at pressure 10 *mTorr*.

$$n_{H_2} = \frac{\Gamma_r}{v_{H_2}} = \frac{2.0 \times 10^{18}\ (H_2/cm^2/sec)}{1.93 \times 10^5\ (cm/sec)}$$

$$= 1.04 \times 10^{13}\ (H_2/cm^3)\,. \tag{6.6.7}$$

Now as the line integrated electron density is (see Fig.6.12(a)):

$$\int n_e\, dl = 8.0 \times 10^{15}\ (\,cm^{-2}\,)\ (\,at\ 10\ mTorr\,)\,, \tag{6.6.8}$$

then the averaged electron density is

$$\bar{n}_e = \frac{\int n_e\, dl}{L_{vessel}} = 2.8 \times 10^{14}\ (\,cm^{-3}\,)\,, \tag{6.6.9}$$

which is similar to the case of parallel bias case. The averaged ionization degree is also about 100% because the density of neutrals is much lower than the plasma density.

The corresponding recycling time is:

$$\tau_p = \frac{a\,\bar{n}_e}{4\,\Gamma_r} = \frac{3.0 \times 2.8 \times 10^{14}}{4 \times 2.0 \times 10^{18}}$$

$$= 1.05 \times 10^{-4}\ (sec) = 105.0\ (\mu sec)\,. \tag{6.6.10}$$

This is also comparable with the discharge time. If we choose $a = 3.0\ (cm)$, $k\,T_e = 4\ (eV)$, $\bar{n}_e = 2.8 \times 10^{14}\ (cm^{-3})$, and $V_{loop} = 10.0\ (V)$, but $I_p = 7.5\ (kA)$ at $t = 130.0\ (\mu sec)$ (see Fig.6.12(b) for the current profile), then $W_p = 2.3\ (J)$ and $\tau_E = 30.5\ (\mu sec)$. So we have also $\tau_p \approx 3.44\,\tau_E$. Therefore, the recycling of the plasma ions with cold neutrals is less responsible for energy loss in the reverse bias case.

6.6.3 The Pressure Effect

So far, all of the calculations are for the 10 ($mTorr$) pressure of hydrogen gas. We have also measured $\int n_e\, dl$ and the H_α light emissivity at 20 ($mTorr$) and 30 ($mTorr$)

pressures. It is found that $\int n_e \, dl$ depends almost linearly with the fill pressure. However, the H_α light emissivity, as well as the neutral flux Γ_r, only weakly depends on the pressure. This means that the density of the neutrals in the top and bottom regions of the vessel is almost the same at different gas pressure while the averaged electron density $\bar{n}_e$ changes with the fill pressure. As a result, when the pressure increases, the particle (i.e. the proton) recycling time τ_p ($\tau_p = \frac{a \, \bar{n}_e}{4 \, \Gamma_r}$) also increases ($\bar{n}_e$ increases but Γ_r roughly keeps constant).

The energy confinement time τ_E also increases as the fill pressure increases since the plasma current doesn't increase as fast as the total plasma energy does (see equation (6.6.5)).

The detailed calculation for the case of parallel bias shots is listed in table 6, and table 7 is for the case of reverse bias shots. In table 6 there is no good data for the shot at 30 (*mTorr*). All of these shots are obtained at the low toroidal magnetic field (B_t = 2.0 (*kG*)).

The pressure in these tables is obtained from the ionization pressure gauge. Since the pressure gauge was located in an extended tubing attached to the vacuum vessel and the piezoelectric valve is very sensitive to the discharge of capacitor banks, the real value of the fill pressure is usually about 1.9 ~ 2.8 times lower than the reading from the gauge, especially for the higher pressures because of the log scale on the gauge.

From table 6 we can see that $\tau_p \approx (1.2 \sim 1.37) \, \tau_E$ for different fill pressure. This means that the recycling of hot plasma ions with the cold neutrals from the walls is an important mechanism for loss of plasma energy at different fill pressure for the parallel bias case. In table 7, $\tau_p \approx (3.3 \sim 3.5) \, \tau_E$ at different fill pressure, so the recycling of hot ions with cold neutrals is one of the main processes responsible for the reduction of plasma energy confinement in the reverse bias case.

Table 6: The particle recycling time and energy confinement time at different fill pressure (parallel bias case)

P (mTorr)	$\bar{n}_e$ (cm^{-3})	n_{H_2} (cm^{-3})	Γ_r ($H_2/cm^2/s$)	W_p (J)	L_p (kA)	B_t (kG)	τ_p (μs)	τ_E (μs)
10.0	2.98×10^{14}	1.45×10^{13}	2.8×10^{18}	5.53	6.3	1.95	120.5	87.7
20.0	4.75×10^{14}	1.71×10^{13}	3.3×10^{18}	8.75	6.5	2.0	161.9	134.6

Table 7: The particle recycling time and energy confinement time at different fill pressure (reverse bias case)

P (mTorr)	$\bar{n}_e$ (cm^{-3})	n_{H_2} (cm^{-3})	Γ_r ($H_2/cm^2/s$)	W_p (J)	L_p (kA)	B_t (kG)	τ_p (μs)	τ_E (μs)
10.0	2.80×10^{14}	1.04×10^{13}	2.0×10^{18}	2.3	7.5	1.95	105.0	30.5
20.0	4.75×10^{14}	1.30×10^{13}	2.5×10^{18}	3.9	9.5	2.0	142.5	41.0
30.0	1.07×10^{15}	1.55×10^{13}	3.0×10^{18}	8.8	10.7	1.98	267.5	81.9

The ratio of $\left[\frac{\tau_p}{\tau_E}\right]$ in HBT plasmas is comparable with the results obtained in other tokamaks, see reference [59].

CHAPTER SEVEN
CONCLUSION

7.1 The Carbon Ion Diffusion Measurement

The carbon ion impurity diffusion in the Columbia High Beta Tokamak (HBT) is governed by the high collisionality of carbon ions with the plasma ions (protons). Since the quantity of $(\Omega_c \tau_{cp})^2$ is in the order of unity and the mean free path of the carbon ion is much smaller than the plasma radius, the plasma in the vicinity of the carbon probe can be approximated as a cylinder contained by a uniform and straight magnetic field. The transport of the carbon ions released from the discharge of the carbon probe is well interpreted by a *classical* transport theory in a 2-D geometry.

The enhancement of the carbon ion transport due to the *Pfirsch–Schluter* effect is not observed because the mean free path of the carbon ion is much smaller than the plasma radius, as well as the connection length. Therefore, the modification of the classical transport theory, i.e. the *neoclassical* transport theory, is not appropriate for the explanation of carbon ion transport.

A 2-D fluid model is used to describe the diffusion of carbon ions which are released from a pulsed point source located at the magnetic axis of the plasma. We find that the ionic charge (Z_c) affects both the parallel and perpendicular diffusion coefficients. Therefore, it is necessary to distinguish the diffusion coefficients for the carbon ions at different ionization state. It is found that $D_{||}$ is almost the same order as $D_{\perp}$, i.e. the parallel diffusion is stronger than, but comparable with, the perpendicular diffusion because of the low temperature and the high density of the plasma; then the density contours of the carbon ions are a set of nested ellipsoids.

Convective effects can be neglected when the convection velocity $|V_c| \ll \left[\frac{D}{t}\right]^{1/2}$.

The numerical simulation, including the plasma bulk motion, shows that up to 500.0 (m/sec), radial convection flow will not affect the diffusion process to a measurable degree; a similar number is true for the toroidal diffusion as well. However, when the toroidal convection velocity is 1,000.0 (m/sec), there should be an obvious effect on the radial diffusion, quite different from what occurs when there is only a small convection. When the toroidal convective velocity is in the range of 10,000.0 (m/sec), the solution of the fluid equation for the carbon ion density is nearly zero because the convection effect is so strong that almost all of the carbon ions are quickly moved away by the convective flow. Experimentally, we don't observe this phenomena, so the plasma toroidal flow, if exists, must happen only in the early time of the discharge and should quickly decay to a very small value (lower than 100.0 – 1,000.0 (m/sec)). Similarly, the plasma radial flow, if exists, must be lower than the value of 500.0 (m/sec).

7.2 The H_α Light Measurement

The H_α light measurements are made for both cases of parallel and reverse bias shots. We found a zone (the boundary layer) of enhanced H_α emission at $\bar{r}_0 = 4.5$ (cm) for the parallel bias case, and $\bar{r}_0 = 3.0$ (cm) for the reverse bias case. The thickness of the layer is about 0.5 – 1.0 (cm), as expected, and is much smaller than the plasma radius a. We calculated that at 10 ($mTorr$) fill pressure, the particle recycling time is $\tau_p \simeq 120.5$ (μsec) for the parallel bias case and $\tau_p \simeq 105.0$ (μsec) for the reverse bias case. Comparing with the estimate of the corresponding energy confinement time $\tau_E \simeq 87.7$ (μsec) (parallel bias) and $\tau_E \simeq 30.5$ (μsec) (reverse bias), we have $\tau_p \simeq (1.4 \sim 3.5)\,\tau_E$. Hence the recycling of the plasma ions with cold neutrals from the walls can be an important mechanism for the loss of plasma energy. Of course, impurity radiation and electron heat conduction also contribute to the reduction of the energy confinement.

REFERENCES

[1] Navratil, G. A., et al., "Experimental and Theoretical Studies of Circular Cross-Section High-Beta Tokamak", *The Eleventh International Conference on Plasma Physics and Controlled Nuclear Fusion Research 1986*, IAEA-CN-47/A-V-4, Kyoto, Japan, 1986.

[2] Brickhouse, N. S., et al., "Effects of *q* and High Beta on Tokamak Stability", *The Tenth International Conference on Plasma Physics and Controlled Nuclear Fusion Research 1985*, IAEA-CN-44/A-VI-2, London, 1985.

[3] Deniz, A. V., *The Magnetic Field Structure of Experimental High Beta Tokamak Equilibria*, Ph.D Thesis, Report No.105, Columbia University, 1986.

[4] Mauel, M. E., et al., "Measurement of MHD Instabilities in High Beta Tokamaks", *The Tenth International Conference on Plasma Physics and Controlled Nuclear Fusion Research 1988*, IAEA-CN-50/A-VII-6, London, 1985.

[5] Deniz, A. V., Marshall, T. C., Ivers, T., Li, X. and Mauel, M. E., "Transition of a Tokamak Plasma from a State with Low-to High-Poloidal Beta", *Phys. Fluids 29 (12)*, December 1986, p.4119-4122.

[6] Deniz, A. V., Li, X. L. and Marshall, T. C., "Plasma Formation and Equilibrium in a High Beta Tokamak", *Phys. Fluids 30 (8)*, August 1987, p.2527-2537.

[7] Murakami, M., Callen, J. D., Berry, L. A., "Some Observations on Maximum Densities in Tokamak Experiments", *Nuclear Fusion 16 2-Letters*, 1976, p.347-348.

[8] Meyerhofer, D. D., Levinton, F. M., Yamada, M., "Particle Diffusion in a Spheromak", *Physical Review Letters*, Volume 60, Number 10, March 1988, p.933-936.

[9] Mayo, R. M., Levinton, F. M., Meyerhofer, D. D., Chu, T. K., Paul, S. F.,

Yamada, M., "Measurement of the Local Carbon Diffusion Coefficient in the S-1 Spheromak", *Nuclear Fusion*, Vol.29, No.9, 1989, p.1493-1504.

[10] Marmar, E. S., Rice, J. E., Terry, J. L., Seguin, F. H., "Impurity Injection Experiments on the Alcator C Tokamak", *Nuclear Fusion*, Vol.22, No.12, 1982, p.1567-1575.

[11] Gentle, K. W., et al., "Transport Studies in the TEXT Tokamak", *Plasma Physics and Controlled Fusion*, Vol.26, No.12A, 1984, p.1407-1418.

[12] Stratton, B. C., "Impurity Transport in Ohmically Heated TFTR Plasmas", *PPPL-2562, November 1988*.

[13] Levinton, F. M., Meyerhofer, D. D., "Measurement of the Local Particle Diffusion Coefficient in a Magnetized Plasma", *Rev. Sci. Instrum. 58(8)*, August 1987, p.1393-1400.

[14] Roth, J., "Physical Sputtering of Solids at Ion Bombardment", *Physics of Plasma-Wall Interactions in Controlled Fusion, NATO ASI Series*, Plenum Press, New York and London, 1986, p.351-388.

[15] Deniz, A. V., Merlino, R. L., "Bubble-Free Encapsulation of Magnetic Probes for Use in a High-Voltage Plasma Discharge", *Rev. Sci. Instrum. 53(10)*, October 1982, p.1622-1623.

[16] Levinton, F. M., *Measurement of High Beta Tokamak Pressure Profiles with Multipoint Thomson Scattering*, Ph.D Thesis, Report No.92, Columbia University, 1983.

[17] Holland, A. K., *Tomographic Analysis of the Evolution of Plasma Cross-Sections in HBT*, Ph.D Thesis, Report No. 103, Columbia University, May 1986.

[18] Che, H. Y., et al., *Equilibrium, Confinement, and Stability Measurements of the HBT High Beta Tokamak Plasmas*, Report No.110, Columbia University, August 1987.

[19] Spitzer, L., *Physics of Fully Ionized Gases*, Second Edition, Interscience, New York, 1962, p.120-136.

[20] Spitzer, L., "The Stability of Isolated Clusters", *Monthly Notices, Roy.Astron.Soc.(London)*, 100, 396, 1940.

[21] Georgiou, G. E., *Spectroscopic Study of Turbulent Heating in the High Beta Tokamak-Torus II*, Ph.D Thesis, Report No.81, Columbia University, 1979.

[22] McWhirter, R. W. P., "Spectral Intensities", *Plasma Diagnostic Technique*, Academic Press, New York, London, 1965, p.201-264.

[23] Phaneuf, R. A., Janev, R. K., Pindzola, M. S., "Collisions of Carbon and Oxygen Ions with Electrons, H, H_2, and He", *Atomic Data for Fusion*, Vol.V, ORNL-6090/V5, February 1987, p.4-21.

[24] Hulse, R. A., "Numerical Studies of Impurities in Fusion Plasmas", *Nuclear Technology/Fusion*, Vol.3, March 1983, p.259-272.

[25] Sneddon, I. N., *Fourier Transforms*, First Edition, McGraw-Hill Book Company, New York, 1951, p.159-205.

[26] Yan, Z. J., *Equations of Mathematical Physics*, University of Science and Technology of China Press, Hefei, Anhui, January 1980, p.83-84.

[27] Press, W. H., Flannery, B. P., Teukolsky, S. A., Vetterling, W. T., *Numerical recipes: The Art of Scientific Computing*, Cambridge University Press, London, New York, 1987, p.164 and 653-655.

[28] Jackson, J., D., *Classical Electrodynamics*, Second Edition, John Wiley and Sons, New York, 1975, p.472-473 and 820.

[29] Chen, F. F., *Introduction to Plasma Physics and Controlled Fusion, Vol.1: Plasma Physics*, Second edition, Plenum Press, New York and London, 1975, p.183-184.

[30] Kostek, C. A., Marshall, T. C., "Observation of Plasma Rotation in the High Beta Tokamak Torus II", *Plasma Physics*, Vol.25, No.4, 1983, p.421-433.

[31] Meyer, S. L., *Data Analysis for Scientists and Engineers*, John Wiley and Sons, New York, 1975, p.39-48.

[32] The Teaching and Research Section in Mathematics, *Mathematical Analysis*, Vol.2, University of Science and Technology of China Press, Hefei, Anhui, 1978, p.50-54.

[33] Miyamoto, K., *Plasma Physics for Nuclear Fusion*, Revised edition, The MIT Press, 1989, p.198-227.

[34] Rutherford, P. H., "Impurity Transport in the Pfirsh-Schluter Region", *The Physics of Fluids*, Vol.17, No.9, September 1979, p.1782-1784.

[35] Book, D. L., *NRL Plasma Formulary*, Naval Research Laboratory, Revised Edition, Washington, 1987 p.34-35.

[36] Rutherford, P. H., Hirshman, S. P., Jensen, R., Post, D. E., and Seidl, F. G. P., "Impurity Transport in Tokamaks", *Proceedings of the International Symposium on Plasma Wall Interaction"*, Pergamon Press, Oxford, 1977, p.173-191.

[37] Stringer, T. E., "Neoclassical Transport of Impurities", *Theory of Magnetically Confined Plasmas*, International School of Plasma Physics, Villa Monastero, Italy, 1977.

[38] Hawryluk, R. J., Suckewer, S., Hirshman, S. P., "Low-Z Impurity Transport in Tokamaks", *Nuclear Fusion*, Vol.19, No.5., 1979, p.607-631.

[39] Hirshman, S. P., Sigmar, D. J., "Neoclassical Transport of Impurities in Tokamak Plasmas", *Nuclear Fusion*, Vol.21, No.9, 1981, p.1079-1201.

[40] TFR Group, "Light Impurity Transport in the TFR Tokamak: Comparison of Oxygen and Carbon Line Emission with Numerical Simulations", *Nuclear*

Fusion, Vol.22, No.9, 1982, p.1173-1189.

[41] Woods, L. C., *Principles of Magnetoplasma Dynamics*, First Edition, Clarendon Press, Oxford, 1987, p.247-249.

[42] Baylor, L. R., *Particle Transport in Pellet Fueled JET Plasmas*, ORNL/TM-11420, January 1990.

[43] Laing, E. W., "Transport Theory", *Plasma Physics and Nuclear Fusion Research*, U.K.A.E.A. Research Group, Academic Press, London, 1981, p.155-189.

[44] Stringer, T. E., "Anomalous Transport Theory", *Plasma Physics and Nuclear Fusion Research*, U.K.A.E.A. Research Group, Academic Press, London, 1981, p.305-318.

[45] Janev, R. K., Post, D. E., Langer, W. D., Evas, K., Heifetz, D. B., and Weisheit, J. C., "Survey of Atomic Processes in Edge Plasmas", PPPL-2045, November 1983.

[46] McNeill, D. H., and Kim, J., "Balmer Alpha Emission and Hydrogen Atom Energy in Ion Source Discharges", PPPL-1797, July 1981.

[47] McNeill, D. H., Bell, M. G., Grek, B., and LeBlanc, B., "Edge Region Hydrogen Line Emission in the PDX Tokamak", PPPL-2085, February 1981.

[48] Hutchinson, I., H., "Lectures in Plasma Diagnostics", PFC/CP-90-1, DOE/ET-51013-283, Plasma Fusion Center, MIT, June 1990, p.36-39.

[49] Xiang, Z. L., and Yu, C. Y., *The Diagnostic Techniques for High Temperature Plasmas*, Vol. 1, Shanghai Science and Technology Press, 1982, p.13-15.

[50] Mauel, M. E., private communication.

[51] Park, H. K., "A New Asymmetric Abel-Inversion Method for Plasma Interferometry in Tokamaks", PPPL-2592, February, 1989.

[52] Goult, R. J., Hoskins, R. F., Milner, J. A., and Pratt, M. J., *Computational Methods in Linear Algebra*, John Wiley and Sons, New York, 1974, p.72-113.

[53] The Teaching and Researching Section in Mathematics and Computer Software, *Computers and Programming Languages,* Vol.2, Southern Institute of Technology of China, People's Education Press, May 1979, p.166-328.

[54] Horowitz, P., and Hill, W., *The art of electronics,* Cambridge University Press, London, New York, 1980, p.628-630.

[55] Klein, M. V., Furtak., T. E., *Optics,* Second Edition, John Wiley and Sons, 1986, p.76-86.

[56] Leo, W. R., *Technique for Nuclear and Particle Physics Experiment: A How-to Approach,* Springer-Verlag, 1987.

[57] Janev, R. K., Langer, W. D., Evans, Jr., K. E., and Post, D. E., *Elementary Processes in Hydrogen-Helium Plasmas,* Springer-Verlag, 1987, p.35-55.

[58] Izzo, R., *A Numerical Study of the Columbia High Beta Device: Torus-II,* Ph.D Thesis, Report No.84, Columbia University, 1981.

[59] Hugill, J., "Transport in Tokamaks-A Review of Experiment", *Nuclear Fusion,* Vol.23, No.3, 1983, p.331-373.

[60] Ivers, T., private communication.

[61] Ivers, T. H., Mauel, M. E., Navratil, G. A., "Measurement of the Internal Magnetic Structure of Fast-Growing External Kink Instabilities in a High-Beta Tokamak", *Physical Review Letters,* to be published, 1990.

APPENDIX
THE OBSERVATION OF AN INSTABILITY USING THE CARBON PROBE TECHNIQUE

The carbon probe technique can also provide a way for the observation of a macroscopic plasma instability. Fig.A.1 is the measurement of C_{II} light at $\Delta r =$ 2.0 (cm) from the center line of the carbon probe, obtained in the old vacuum chamber. The toroidal magnetic field, for this shot, is $B_t = 2.0\ (kG)$ and the fill pressure is 10 $(mTorr)$. According to the data obtained from the new chamber, the perpendicular diffusion coefficient for C^+ ions should be $D_{2\perp} = 10.0\ (m^2/sec)$. The first envelope of the C_{II} light started at about $t = 80.0\ (\mu sec)$ and this is caused by the plasma ablation. The second envelope, started at $t = 153.0\ (\mu sec)$, resulted from the discharge of the carbon probe fired at $t = 151.0\ (\mu sec)$. This envelope includes the three pulses of the source discharge, which finished before $t = 195.0\ (\mu sec)$ (see also Fig2.4.(a) for the probe discharge current), and eventually decay to zero (the predicted curve is plotted as a dotted line in Fig.A.1).

However, at $t = 200.0\ (\mu sec)$, there is a third signal with peak value even higher than that of the first two. This can be explained as a rapid outward plasma radial displacement that carries out the radiating carbon ions. According to the discussion in Chapter Four, the speed of this convection should be larger than

$$V_c = \left[\frac{D_{2\perp}}{t} \right]^{1/2} = \left[\frac{10.0\ (m^2/sec)}{(200.0 - 150.0) \times 10^{-6}\ (sec)} \right]^{1/2} \tag{A.1}$$

$$= 500.0\ (m/sec)\ ;$$

otherwise, the displacement would not be detected. Therefore, the criterion for the measurement of a radial macroscopic instability is that the speed of the bulk motion, V_b, should satisfy the following condition:

$$V_b \geq \left[\frac{D_\perp}{t} \right]^{1/2}, \tag{A.2}$$

where $D_\perp$ is the radial diffusion coefficient of the carbon ions and t is the time interval between the start time of the carbon probe discharge and the time at which the instability occurs. Typically, the speed of a MHD instability is in the order of the Alfven speed V_A ($V_A \sim 10^5$ (m/sec)); so we have no trouble with this technique to measure the macroscopic MHD instability because the diffusion is much slower than the displacement.

Unfortunately, other diagnostic data, such as the magnetic probe, the loop voltage, the plasma current, etc., were not retrieved for this shot due to a computer problem, so there is no corroborating evidence for this instability from the magnetic probe and the loop voltage. However, after inspecting the data file of the instability study in HBT[60-61], we find that macroscopic instabilities do occur at $t \approx 200.0$ (μsec) under the same operating conditions as obtained for Fig.A.1. An example of these unstable shots is presented in Fig.A.2, which has the similar electron density, temperature and toroidal magnetic field as the one shown in Fig.A.1. From the magnetic probe data, the outer-loop voltage, the H_α light emission, etc., a radial displacement happened at almost the same time as that when the third peak of signal appeared in Fig.A.1.

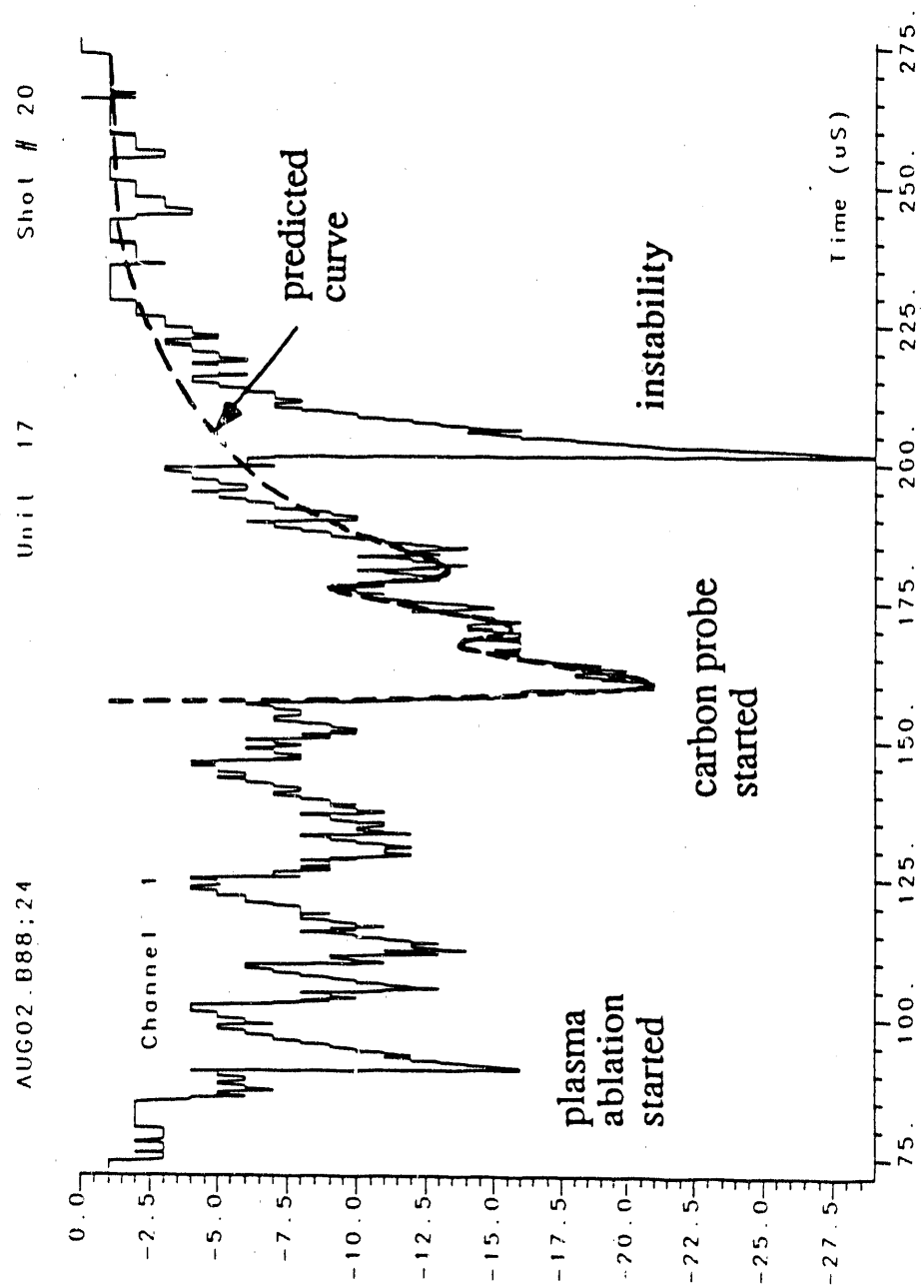

Figure A.1 An instability measurement from C_{II} light emission.

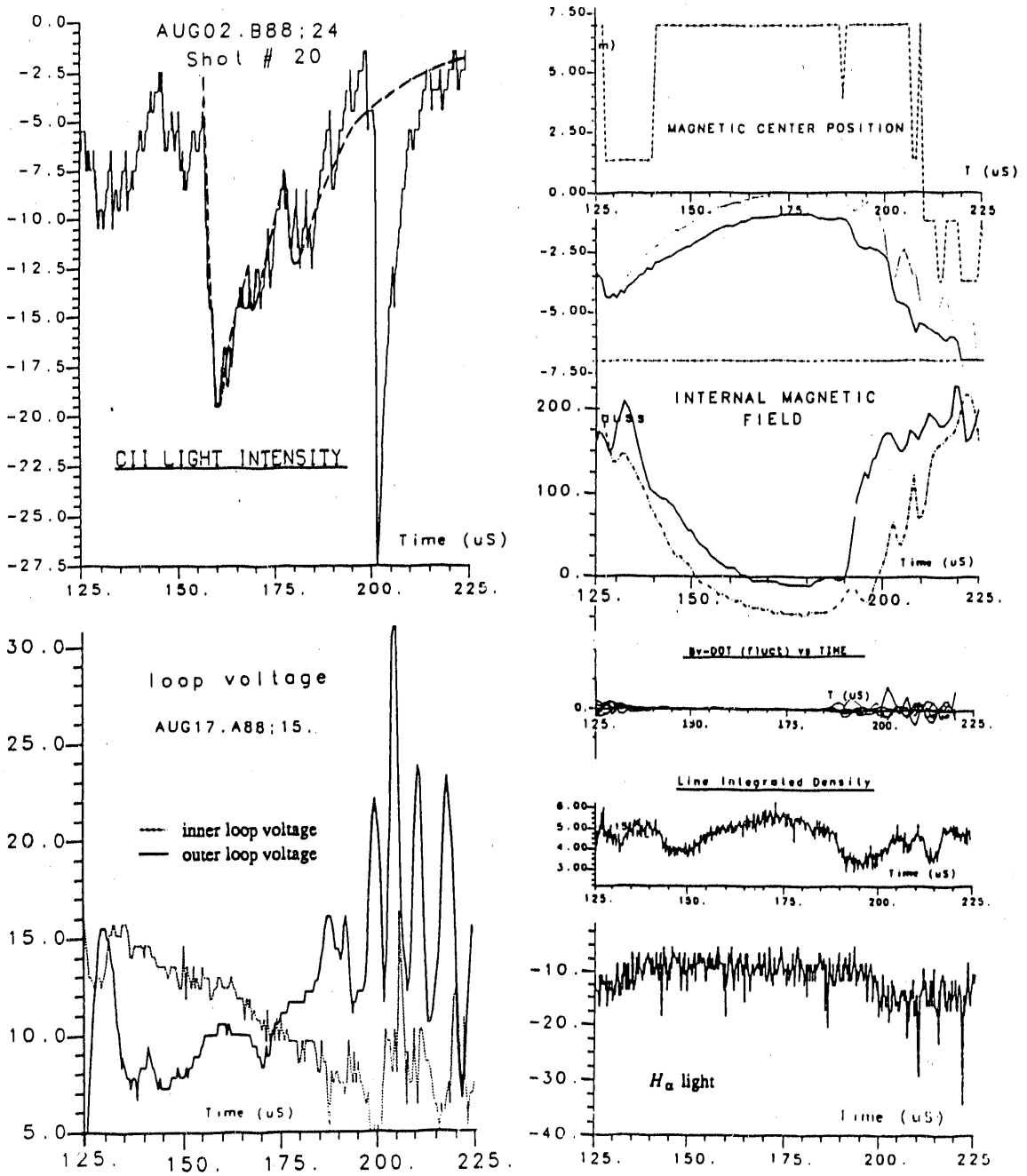

Figure A2 An example of an unstable shot .

END

DATE FILMED

12 / 19 / 90